Final Report

High-Pressure Turbulent Flame Speeds and Chemical Kinetics of Syngas Blends with and without Impurities

For the Period:
October 1, 2013 – September 30, 2017

Principal Authors:
Eric Petersen, Olivier Mathieu, Anibal Morones, Charles Keesee,
Joshua Hargis, and Victor Leon

Principal Investigator:
Eric L. Petersen
Department of Mechanical Engineering
Texas A&M University
3123 TAMU
College Station, TX 77843
979-845-1257

Issue Date: January 29, 2018

DOE Award No. DE-FE0011778
TEES Project 502951-00001

Texas A&M Engineering Experiment Station
400 Harvey Mitchell Parkway, Suite 300
College Station, TX 77845-4375

ABSTRACT

This Final Report documents the entire four years of the project, from October 1, 2013 through September 30, 2017. This project was concerned with the chemical kinetics of fuel blends with high-hydrogen content in the presence of impurities. Emphasis was also on the design and construction of a new, high-pressure turbulent flame speed facility and the use of ignition delay times and flame speeds to elucidate the diluent and impurity effects on the fuel chemistry at gas turbine engine conditions and to also validate the chemical kinetics models. The project was divided into five primary tasks: 1) Project Management and Program Planning; 2) Turbulent Flame Speed Measurements at Atmospheric Pressure; 3) Experiments and Kinetics of Syngas Blends with Impurities; 4) Design and Construction of a High-Pressure Turbulent Flame Speed Facility; and 5) High-Pressure Turbulent Flame Speed Measurements. Details on the execution and results of each of these tasks are provided in the main report.

TABLE OF CONTENTS

EXECUTIVE SUMMARY

Besides mostly H_2 and CO, syngas also contains reasonable amounts of light hydrocarbons, CO_2, H_2O, N_2, and Ar. Impurities such as NH_3, HCN, COS, H_2S, and NOx (NO, NO_2, N_2O) are also commonly found in syngas. The presence of these impurities, even in very low concentrations, can induce some strong changes in combustion properties. Although they introduce potential design and operational issues for gas turbines, these changes in combustion properties due to the presence of impurities are still not well characterized. The aim of this work was therefore to investigate numerically the effect of the presence of impurities in realistic syngas compositions on some fundamental combustion properties of premixed systems such as laminar flame speed and ignition delay time, at realistic engine operating conditions. To perform this study, a state-of-the-art C0-C3 detailed kinetics mechanism was used. This mechanism was combined with recent, optimized sub-mechanisms for impurities which can impact the combustion properties of the syngas such as nitrogenous species (i.e., N_2O, NO_2, NH_3, and HCN) and sulfur-based species such as H_2S, SO_2 and COS. Several temperatures, pressures, and equivalence ratios were investigated. The results of this study showed that the addition of some impurities modifies notably the reactivity of the mixture. The ignition delay time is decreased by the addition of NO_2 and H_2S at the temperatures and pressures for which the HO_2 radical dominates the H_2 combustion. However, while NO_2 has no effect when OH is dominating, H_2S increases the ignition delay time in such conditions for pressures above 1 atm. The amplitude of these effects is however dependent on the impurity concentration. Laminar flame speeds are not sensitive to NO_2 addition but NH_3 and HCN are, inducing a small reduction of the laminar flame speed at fuel rich conditions. H_2S exhibits some inhibiting effects on the laminar flame speed but only for high concentrations. The inhibiting effects of NH_3, HCN, and H_2S are due to the OH radical consumption by these impurities, leading to radicals that are less reactive.

New Laminar Flame Speed measurements have been taken for a wide range of syngas mixtures containing hydrocarbon impurities. These experiments encompassed a wide range of syngas mixtures beginning with two baseline mixtures. The first of these baseline mixtures was a bio-syngas with a 50/50 H_2/CO split, and the second baseline mixture was a coal syngas with a 40/60 H_2/CO split. Experiments were conducted over a range of equivalence ratios from ϕ = 0.5 to 3 at initial conditions of 1 atm and 300 K. Upon completion of the baseline experiments, two different hydrocarbons were added to the fuel mixtures at levels ranging from 0.8 to 15% by volume, keeping the H_2/CO ratio locked for the bio-syngas and coal syngas mixtures. The addition of these light hydrocarbons, namely CH_4 and C_2H_6, had been shown in recent calculations by the authors' groups to have significant impacts on the laminar flame speed, and the present experiments validated the suspected trends. For example, a 7% addition of methane to the coal-syngas blend decreased the peak flame speed by about 25% and shifted it from ϕ = 2.2 to a leaner value near ϕ = 1.5. Also, the addition of ethane at 1.7% reduced the mixture flame speed more than a similar addition of methane (1.6%). In general, the authors' chemical kinetic model over predicted the laminar flame speed by about 10-20% for the mixtures containing the hydrocarbons. The decrease in laminar flame speed with the addition of the hydrocarbons can be explained by the increased importance of the inhibiting reaction $CH_3 + H (+M) \leftrightarrow CH_4 (+M)$, which also explains the enhanced effect of C_2H_6 compared CH_4, where the former produces more CH_3 radicals, particularly at fuel rich conditions.

A complete characterization of the turbulence in the first-generation turbulent flame speed bomb was performed. The study objectives were to: confirm the earlier PIV measurements with LDV, this time in the actual vessel; expand the interrogation area from a plane to a 3-D volume; assess the performance of the impellers at different levels of rotational speed, and; provide a more direct assessment of the temporal scale. Basic concepts on the statistical description of turbulence were introduced. Two levels of fan speed were chosen to run in the modified turbulent vessel, namely 8,000 and 12,000 rpm. A tri-dimensional space situated at the center of the vessel was systematically scanned and turbulence statistics were obtained. The results confirmed some of the observations of the PIV, but the extension of the measurements to a tridimensional region also revealed unfavorable characteristics previously missed. The work concludes by suggesting improvements for a new design of turbulent flame bomb. In particular, a new arrangement of the fans is advised.

Laminar flame speed experiments were performed to study the effect that small amounts of H_2S has on the flame speed of syngas mixtures. The syngas was composed of 60/40 CO/H_2 in an oxidizer containing argon rather than nitrogen. The O_2/Ar ratio was chosen to keep the same adiabatic temperatures as those with air at similar equivalence ratios. The results showed that the argon produced lower flame speeds than with the nitrogen-based air, and that the H_2S had more of an effect at the rich conditions, decreasing the laminar flame speed. A kinetics model compared will with the data in general, but improvements can still be made.

Shock-tube experiments were performed to study the oxidation of H_2S in H_2S-O_2-Ar mixtures (98% Ar) over a range of temperatures and equivalence ratios (0.5, 1, 1.5) for pressures around 1 atm. Measurements included ignition delay times inferred from OH* emission and the direct measurement of water time histories using a tunable diode laser absorption technique. These data are currently being used to make significant changes to the current chemical kinetics mechanism, and this part of the study is still ongoing. The few available mechanisms in the literature cannot model the new data, and it is providing difficult to match all the data available in the literature.

A new fan-stirred flame bomb apparatus was designed, manufactured, and installed during this project. This is the second iteration of such a device by this group. The present version extends the test domain of pressure and temperature to at least 10 atm and 150°C, respectively. To further the experimental pressure, a vented deflagration mode of operation has been considered. This bomb has two breaches that can be used as vents when fitted with the proper diaphragm or burst disk. This vessel has now 4 windows and has been prepared to make use of optical diagnostics that demand two orthogonal lines of sight. The range of turbulence fluctuation is also increased to 10 m/s, and spatial distribution of the fans is improved with respect to the original design. Further details on the turbulence generation and its control is provided. After the turbulence field was characterized for the optimum impeller geometry, a series of high-pressure, turbulent flames were measured for 50:50 H_2:CO mixtures in air. Pressures of 1, 5, and 10 bar were measured. The results show a marked effect of both fan speed (varied from 2000 to 8000 rpm) and pressure on the propagation of the turbulent flame.

EXPERIMENTS AND KINETICS OF SYNGAS BLENDS WITH IMPURITIES

This portion of the project focused on the measurement of laminar flame speed and ignition delay time for syngas mixtures with various impurities; chemical kinetics modeling is ultimately what the data are used to improve and to which they are compared. Two main projects were completed, the first dealing with the use of our improved NOx and impurities kinetics mechanisms to perform calculations at gas turbine conditions to assess the effect of the impurities. The second was concerned with the measurement of laminar flame speeds for syngas blends with hydrocarbon addition.

Effect of Impurities at Gas Turbine Conditions

Synthetic gas or syngas can be produced from nearly any type of carbonaceous feedstock. This wide array of possible sources in particular makes syngas an attractive fuel for dependable, clean, and efficient energy production using Integrated Gasification Combined Cycle (IGCC) plants or gas turbines. The syngas composition depends on the type of feedstock and on the process used to gasify it. The composition can include 6.8%–50.4% H_2, 8.1%–60.5% CO, 1.3%–29.6% CO_2, 0%–20.4% H_2O, 0%–9.3% CH_4 [Kreji et al., 2013], and many impurities. Despite this complex composition, most of the studies on syngas have been historically focusing on H_2/CO only. Few studies have also dealt with steam [Das et al., 2011], CO_2 [Burke et al., 2007; Natarajan et al., 2005; Wang et al., 2013], N_2 [Prathap et al., 2008], or realistic mixture composition (although highly diluted in Ar for the shock-tube data) [Herzler et al., 2012; Mathieu et al., 2013a].

Recently, the effects of hydrocarbon addition (CH_4, C_2H_6, C_2H_4, and C_2H_2) were studied numerically at realistic gas turbine conditions for a series of syngas compositions (from the baseline CO/H_2 to real syngas mixture compositions) derived from biomass and coal feedstocks by the present authors [Mathieu et al., 2013b]. The results of this study exhibited the great importance of hydrocarbons, even in small concentration, on fundamental combustion properties such as ignition delay time (τ_{ign}) and laminar flame speed (S_L). Indeed, while the CO/H_2 ratio was found to be of little importance on the ignition delay time, the addition of hydrocarbons increased τ_{ign} notably under the conditions investigated. This increase was a function of the nature and concentration of the hydrocarbon and the pressure and temperature range. At 1 atm, the ignition delay time was increased over the entire range of temperatures studied, whereas τ_{ign} was increased only on the high-temperature side at 10 and 35 atm. This effect of the ignition delay time was mostly due to methane and ethylene. For the flame speed, however, ethane was found to be of larger importance, with a noticeable decrease in S_L. It was demonstrated in this previous study that the effects of the hydrocarbon addition are mostly due to reactions between the hydrocarbons and/or their radicals with the radical H, hence competing with the most important promoting reaction $H + O_2 \rightleftarrows OH + O$ at the conditions of interest to gas turbine combustors.

The comparison between the baseline coal- and bio-derived syngases with averaged syngases (containing hydrocarbons, CO_2, H_2O, N_2) showed a large difference in the ignition delay time and in the flame speed. The impacts on the flame speed were due to both chemical and thermal (i.e. flame temperature) effects, whereas the effects on the ignition delay time were linked to the chemistry only. The main outcome of that recent study was that the baseline CO/H_2 mixtures generally studied are not in many cases good candidates to study syngas combustion under gas turbine conditions because they represent an over-simplified blend.

As mentioned earlier, in addition to these fuels and diluents, traces of impurities can also be found in syngas. These impurities are typically NH_3, HCN, COS, H_2S, SO_2, and NOx (NO, NO_2, N_2O), although some traces of HCl and metals have also been reported [Newby et al., 2001; Trembly et al., 2007]. While the concentration of these impurities is typically very low (up to 1.3% and 0.3% vol. for H_2S and HCN, respectively [Cayana et al., 2008], 1.64% vol. for NH_3 [Cuoci et al., 2007], 0.055 % vol. for SO_2 and 0.123 % vol. for NOx [Xu et al., 2011]), they can have a great impact on fuel combustion properties [Glarborg, 2007]. It is also worth mentioning that the combustion properties of syngas are, in most cases, driven by hydrogen combustion chemistry [Krejci et al., 2013; Kéromnès et al., 2013; Mathieu et al., 2013b]. Recent studies with H_2 mixtures seeded with small amounts of NO_2 [Mathieu et al., 2013c] and H_2S [Mathieu et al., 2013d] exhibited a great influence of these impurities on the ignition delay time (generally promoting for NO_2 and generally inhibiting for H_2S). However, except for NH_3 [Mathieu et al., 2013a], there is no study on the influence of these impurities on realistic syngas combustion. There is also no study on the potential interactions between these impurities during syngas combustion.

Since kinetics models for these impurities have been recently optimized (Mathieu et al. for NO_2 (2013c), N_2O (2012), H_2S (2013d), NH_3/H_2-NOx, Dagaut et al. (2008) for HCN, and Glarborg and Marshall (2013) for COS), it is now possible to investigate numerically, with a reasonable degree of accuracy, the effects of these impurities on syngas combustion properties. The aim of the present study was therefore to perform such a numerical investigation for fundamental combustion properties of premixed systems, i,e, laminar flame speed and ignition delay time. Realistic engine operating conditions were selected, and various syngas compositions were studied.

The syngas compositions defined in Mathieu et al. (2013b) were used to define neat baselines for bio- and coal-derived syngases herein. These baseline mixtures were then computationally seeded with various impurities specific to each type of syngas to exhibit their effects on combustion properties of interest herein. The mixtures investigated and the modeling procedure details are covered first in this section of the report. Results are then presented and discussed, with emphasis on the significant chemical kinetics reactions.

Modeling Procedure. The detailed chemical kinetics model used herein is based on the C0–C3 mechanism developed at the National University of Ireland, Galway (NUIG) [Metcalfe et al., 2013]. A high-temperature version of this model, where low-temperature species (peroxy radicals, alkyl hydroperoxides, ketohydroperoxides, etc.) and reactions were removed, was used for flame speed calculations. To this base mechanism were added the sub-mechanisms for H_2/H_2S [Mathieu et al., 2013d] and NH_3-H_2/NOx. The HCN mechanism was added to the NH_3 part and has been unchanged from the work of Dagaut et al. (2008). The COS sub-mechanism is from a recent paper from Glarborg and Marshall (2013), while the NOx-HC interactions were taken from the work of Sivaramakrishnan et al. (2007). The complete mechanism comprises 1,331 reactions and 198 species, while the high-temperature mechanism consists of 188 species and 1,243 reactions. The modeling of the various syngas mixture was done with air as the oxidant. The Chemkin package 10112 was used to perform the numerical calculations. Ignition delay time calculations were performed using the Closed Homogeneous Batch Reactor model with the Constant Volume assumption, while the Premixed Laminar Flame Speed Calculation model was used to compute the laminar flame speeds.

Mixtures Investigated. The two first mixtures studied were the baseline (CO/H_2) coal- and bio-derived syngas mixtures in air (60/40 and 50/50 (mole ratio), respectively). These neat mixtures were then seeded with single impurities (COS, NH_3, and H_2S for the coal syngas and NO_2, NH_3, HCN, and SO_2 for the bio-syngas) at their maximum reported concentration in the literature to estimate the effect of impurities on ignition delay time and laminar flame speed on these baseline mixtures. Note that due to their possible large concentration and presumably great effects on combustion properties, NO_2 and H_2S have also been studied at averaged concentrations that have been determined from several syngas mixture compositions [Munasinghe and Khanal, 2010; Xu et al., 2009; Sharma et al., 2013; Newby et al., 2001]. For each type of syngas, a mixture containing all the aforementioned impurities at their maximum reported concentration was also investigated, to exhibit possible synergistic or antagonistic effects between impurities.

In addition to these baseline syngases, averaged, realistic, neat mixtures, containing H_2/CO, H_2O, N_2, CO_2, and small hydrocarbons were also defined. More details on these realistic mixtures and on the effects of hydrocarbons on ignition delay time and laminar flame speed are available in Mathieu et al. (2013b). Effects of NO_2 and H_2S at averaged and maximum reported concentrations for, respectively, these realistic bio- and coal-derived syngases were investigated. Finally, the realistic syngases were also studied with the maximum reported concentration of all impurities specific to each type of syngas. The compositions of the mixtures investigated in this study are provided in Table 1 for the bio-derived syngas and in Table 2 for the coal-derived syngas.

Table 1 Bio-syngas mixtures investigated (mole fraction).

Mixture	H_2	CO	CH_4	C_2H_6	C_2H_4	C_2H_2	H_2O	N_2	CO_2	NO_2	NH_3	HCN	SO_2
bBiosyn	50.0	50.0	—	—	—	—	—	—	—	—	—	—	—
bBiosyn-HC	39.1	39.1	15.0	0.8	5.3	0.7	—	—	—	—	—	—	—
bBiosyn-NO_2Av	49.98	49.98	—	—	—	—	—	—	—	0.04	—	—	—
bBiosyn-NO_2Hi	49.94	49.94	—	—	—	—	—	—	—	0.12	—	—	—
bBiosyn-NH_3	49.86	49.86	—	—	—	—	—	—	—	—	0.28	—	—
bBiosyn-HCN	49.86	49.86	—	—	—	—	—	—	—	—	—	0.28	—
bBiosyn-SO_2	49.9725	49.9725	—	—	—	—	—	—	—	—	—	—	0.055
bBiosyn-impur	49.6325	49.6325	—	—	—	—	—	—	—	0.12	0.28	0.28	0.055
Biosyn	21.75	21.75	8.5	—	—	—	20.0	13.0	15.0	—	—	—	—
Biosyn-NO_2Av	21.7413	21.7413	8.4966	—	—	—	19.992	12.995	14.994	0.04	—	—	—
Biosyn-NO_2Hi	21.7239	21.7239	8.4898	—	—	—	19.976	12.984	14.982	0.12	—	—	—
Biosyn-impur	21.5901	21.5901	8.4375	—	—	—	19.853	12.905	14.8898	0.12	0.28	0.28	0.055

Flame speed computations were performed at 1 and 15 atm; between ϕ = 0.5 and 3.0; and for unburned gas temperatures (T_u) of 300 and 500 K. Ignition delay time computations were performed between 900 and 1400 K; at 1, 10, and 35 atm; and for an equivalence ratio of ϕ = 0.5.

Stoichiometric mixtures were also investigated for the neat mixtures as well as for the mixtures with all the impurities. The ignition delay time was defined by the step rise in the OH* signal, which occurs at ignition, as visible in Fig. 1. As can be seen in this figure, a similar result would have been obtained using the pressure signal, even though a slow and very moderate pressure increase can be observed before the ignition.

Table 2 Coal-syngas mixtures investigated (mole fraction).

Mixture	H_2	CO	CH_4	C_2H_6	C_2H_4	C_2H_2	H_2O	N_2	CO_2	COS	H_2S	NH_3
bCoalsyn	40.00	60.00	—	—	—	—	—	—	—	—	—	—
bCoalsyn-HC	36.268	54.402	7.4	1.7	0.1	0.13	—	—	—	—	—	—
bCoalsyn-COS	39.996	59.994	—	—	—	—	—	—	—	0.01	—	—
bCoalsyn-H_2SAv	39.996	59.994	—	—	—	—	—	—	—	—	0.01	—
bCoalsyn-H_2SHi	39.6	59.4	—	—	—	—	—	—	—	—	1	—
bCoalsyn-NH_3	39.84	59.76	—	—	—	—	—	—	—	—	—	0.4
bCoalsyn-impur	39.436	59.154	—	—	—	—	—	—	—	0.01	1	0.4
Coalsyn	23.48	35.22	1.6	—	—	—	21.8	8.5	9.4	—	—	—
Coalsyn-H_2SAv	23.4777	35.2165	1.5998	—	—	—	21.7978	8.4991	9.3991	—	0.01	—
Coalsyn-H_2SHi	23.2452	34.8678	1.584	—	—	—	21.582	8.415	9.306	—	1	—
Coalsyn-impur	23.1489	34.7234	1.5774	—	—	—	21.4926	8.3802	9.2675	0.01	1	0.4

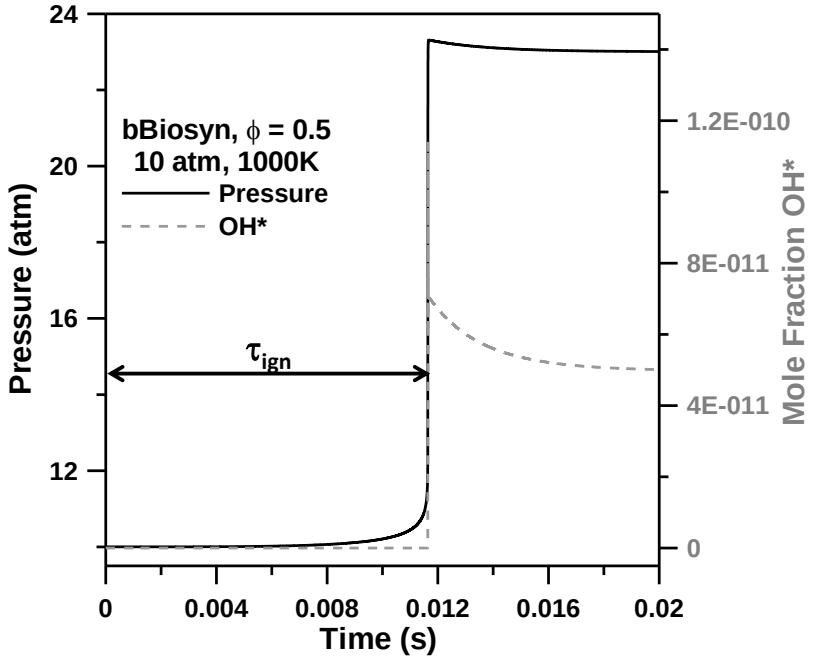

Fig. 1 Determination method for the ignition delay time using the computed pressure and OH* mole fraction profiles.

Model Validation. While the base C0-C3 mechanism has been validated against a large body of hydrogen and syngas data from the literature, it is however worth mentioning that there are very few experimental results available for syngas mixtures with impurities. To the best of the authors' knowledge, the only results available are the results from Mathieu et al. (2013a) where ignition delay times for baseline (H_2 and CO only) and realistic (H_2, CO, CO_2, CH_4, and H_2O) bio-syngas mixtures diluted in Ar, with and without NH_3, were measured at various pressures. These results were computed with the detailed kinetics mechanism described above, and the results are visible in Fig. 2 for the baseline mixture and in Fig. 3 for the realistic mixture. As can be seen in Fig. 2, the model captures very well the experimental trends for all pressure conditions. Data at 30 atm were perfectly reproduced, and the lack of effect of NH_3 is captured. At 10 atm, ignition delay times are also perfectly reproduced by the model, except for the highest temperature when NH_3 is in the mixture, where a small discrepancy can be observed. While the model predicts a very small increase in the ignition delay time at this pressure when ammonia is added, it is difficult to observe such a small increase from the experimental results. At the lowest pressure investigated, the results are generally well reproduced except for the lowest temperatures where the model is under-reactive. The very small decrease in the ignition delay time observed when NH_3 is added, over most of the temperature range, can be observed both in the experiments and in the modeling at this pressure condition.

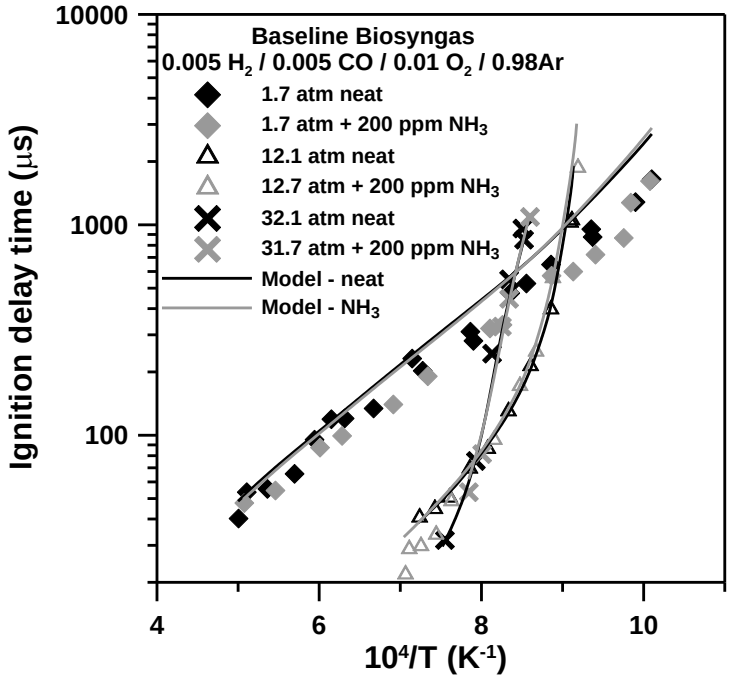

Fig. 2 Comparison between ignition delay times for a baseline (H_2/CO) biosyngas mixture diluted in Ar, with and without NH_3, from Mathieu et al. (2013a) and the model used in this study at various pressure conditions.

For the realistic biosyngas mixture, Fig. 3, the experimental trends associated with the pressure condition and the presence of NH_3 (very small increase in the ignition delay time for the latter case) are also captured by the model. However, for this type of mixture, the model tends to be under-reactive by a factor of around 2, especially on the low-temperatures side at 1.7 atm and on the high-temperatures side for higher pressures. This validation stage shows the ability of the model to reproduce experimental trends with good accuracy in the results. This comparison demonstrates the relevance of the mechanism used in this study to conduct a numerical investigation for the temperature and pressure range relevant to gas turbines.

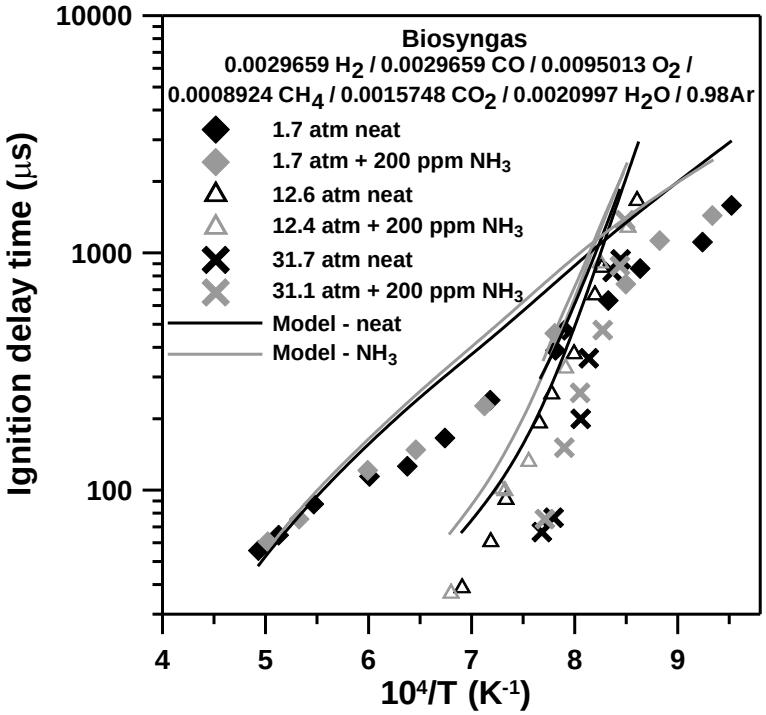

Fig. 3 Comparison between ignition delay times for a biosyngas mixture diluted in Ar, with and without NH_3, from Mathieu et al. (2013a) and the model used in this study at various pressure conditions.

Results. The results are presented as follows: first, the calculations for the neat baseline mixtures (CO and H_2 only) are covered to study the effect of the H_2/CO ratio. This series is followed by the effect of the impurity additions on these baseline mixtures. Finally, the averaged syngas mixtures including all species are considered with and without impurities. For each general category, the ignition delay time results are discussed first, followed by the laminar flame speed results.

Neat Baseline Mixtures. The effects of the ratio between CO and H_2 on the ignition delay time, for the three pressure conditions investigated, are typically small, as can be seen in Mathieu et al. (2013b). Therefore, the small change in the CO/H_2 ratio between the coal- and bio-syngases investigated herein does not really alter the predicted ignition delay times for these neat baseline mixtures; regardless of the temperature or pressure. One can mention that the main difference between these two syngases is that the ignition delay times are slightly shorter for the mixture that

contains the higher proportion of H_2 (bio-syngas), but no change in the behavior was reported. One can also mention the important, and temperature-dependent, effect of pressure on the ignition delay time (see Mathieu et al. (2013b)). These effects were discussed in detail already [Kéromnès et al., 2013] and are essentially due to the competition between two reactions: the chain-branching reaction $H + O_2 \rightleftarrows OH + O$ (r1) and the chain-propagating reaction $H + O_2 (+M) \rightleftarrows HO_2 (+M)$ (r2). While r1 controls the reactivity at higher temperature, r2 is predominant at lower temperature. In addition, the transition from r2 to r1 is shifted to higher temperatures when the pressure is increased. This pressure dependence is due to the increased collisional efficiency of r2 which decreases the overall reactivity. This reason explains why low-pressure experiments show a stronger reactivity than high-pressure experiments at the intermediate-temperature range.

Although the laminar flame speed for syngas mixtures was investigated for two temperatures and for two pressures, only two examples with the extreme conditions are discussed here. The trends and conclusions drawn from these two examples are indeed the same for the two other conditions, not shown. The difference between these two types of mixtures was discussed in detail previously [Mathieu et al., 2013b]. At 1 atm for an inlet temperature of 300 K with the baseline coal- and bio-syngases, the difference between the two types of syngas can be relatively important for this combustion property; the blend with the lowest amount of H_2 has the lowest flame speed, especially at fuel rich conditions. The difference between the two mixtures is close to 30 cm/s. Similar observations can be made for the 15-atm, 500-K condition, the difference being a little larger (45 cm/s). Note that the largest difference between the two syngases was observed for the 1 atm, 500-K case, which also corresponds to the condition where the flame speeds are the highest.

Impurity Addition to the Baseline Mixtures. The effects of impurity addition on the baseline bio-syngas mixture are visible in Figs. 4 (1 atm), 8 (10 atm), and 9 (35 atm). As can be seen in Fig. 4, only NO_2 seems to have an effect (promoting) on the ignition delay time, for temperatures lower than 1000 K. The differences in the ignition delay time induced by the presence of NH_3, HCN, or SO_2 are indeed too small to be discernible. At 900 K, the ignition delay time is reduced by about 85% by the addition of 400 ppm of NO_2, and this reduction in the ignition delay time reaches 92% for the highest NO_2 concentration investigated (bBiosyn-NO_2Hi mixture). The ignition delay times for the mixture containing all the impurities at their highest level are nearly the same as for the bBiosyn-NO_2Hi mixture, which indicates that there is no important interaction between the impurities at this condition.

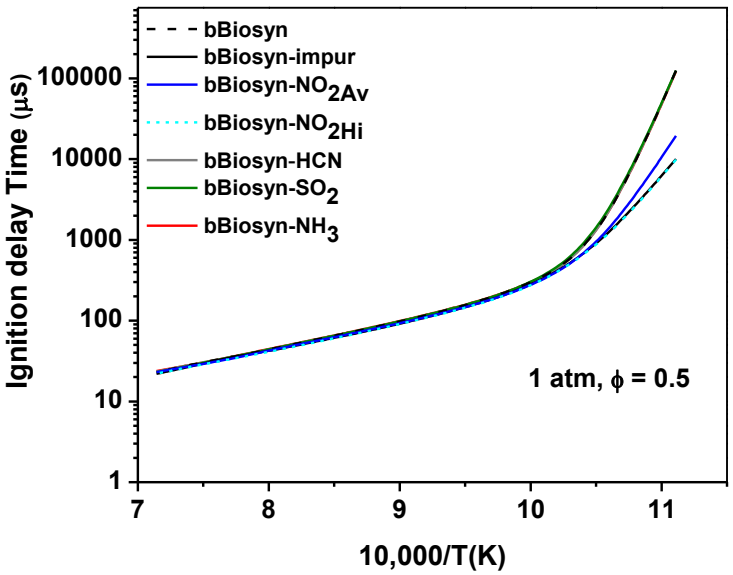

Fig. 4 Effect of various impurities on the ignition delay time for a baseline bio-syngas mixture at 1 atm.

At 10 atm (Fig. 5), similar to the atmospheric-pressure case, only NO_2 has an effect on the ignition delay time. This effect starts at higher temperatures, below 1150 K, and is less important than for the previous case: 23% and 45% reduction at 900 K for the bBiosyn-NO_2Av and bBiosyn-NO_2Hi mixtures, respectively.

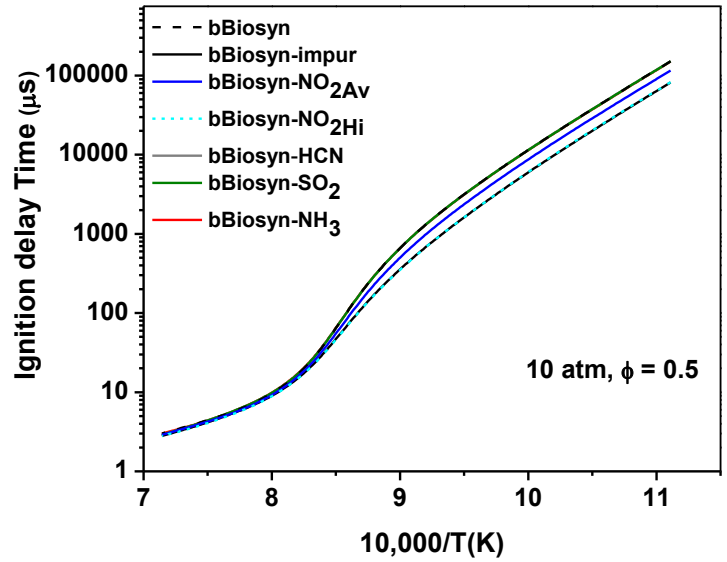

Fig. 5 Effect of various impurities on the ignition delay time for a baseline bio-syngas mixture at 10 atm.

A similar trend is followed at higher pressure, Fig. 6, where NO_2 has some effect at temperatures below 1250 K but with reductions in the ignition delay time that are less important: ignition delay times are shorter by around 19% with an addition of 400 ppm of NO_2 and by around 36% with 1200 ppm of NO_2 at 900K.

The effects on the ignition delay time of impurities that are more specific to coal syngas are visible in Figs. 7, 8, and 9 for pressures of 1, 10, and 35 atm, respectively. As can be seen in these figures, similar to the baseline bio-syngas, an addition of NH_3 does not modify the ignition delay time over the range of conditions investigated. A similar absence of any effect is observed with COS. However, if an averaged concentration of H_2S does not have a distinguishable effect on τ_{ign}, a relatively large concentration of this contaminant exhibits a large effect on the ignition delay time. At 1 atm (Fig. 7), it is visible that H_2S reduces the reactivity of the mixture over the entire range of temperature and strongly reduces the curvature of the neat mixture profile for temperatures below 1000 K. It is also worth mentioning that the mixture with all the impurities yields the same results as the bCoalsyn-H_2SHi mixture, indicating that there is no interaction between impurities at these conditions.

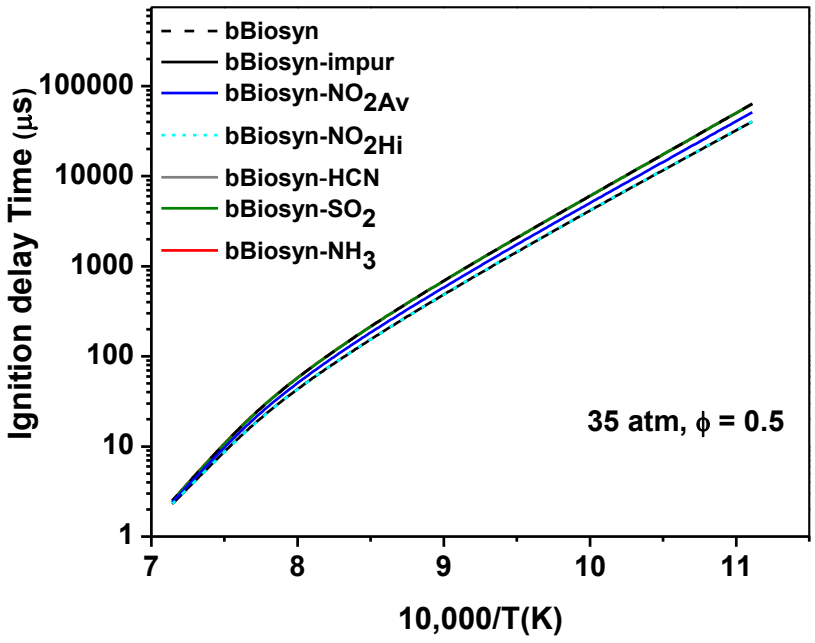

Fig. 6 Effect of various impurities on the ignition delay time for a baseline bio-syngas mixture at 35 atm.

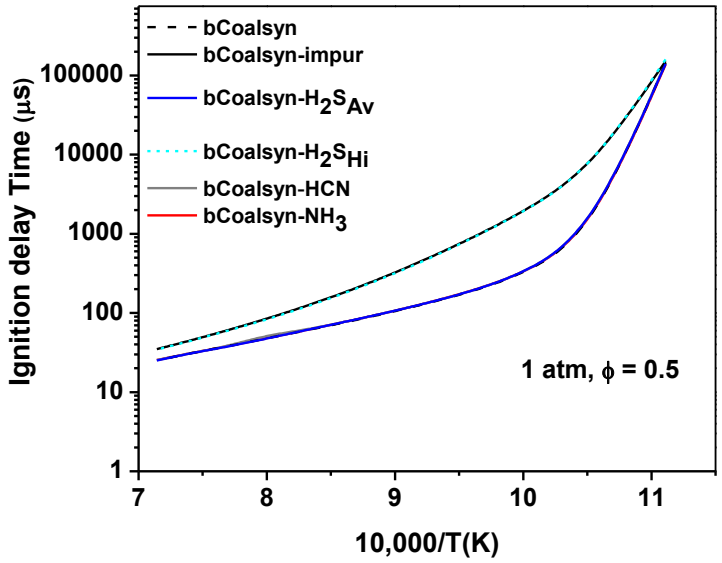

Fig. 7 Effect of various impurities on the ignition delay time for a baseline coal-syngas mixture at 1 atm.

At 10 atm, Fig. 8, the high concentration of H_2S is also the only case where an effect on the ignition delay time can be observed. Again, it seems that the curvature in τ_{ign} observed with the neat mixture is strongly reduced by the presence of this contaminate. In this case, however, the reduction of the curvature corresponds to an increase in the ignition delay time for temperatures above 1150 K (by up to 46%) and to a decrease in τ_{ign}, as high as 60%, below this temperature.

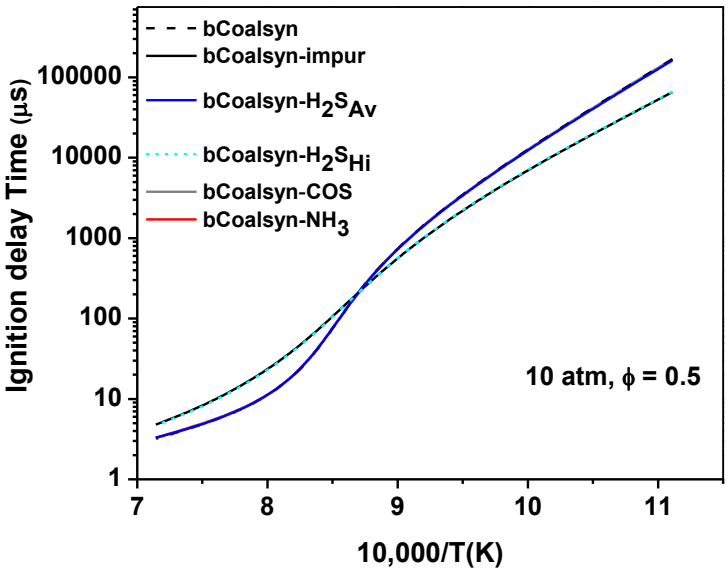

Fig. 8 Effect of various impurities on the ignition delay time for a baseline coal-syngas mixture at 10 atm.

At 35 atm, Fig. 9, the effects are similar to those observed at 10 atm but the temperature at which the curves cross is shifted to 1330 K. While the increase in τ_{ign} is rather moderate at the highest temperature investigated (from 3.2 to 4.8 µs), the increase in the reactivity due to the large H_2S concentration is rather important on the low-temperature side (from 168,500 to 65,000 µs).

The effect of the equivalence ratio was also investigated in this study. Since this effect has been studied already by the authors [Mathieu et al., 2013b] with neat mixtures. To summarize these results, increasing the equivalence ratio from 0.5 to 1.0 has nearly no effect on the ignition delay time at 1 atm for the bBiosyn mixture. A small decrease in the reactivity is observed at the two temperature extremities at 10 atm (4.5% difference at the highest temperature and up to 13.7% for the lowest temperature), while the decrease in the reactivity covered most of the temperature range at 35 atm. Similar results were observed for the bCoalsyn mixture.

In the presence of impurities, Fig. 10, the ignition delay times of a baseline bio-syngas mixture doped with impurities seem to be modified in larger proportion by a change in the equivalence ratio than for the neat mixture. The ignition delay time is indeed decreased by between 20% (1400 K) and 45% (900 K) at 1 atm and up to 55% at 10 atm, 900 K. For the highest pressure investigated, the reduction in τ_{ign} is between 25% at 1400 K and 50% at 900 K.

Concerning the baseline coal-syngas mixture with impurities, Fig. 11, the effect of the equivalence ratio on τ_{ign} seems a bit more complex. Indeed, the ignition delay time is slightly increased at 1 atm for temperatures above 950 K and is decreased below this temperature. It is also worth mentioning that a similar behavior is observed at 10 atm, with the pivot temperature being around 1135 K. At 35 atm, τ_{ign} are shorter for the highest equivalence ratio over the entire range of temperature investigated, the decrease being very small at high temperature and above 35 % at 900 K.

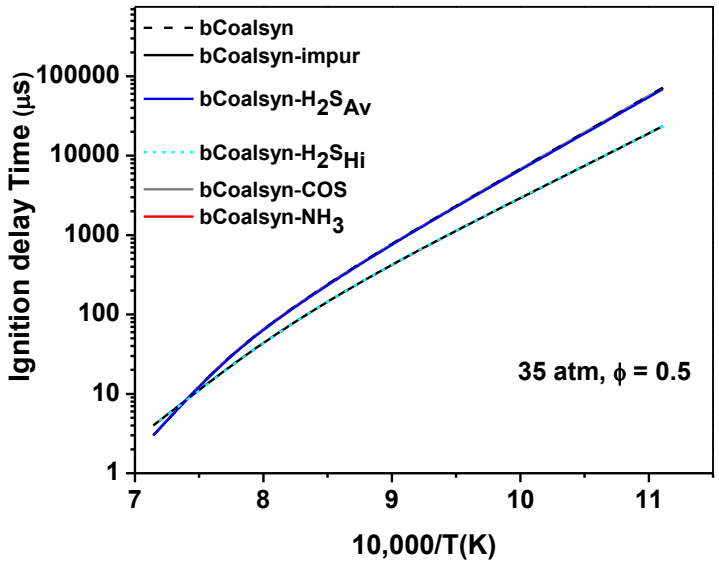

Fig. 9 Effect of various impurities on the ignition delay time for a baseline coal-syngas mixture at 35 atm.

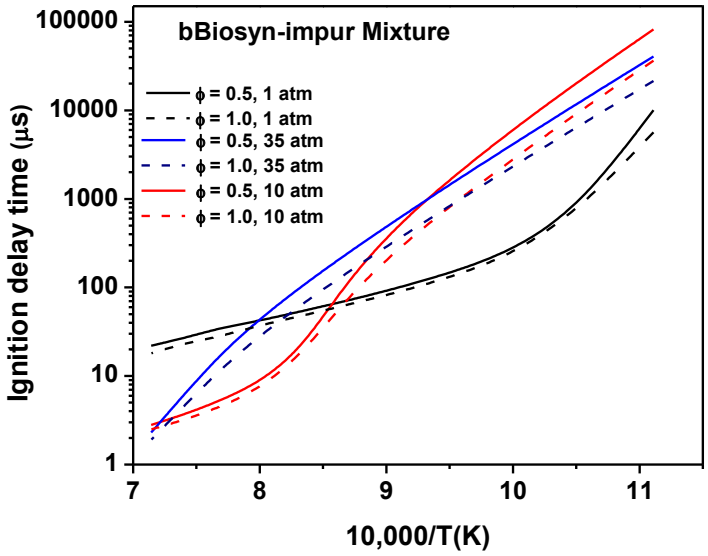

Fig. 10 Equivalence ratio effect on the ignition delay time for a baseline bio-syngas mixture with impurities at 1, 10, and 35 atm.

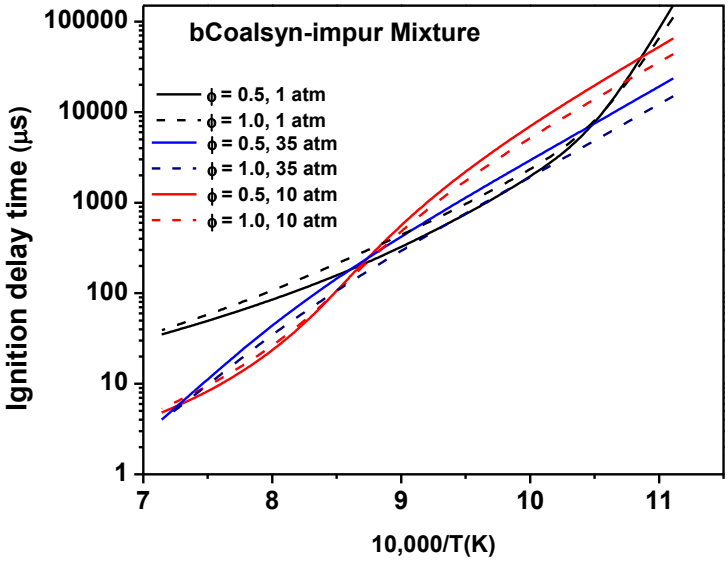

Fig. 11 Equivalence ratio effect on the ignition delay time for a baseline coal-syngas mixture with impurities at 1, 10, and 35 atm.

It is interesting to compare the effects of hydrocarbon addition, investigated in Mathieu et al. (2013b), with the effects of impurity addition on the baseline syngas mixtures investigated herein. As can be seen in Fig. 12 for the bBiosyn mixture, the effects from hydrocarbon addition are overall higher than the effects for impurity addition. This is particularly true at 1 atm where a large effect of hydrocarbon addition is visible on the entire range of conditions against the low-temperature side only for the impurities. At 10 atm, it is interesting to see that the effects of

hydrocarbons are visible only on the high-temperature side, whereas the impurity effect is still observed for low temperatures at this pressure condition. The same behavior is observed for the 35-atm case, although the effects of both hydrocarbons and impurities are smaller at this pressure condition. Similar observations can be made for the coal-syngas mixture, Fig. 13, although the hydrocarbon-addition effects are less important in this case.

The effects on the laminar flame speed of various impurities with bBiosyn at 1 atm, 300 K and 15 atm, 500 K as initial conditions are visible in Fig. 14 and Fig. 15, respectively. As can be seen in Fig. 14, the addition of impurities has a small effect on the laminar flame speed and this effect is visible for fuel rich conditions only, for an equivalence ratio larger than 1.5. Results are also somewhat contrary to what has been observed for the ignition delay time: the reactivity of the mixture is decreased by the impurity addition and this effect is found for all the impurities except NO_2 and SO_2. The largest effect is provided by NH_3 (reduction of the maximum S_L by 5cm/s), and the maximum laminar flame speed is only reduced by a few cm/s, from 191 to 189 cm/s, for the 0.28% NH_3 addition. When all the impurities are added together, the laminar flame speed is further reduced. However, the reduction corresponds to the sum of the effects from NH_3 and HCN, indicating that there is no enhancing or inhibiting interaction between these impurities.

At the other extreme condition, 500 K and 15 atm (Fig. 15), laminar flame speeds are higher but trends in the results are similar. However, the decrease in the laminar flame speed with impurities is slightly larger, from 271 to 258 cm/s, with NH_3.

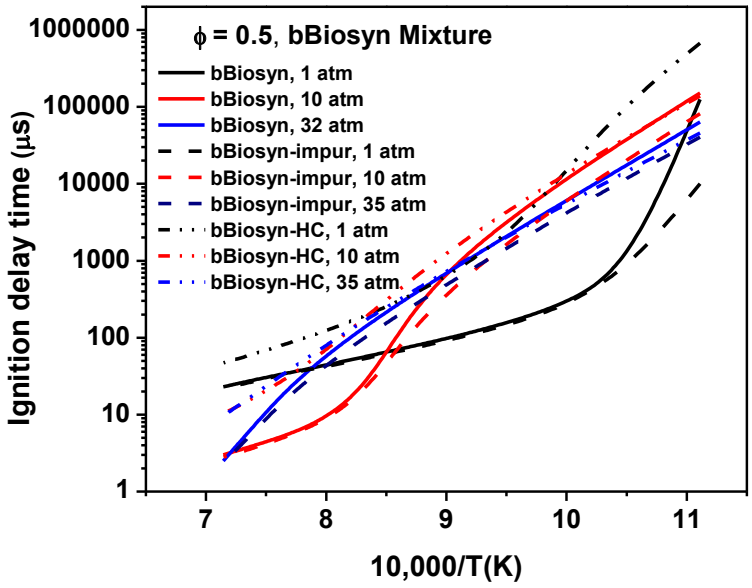

Fig. 12 Impurity- and hydrocarbon-addition effects on the ignition delay time of a baseline bio-syngas mixture at ϕ = 0.5 and at 1, 10, and 35 atm.

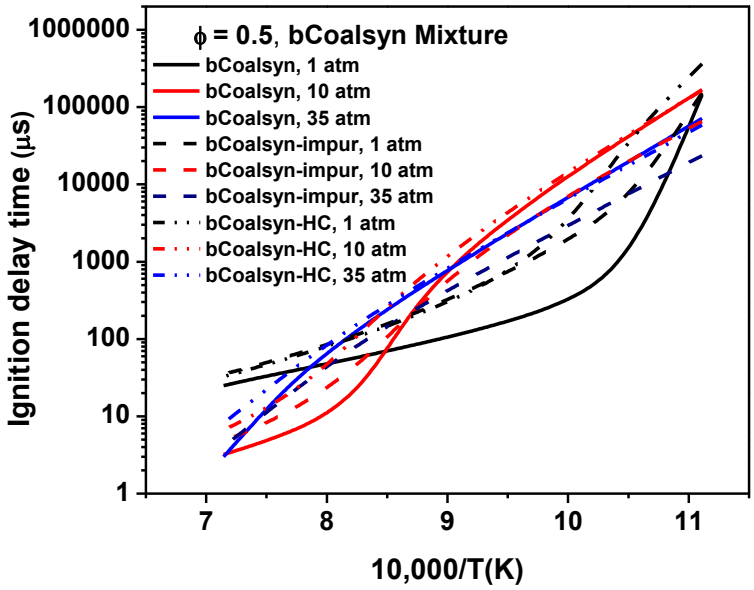

Fig. 13 Impurity- and hydrocarbon-addition effects on the ignition delay time of a baseline coal-syngas mixture at ϕ = 0.5 and at 1, 10, and 35 atm.

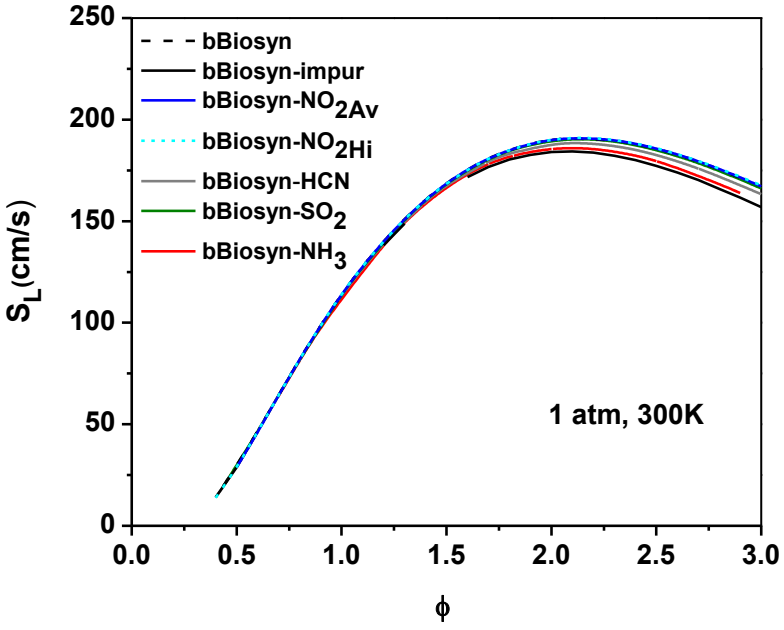

Fig. 14 Laminar flame speed as a function of equivalence ratio for a baseline bio syngas with various impurities and at 1 atm and 300 K as initial conditions.

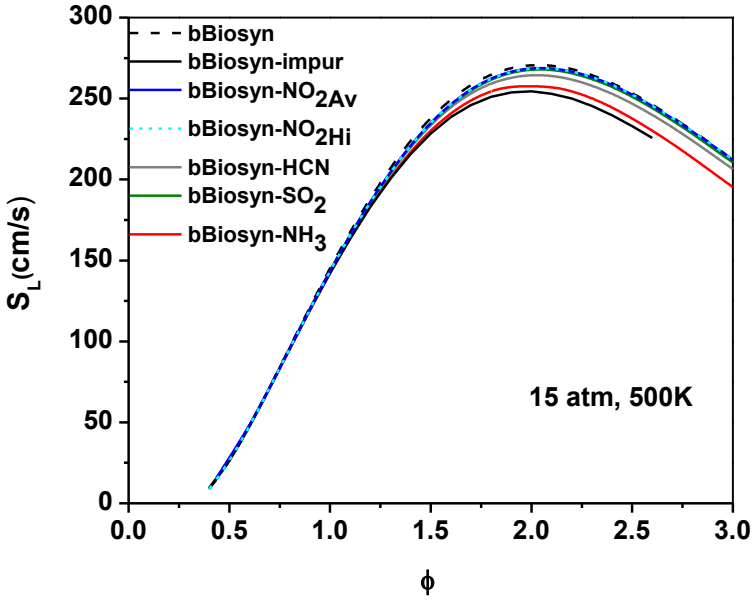

Fig. 15 Laminar flame speed as a function of equivalence ratio for a baseline bio syngas with various impurities and at 15 atm and 500 K as initial conditions.

For the bCoalsyn mixture, Fig. 16, a decrease in the laminar flame speed is still observed with the NH_3 addition. A low concentration of H_2S seems to be without effect, while a relatively large reduction of the laminar flame speed (from 169 to 153 cm/s for the maximum flame speed) can be observed with the highest H_2S concentration. As for the bBiosyn mixtures, these effects are observed for equivalence ratios above 1.5 only and the effects of impurities on the laminar flame speed (NH_3 and H_2S in this case) seem to add to each other without apparent interaction.

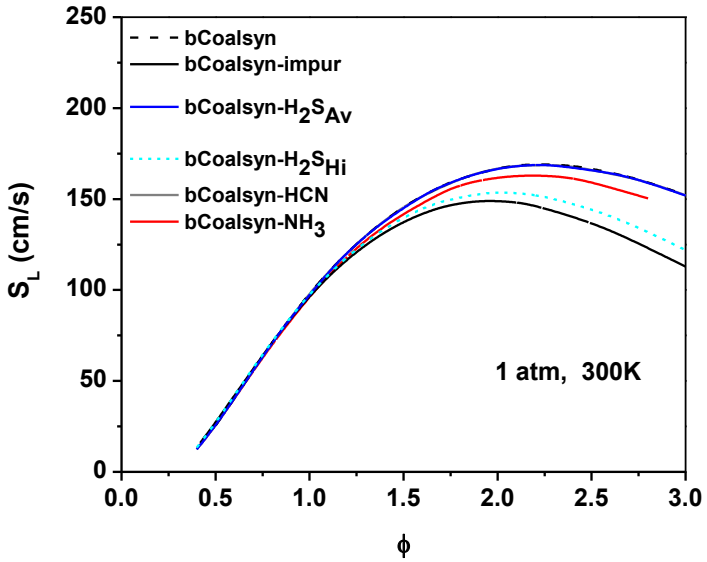

Fig. 16 Laminar flame speed as a function of equivalence ratio for a baseline coal syngas with various impurities at 1 atm and 300 K as initial conditions.

Figure 17 shows the results at the other extreme conditions, 500 K and 15 atm. As can be seen, the trends are the same as for the 300-K, 1-atm case. However, one can notice the higher flame speed at this condition and the fact that the maximum flame speed is shifted towards lower equivalence ratios. The effect of impurities is also slightly higher at this extreme condition and this result seems to be mostly due to the pressure increase (by comparing results obtained at 15 atm, 300 K and 1 atm, 500 K, not shown).

The influence of impurity addition on the baseline biosyngas can be compared to the effects of hydrocarbon addition at 1 atm and 300 K in Fig. 18. It is visible in this figure that the effect of impurities is significantly smaller than the effect of hydrocarbons. Indeed, while the impurities decreased the laminar flame speed by only about 3%, S_L is reduced by 55% when hydrocarbons are present, and the equivalence ratio for which this maximum in the flame speed is observed is also notably decreased, from 2.1 to 1.3.

At higher pressure and temperature, Fig. 19, the difference between impurities and hydrocarbon addition is even higher: a 66% decrease in S_L was observed for the hydrocarbon addition (with a maximum in S_L observed at ϕ = 2.0 for the baseline and 1.2 or the hydrocarbon addition) and around 6% for the impurities.

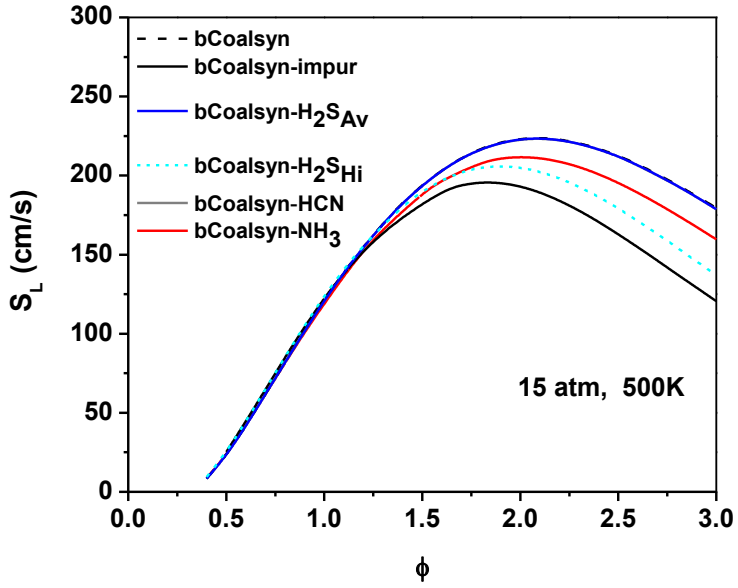

Fig. 17 Laminar flame speed as a function of equivalence ratio for a baseline coal syngas with various impurities and at 15 atm and 500 K as initial conditions.

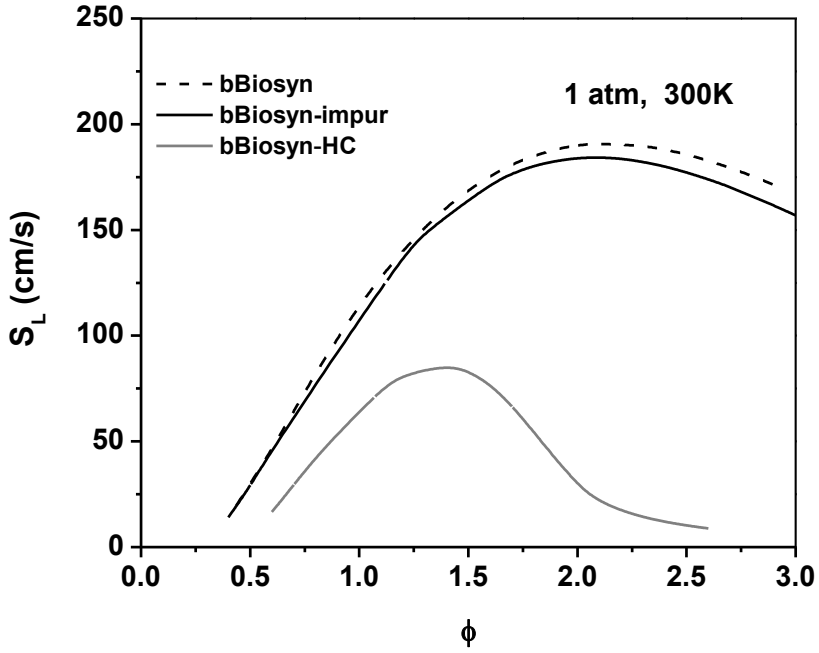

Fig. 18 Laminar flame speed as a function of equivalence ratio for a baseline bio syngas with various impurities or hydrocarbons at 1 atm and 300 K as initial conditions.

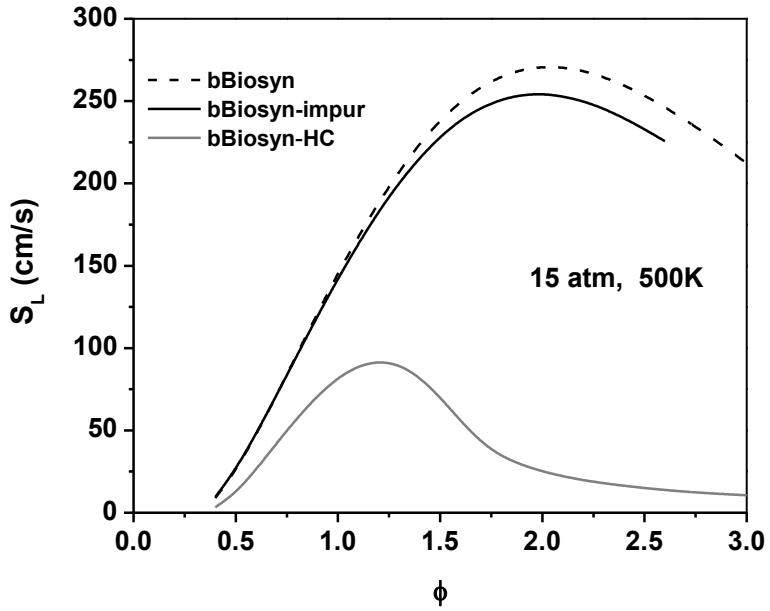

Fig. 19 Laminar flame speed as a function of equivalence ratio for a baseline bio-syngas with various impurities or hydrocarbons at 15 atm and 500 K as initial conditions.

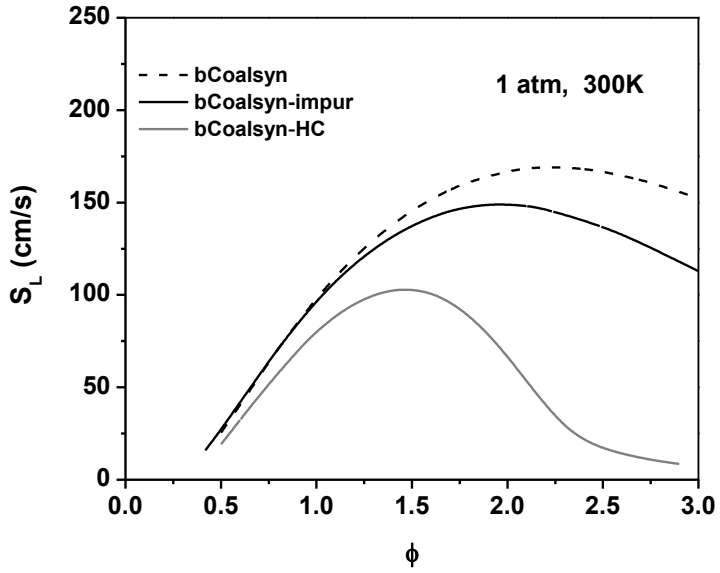

Fig. 20 Laminar flame speed as a function of equivalence ratio for a baseline coal syngas with various impurities or hydrocarbons at 1 atm and 300 K as initial conditions.

The same comparison between the effects of impurities and hydrocarbons was made for the baseline coal syngas at 1 atm, 300 K (Fig. 20) and 500 K, 15 atm (Fig. 21). One can notice from these figures that the effects of impurities are more important for the coal syngas than for the bio-syngas while the effects of the hydrocarbons are lower. As a result, while a significant difference can be observed between these two kinds of addition, the difference is not as large as for the bio-syngas (S_L reduction of 12% by impurities and 39% by hydrocarbons at 300 K and 1 atm and of 13% and 51%, respectively, for the 500-K, 15-atm condition).

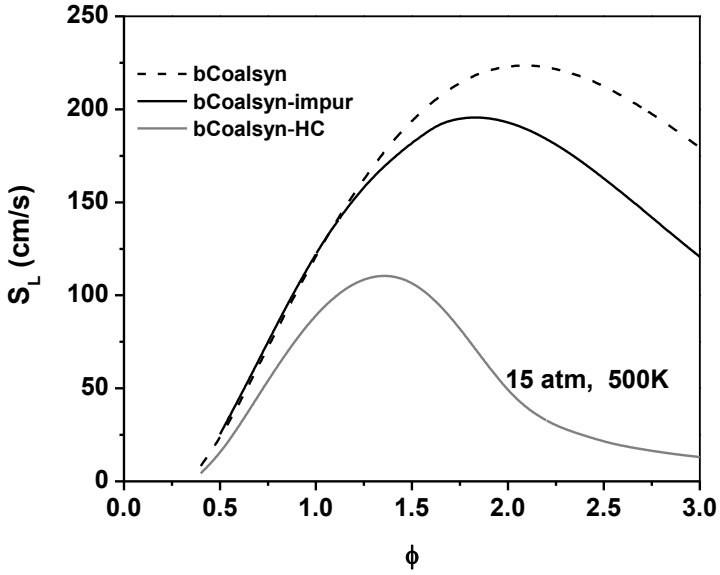

Fig. 21 Laminar flame speed as a function of equivalence ratio for a baseline coal syngas with various impurities or hydrocarbons at 15 atm and 500 K as initial conditions.

Impurity Addition to the Average Mixture. A comparison between the ignition delay times of the two averaged mixtures (from coal and biomass) for the three pressure conditions investigated has been made in Mathieu et al. (2013b). Some significant differences between these two mixtures were observed due to the difference in hydrocarbon composition. The equivalence ratio effect for the two average mixtures is visible in the authors' previous work [Mathieu et al., 2013b].

The effects of impurity addition on the ignition delay time of the average bio-syngas mixture at 1 atm are visible in Fig. 22. It is visible from this figure that, as for the baseline mixtures, only NO_2 has an effect on the ignition delay time. Indeed, ignition delay times are notably decreased below 1000 K in the presence of NO_2; the amplitude of this decrease being proportional to the concentration of NO_2 at the authors' conditions. The ignition delay times for the mixture with all the impurities are similar to the ones from the high NO_2 concentration mixture, indicating a lack of effect of NH_3, HCN, and SO_2.

At 10 atm, Fig. 23, the trends are similar to those described at 1 atm (decrease of the ignition delay time on the low-temperature side, for NO_2 only). The decrease in the ignition delay time was relatively small and was observed only for temperatures below 1250 K.

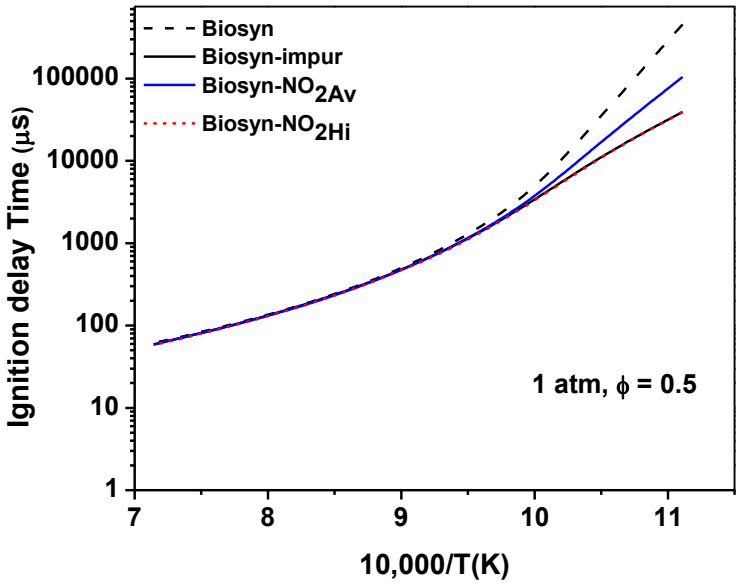

Fig. 22 Effect of various impurities on the ignition delay time for an average bio-syngas mixture at 1 atm.

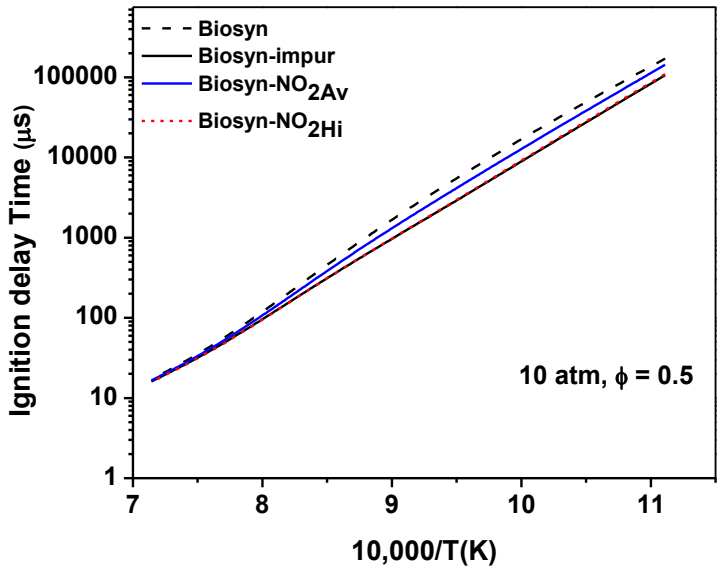

Fig. 23 Effect of various impurities on the ignition delay time for an average bio-syngas mixture at 10 atm.

As can be seen for the case at 35 atm in Fig. 24, effects of impurities on the ignition delay time are relatively small at these conditions. Again, only NO_2 has an effect (enhancing reactivity) on the ignition delay time. This effect is however distributed nearly equally along the range of temperatures investigated.

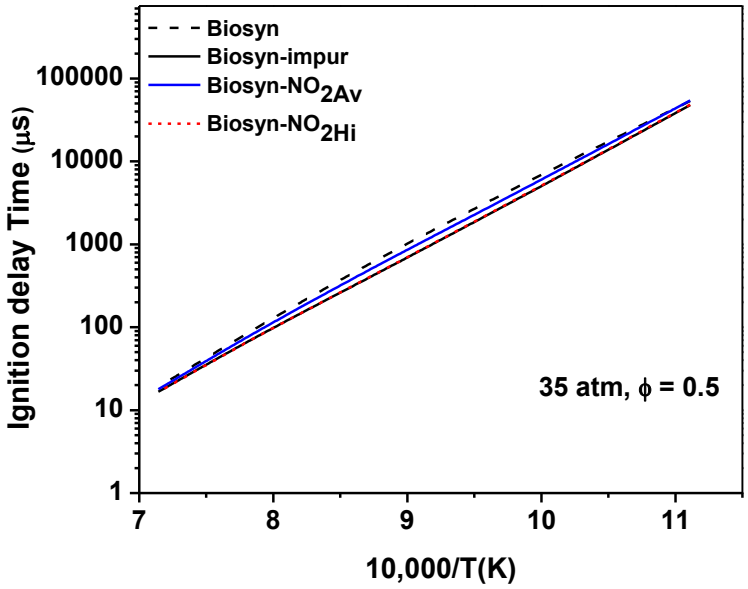

Fig. 24 Effect of various impurities on the ignition delay time for an average bio-syngas mixture at 35 atm.

The effects of impurities on the Coalsyn mixture at 1 atm are visible in Fig 25. As can be seen, the average concentration of H_2S has no effect on the ignition delay time at this condition. The ignition delay time is however notably increased for temperatures above 975 K by a factor between 2 (1400 K) and 5 (1050 K) for the highest H_2S concentration. The calculations yield the same result for the Coalsyn-impur mixture, indicating that the other impurities have no effect overall.

At 10 (Fig. 26) and 35 atm (Fig. 27), the results obtained with the lowest concentration of H_2S investigated are without effect. However, a noticeable effect on the ignition delay time is exhibited by the high H_2S concentration and, again, no further effect is seen with all impurities. At 10 atm, the H_2S addition decreases the ignition delay time below 1225 K and increases it above this temperature. At 35 atm, ignition delay times are not changed by the impurity addition at 1400 K. However, below this temperature, a noticeable decrease can be observed with the highest H_2S concentration, this decrease being larger as the temperature decreases.

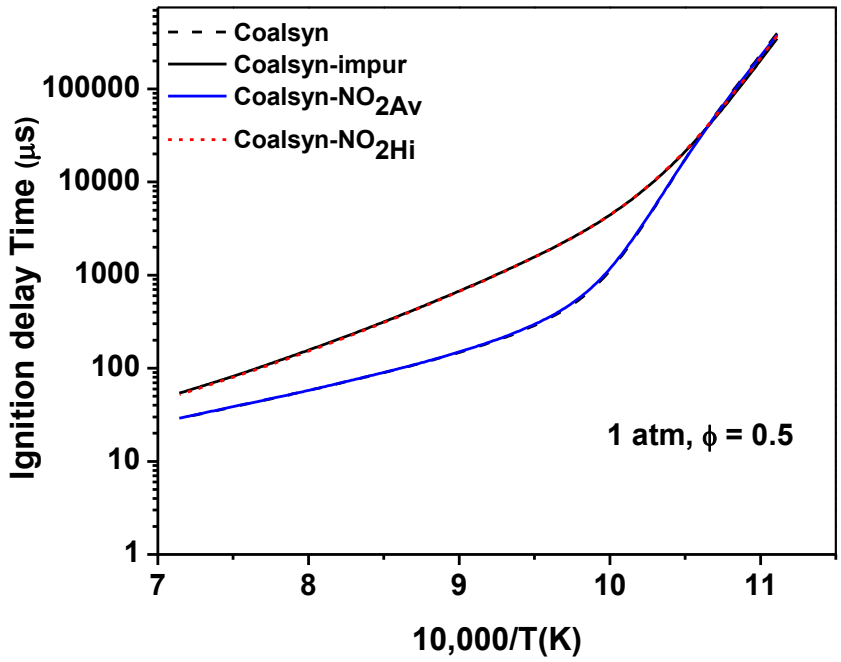

Fig. 25 Effect of various impurities on the ignition delay time for an average coal-syngas mixture at 1 atm.

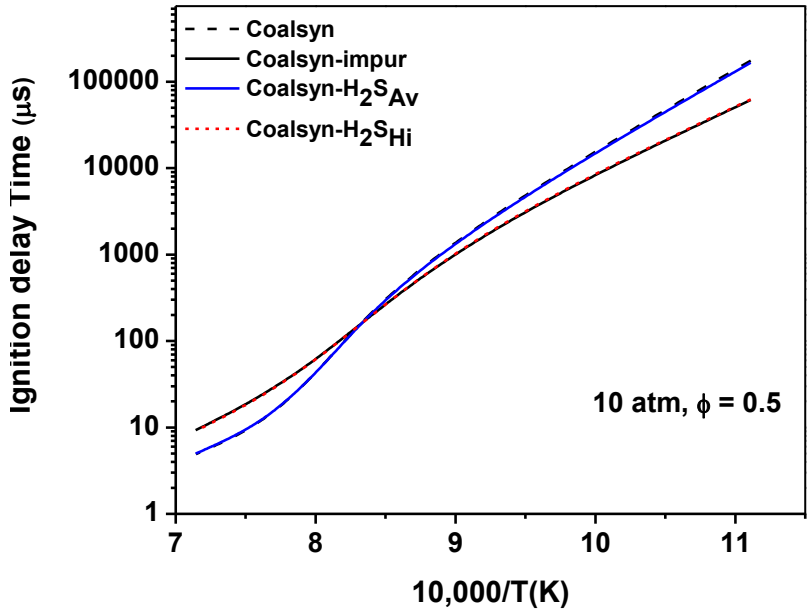

Fig. 26 Effect of various impurities on the ignition delay time for an average coal-syngas mixture at 10 atm.

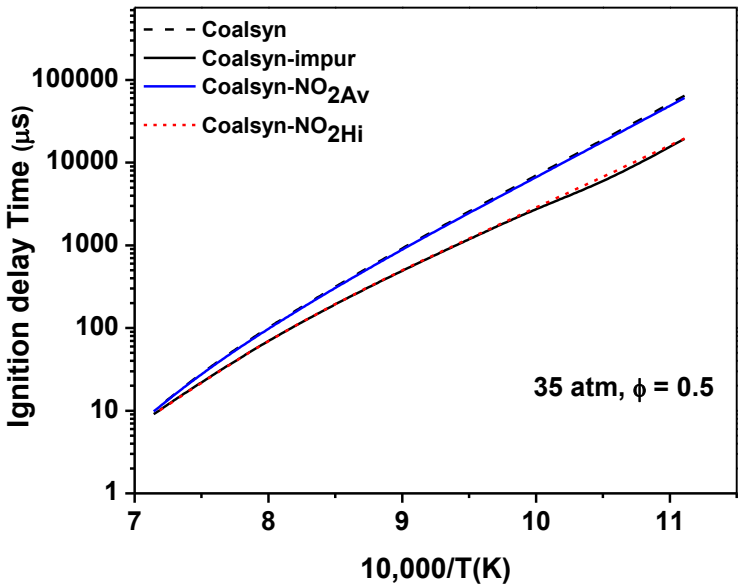

Fig. 27 Effect of various impurities on the ignition delay time for an average coal-syngas mixture at 35 atm.

The effects of impurities on the laminar flame speed of an average coal syngas mixture, with initial conditions of 1 atm and 500 K, are visible in Fig. 28. As can be seen, the smallest H_2S concentration investigated does not exhibit any effect on S_L. A noticeable decrease (around 5%) in the laminar flame speed is however observed with the high H_2S concentration for fuel rich conditions. The laminar flame speed is further reduced (by around 9% total) when all the impurities are in the mixture.

At higher pressure, Fig. 29, laminar flame speeds are significantly smaller, with a reduction higher than 50% due to the initial pressure increase. Impurity effects are the same as for the low-pressure case, and the percentage reduction in the maximum laminar flame speed is also the same as for the previous case with lower initial pressure.

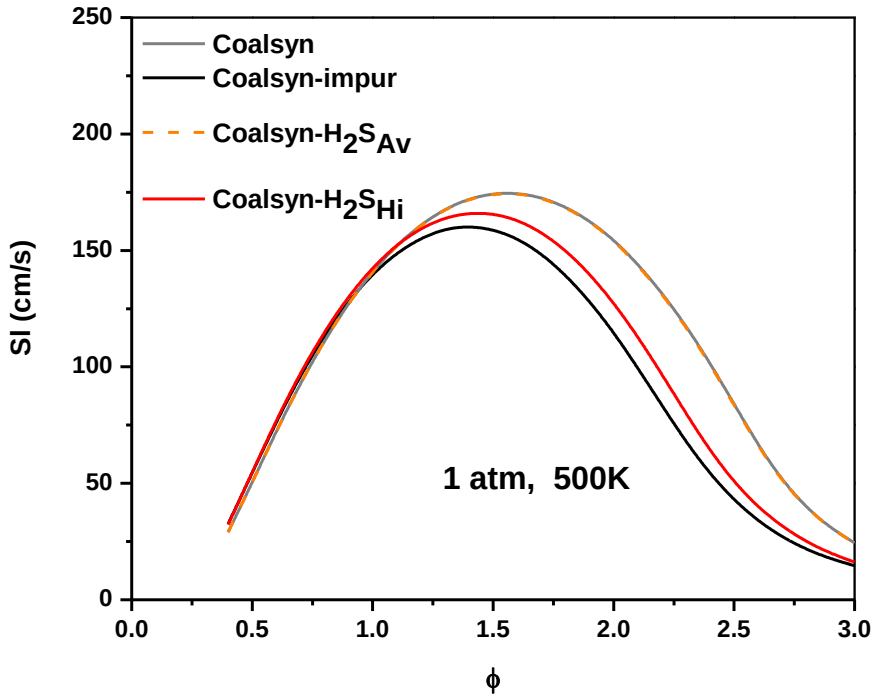

Fig. 28 Effect of various impurities on the laminar flame speed for an average coal-syngas mixture at 1 atm, 500 K as initial conditions.

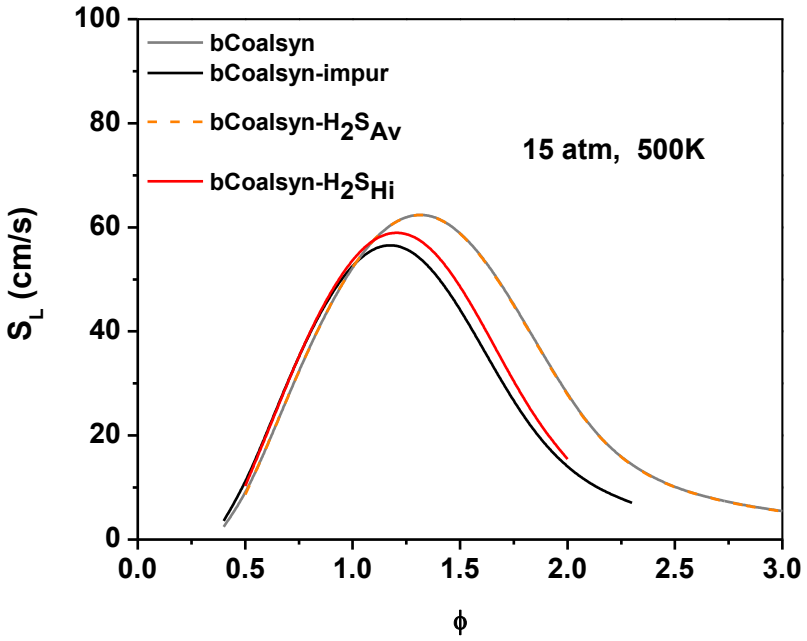

Fig. 29 Effect of various impurities on the laminar flame speed for an average coal-syngas mixture at 15 atm, 500 K as initial conditions.

Discussion. For the bio-syngas mixtures, the results showed that NO_2 was the only impurity to have an effect on the ignition delay time. This effect is present only when the low-temperature chemistry of H_2 rules the combustion (i.e. when the HO_2 radical dominates over OH). This behavior indicates a purely chemical mechanism due to the reaction NO + HO_2 ⇄ NO_2 + OH (r3) (NO_2 being mostly converted to NO by the reaction NO_2 + H ⇄ NO + OH (r4)). The OH radicals produced then oxidize the hydrogen via OH + H_2 ⇄ H_2O + H (r5), and this reaction then allows recycling NO via r4. This catalytic effect of NO_2 which transforms HO_2 into OH explains the large effects observed on the ignition delay time, when the low-temperature chemistry was dominating. The lack of effect of NO_2 on the flame speed, where the high-temperature chemistry of H_2 dominates, associated with the unmodified flame temperature, confirms the chemical role of NO_2.

For the coal baseline syngas, H_2S is the only contaminant that has an influence on the ignition delay time. An effect on the laminar flame speed was observed too, with the highest impurity concentration studied. The inhibiting effect occurring at high temperature or with the laminar flame speed is due to the reaction H_2S + H ⇄ SH + H_2, (r6) which occurs before the ignition and inhibits the dominating reaction H + O_2 ⇄ OH + O (r1) and reduces the overall reactivity of the mixture. The H_2S can therefore be viewed as a sink for H radicals, preventing r1 to take place and to trigger the ignition. The absence of change in the flame temperature, even for the highest H_2S concentration investigated, indicates a purely chemical effect of H_2S on the laminar flame speed. At this condition, the high-temperature mechanism via r6 is responsible for the decrease in the mixture's reactivity. For the conditions where H_2S is promoting the reactivity on the ignition delay time, this result can be explained by the fact that H_2S reacts with radicals (H, O, OH, and HO_2) to give SH + products, and this radical consumption limits the important reactions for H_2 oxidation,

namely $H + O_2 \rightleftarrows OH + O$ (r1) and $H + O_2 + M \rightleftarrows HO_2 + M$ (r2), the latter being more important at these conditions. Most of the SH will then either quickly form SO which will then form SO_2 via the reaction $SO + O_2 \rightleftarrows SO_2 + O$ or react through $SH + SH \rightleftarrows H_2S + S$ (r7). The S produced will then react through $S + O_2 \rightleftarrows SO + O$ (r8) and $SO + O_2 \rightleftarrows SO_2 + O$ (r9).

To summarize, at conditions where r2 dominates, the formation of HO_2 is limited by the presence of H_2S via the consumption of H radicals (r6) whereas the SH produced will then lead to the formation of O radicals via r8 and r9. These O radicals will then react through $O + H_2 \rightleftarrows OH + H$ (r10) and, overall, promote the reactivity of the mixture compared to the conditions where r2 was dominant, without H_2S.

Although NH_3 and HCN did not exhibit any effect on the ignition delay time, these components reduced the flame speeds for the baseline mixtures, mostly on the fuel rich side. These inhibiting effects are purely chemical effects as the laminar flame temperature is nearly unchanged by the presence of these components. This result is visible for the NH_3 case in Fig. 31, where all the adiabatic flame temperatures are the same for a given equivalence ratio, regardless of the nature or concentration of the contaminants. Note that this outcome is also true for the other conditions investigated, including the baseline coal mixture. The chemical analysis showed that this inhibiting effect is chiefly due to the consumption of OH radicals, leading to water and a less-reactive radical (such as NH_2 for NH_3 or SH for H_2S). Overall, the reactive OH radicals are then replaced by less-reactive ones, slowing down the reactivity. This effect is particularly visible at fuel rich conditions, where there is already a shortage of oxygen to complete the combustion of all the fuel molecules.

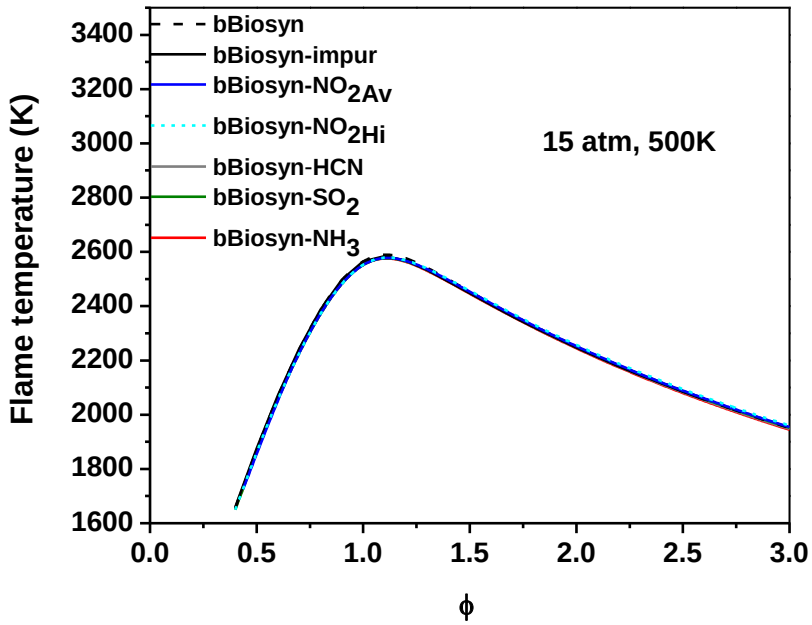

Fig. 31 Effect of various impurities on the adiabatic flame temperature for an average bio-syngas mixture at 15 atm, 500K as initial conditions.

Laminar Flame Speed Measurements with Hydrocarbon Impurities

Synthetic gas, or syngas, is a mixture primarily composed of CO and H_2. This high-hydrogen combination causes it to be an attractive fuel for power generation through gas turbines. However, the concentrations of each species will vary depending on the feedstock and the process used to gasify it. In the ideal case, the syngas mixture would just consist of CO and H_2, but rarely is the mixture this simple. As the composition of syngas can vary greatly, it is important to look at all possible and likely impurities individually to fully understand their effects. This approach will allow gas turbine manufactures the freedom to design safe and efficient turbines that can operate with a variety of syngas mixtures.

Previous studies have shown that there are several impurities that can be present in typical syngas blends. A recent detailed study by the authors focused on the effects of nitrogen- and sulfur-based impurities [Mathieu et al., 2014a]. A detailed review of all previous studies of syngas mixtures can be found in Lee et al. (2014). However, the individual effects of small hydrocarbons, commonly found in syngas mixtures have not been well studied experimentally with respect to fundamental combustion parameters such as laminar flame speed and ignition delay time. The recent modeling study by Mathieu et al. (2014a) built upon their results presented previously [Mathieu et al., 2014b], where the previous work had looked specifically at the effects of hydrocarbon addition to syngas for fuel-air mixtures at engine conditions from a numerical perspective. They found that realistic levels of smaller hydrocarbons present in the syngas fuel blend, up to about 15% by volume, can significantly decrease the laminar flame speed by as much as a factor of two in some cases. The current study builds on the flame speed and ignition delay time modeling research of Mathieu et al. (2014a) to gain an experimental understanding of the effects of hydrocarbon impurities on the flame speed of syngas mixtures and to help validate the chemical kinetics mechanism. The present study therefore focuses on the hydrocarbons shown in Mathieu et al. (2014a) to be present in the largest concentrations and to have the greatest impact on the flame speed, namely methane and ethane.

Presented in this section of Task 3 are the results of new experiments for syngas-based laminar flames speeds with and without hydrocarbon impurities along with the results of a modern chemical kinetics model. The mixture compositions of interest herein are covered first, followed by details of the experimental setup and procedure. Details on the experimental results and a comparison of them to the predictions of the kinetics model are then given. Some discussion on the thermal-diffusive nature of the flames for the various blends as well as an analysis of the chemical kinetics are also provided in a discussion section.

Mixtures Investigated. As mentioned above, the mixtures chosen in this study were based off of an earlier numerical studies done by the authors' groups [Mathieu et al., 2014a; 2014b]. This prior study included two baseline syngas mixtures. These blends were chosen to represent a nominal Coal syngas and a nominal Bio-syngas fuels. The Coal syngas has a 60/40 ratio of CO to H_2, while the Bio-syngas has a 50/50 ratio. Hydrocarbons were then added to each mixture while holding the ratio of CO to H_2 constant. The hydrocarbons chosen for further study were the ones predicted to have the most-significant impact on the laminar flame speed. A detailed breakdown of the resulting mixtures tested in the present study is shown in Table 3.

As seen in Table 3, the two hydrocarbons investigated in this study were methane and ethane. Methane was found to have the greatest presence in the syngas mixtures, reaching 15% for bio-syngas and 7.4% for the coal-derived syngas. Model predictions showed that this large percentage of methane would have a significant impact on the flame speed [Mathieu et al., 2014b]. Ethane was chosen not because it comprised a large percentage of the fuel, 0.8% for bio-syngas and 1.7% for coal syngas, but because of the significant reduction in flame speed prediction that the small percentage of ethane was predicted to cause.

Table 3 Syngas mixtures with HC impurities.

Mixtures Investigated (Mole Fraction)				
Mixture	H_2	CO	CH_4	C_2H_6
Coal-Neat	0.400	0.600	--	--
Coal-1.6% CH_4	0.3936	0.5904	0.016	--
Coal - 7.4% CH_4	0.3704	0.5556	0.074	--
Coal – 1.7% C_2H_6	0.3932	0.5898	--	0.017
Bio-Neat	0.500	0.500	--	--
Bio-5% CH_4	0.475	0.475	0.050	--
Bio-15% CH_4	0.425	0.425	0.150	--
Bio-0.8% C_2H_6	0.496	0.496	--	0.008

This study investigated the high and low extremes of methane found to be present in syngas mixtures. For the coal syngas, the two levels of methane investigated were 1.6% and 7.4% of the fuel by volume. The bio-syngas added methane at 5% and 15%. Ethane was added to both syngas mixtures, with a percentage of 1.7% of the fuel for the coal syngas and 0.8% for the Bio-syngas.

Experimental Setup. Experiments were conducted in the high-pressure, high-temperature, stainless steel, constant-volume bomb at Texas A&M University. The design of this vessel is explained in detail in Krejci et al. (2013). The internal dimensions of the vessel are a 31.8 cm diameter and a length of 28 cm. Flames can be measured under near-constant-pressure conditions to a diameter of 12.7 cm.

All mixtures were made using the partial pressure method via a 0-1000 Torr pressure Transducer, and the experiments were conducted at room temperature (296 K ± 2 K). Research grade (99.5% pure) Methane, Ethane, Hydrogen, Carbon Monoxide as well as ultra-high purity (99.999%) Oxygen and Nitrogen were used. For the low-Methane coal syngas and the Ethane mixtures, the respective hydrocarbon and Hydrogen were premixed in a separate mix tank prior to being added to the vessel. All other components were added individually.

Each gaseous mixture was ignited by a central spark ignition system. Experimental data were collected using a high-speed camera (Photron Fastcam SA1.1) and a Z-type schlieren setup. The frame rate of the camera was adjusted as necessary to capture enough frames to successfully analyze each experiment. Frame rates used for this data set ranged from 3,000 to 18,000 fps. Images were processed using an internally developed MATLAB-based edge detection program. The unburned, unstretched flame speed and burned-gas Markstein length were calculated using the appropriate nonlinear method as outlined by Chen (2010). The overall average uncertainty in the measured flame speed herein is estimated to be ± 7.2 cm/s.

Chemical Kinetic Model. The laminar flame speeds in this work have been simulated using AramcoMech 1.3 [Metcalfe et al., 2013], which was developed to describe the oxidation of small hydrocarbon and oxygenated hydrocarbon species. The simulations were performed using the Premix code of Chemkin Pro. To reduce the computational cost, mixture-averaged transport equations were utilized. Thermal diffusive effects were also included. The predictions for the laminar flame speeds of different fuel-mixtures are depicted in Figs. 32 through 36 as lines.

Results. As seen in Fig. 32, the experimental results for the neat mixtures of CO and H_2 match the model predictions very well. As expected, the syngas mixture with the greater amount of hydrogen, i.e. the bio-syngas, produced a flame speed that was on average 20.8 cm/s faster than the coal syngas mixture. Both mixtures saw a peak in flame speed around an equivalence ratio of 2.0. The experimental data for both mixtures stayed very close to the model with differences typically between about 1 and 2 cm/s.

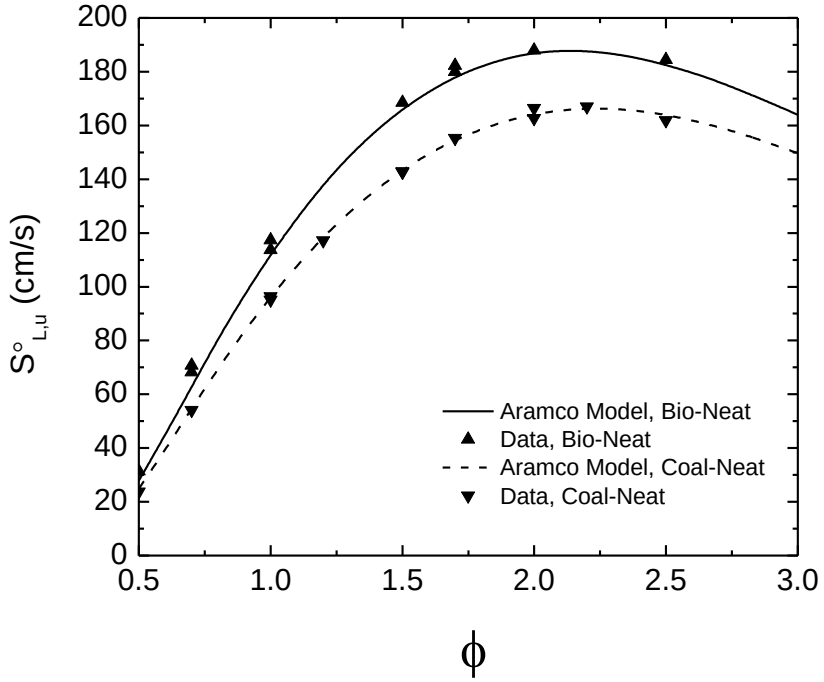

Fig. 32 Laminar flame speeds for the baseline bio-syngas and coal syngas mixtures (Bio-Neat and Coal Neat) at 1 atm and a temperature of 296 K.

As expected, the addition of hydrocarbons to the coal syngas reduced the flame speed. Figure 33 shows the model predictions and the experimental results for these syngas blends. The model predicts well the shape of the flame speed curve and predicts the peak flame speed at the correct equivalence ratio. However, the model under predicts the flame speed for all of the mixtures when hydrocarbons are added. This over prediction is most noticeable at rich mixtures when the model curves deviate from each other, and the effects of the hydrocarbons are more noticeable. On average, the low-methane-concentration (1.6%) model under predicts the flame speed by 2.1%. The next model, with ethane (1.7%), under predicts the flame speed by 10.8%. The greatest

difference was with the highest methane concentration (7.4%), which demonstrated a 17.4% average under prediction of the model. As expected, the greater percentage of hydrocarbons added to the syngas blend the greater reduction in the laminar flame speed. While the low-methane and the ethane mixtures had nearly the same concentration of hydrocarbon addition, 1.6% to 1.7% respectively, the effect of the ethane is noticeably greater.

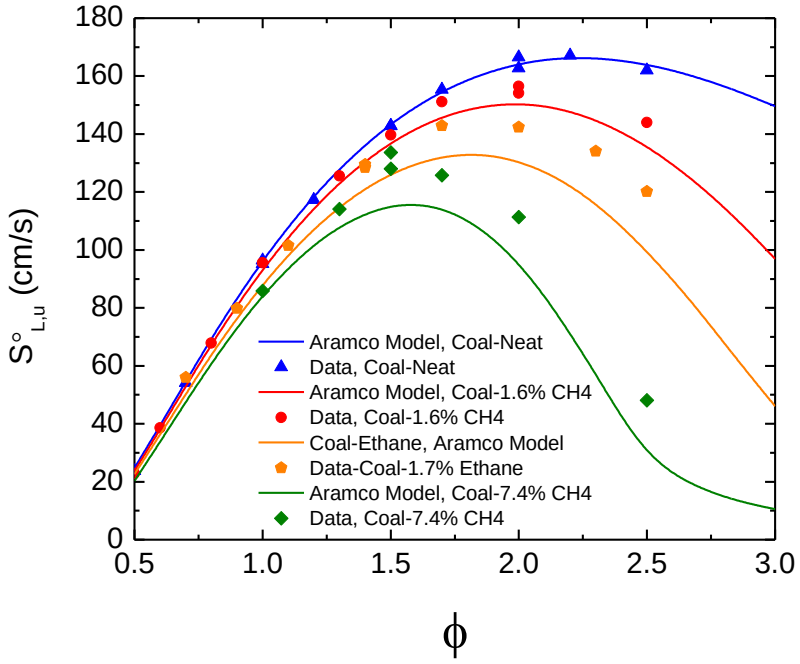

Fig. 33 Laminar flame speeds for coal syngas blends with and without hydrocarbon addition to the baseline mixture at 1 atm and a temperature of 296 K.

Like the coal syngas blends in Fig. 33, the bio-syngas blends also saw a reduction of flame speed with the addition of hydrocarbons. Also like the coal-derived blends, the peak flame speed for the bio-syngas shifted toward an equivalence ratio of 1 as more hydrocarbons were added. The experimental results are plotted in comparison to the model predictions in Fig. 34. For the bio-syngas case, ethane was added in the very small amount of 0.8%. Even in this small amount, it had a significant impact on the flame speed, with a reduction of 11.5 cm/s near the peak equivalence ratio. The model under predicted the flame speed by an average of 7.7%. The low- methane case (5%) saw a reduction in peak flame speed of 34.8 cm/s, with the peak equivalence ratio shifting from $\phi = 2.1$ to 1.7. In general the model under predicts the flame speed by an average of 12.8%. This trend continues for the high-methane case (15%). Here the peak flame speed of 108.2 cm/s was found at $\phi = 1.3$. The model under prediction averages 15.9% for this mixture.

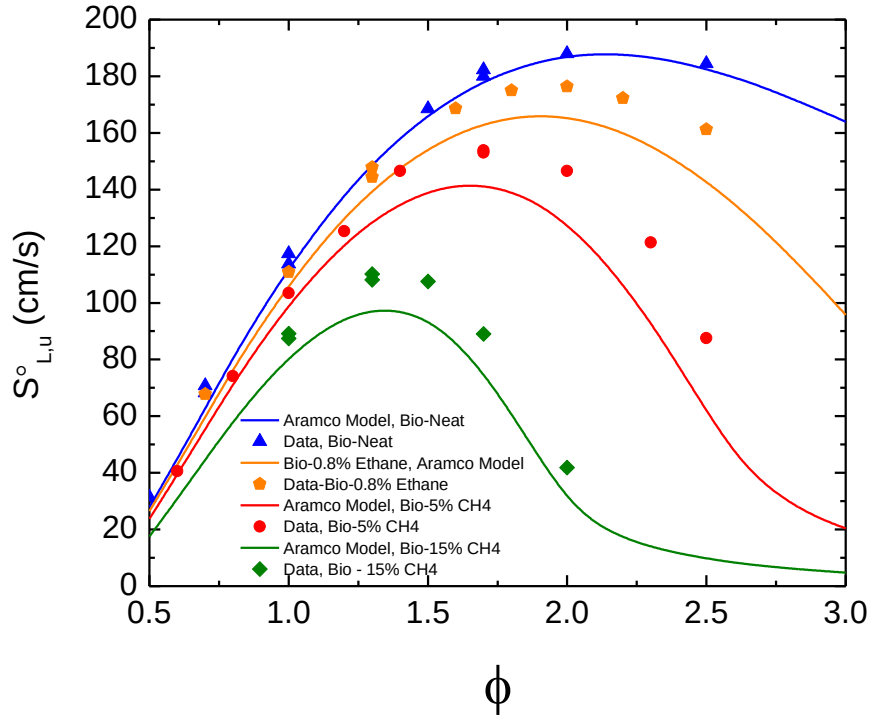

Fig. 34 Laminar flame speeds for bio-syngas blends with and without hydrocarbon addition to the baseline mixture at 1 atm and a temperature of 296 K.

Discussion. Overall, the experimental results agree well with the model predictions. This conclusion is especially true for the neat mixtures in both types of syngas fuel blends. However, the model and the data do not agree as well when methane or ethane is added. The data follow the general shape of the curve predictions, and the peak flame speeds are at the predicted equivalence ratios. On the other hand, the data significantly vary in how far away they are from the model predictions especially at rich conditions. Generally the model is very good for all lean mixtures. While this tendency has been shown for the syngas mixtures investigated in this study, it is important to show that the current model is very accurate at extreme ends of the spectrum in terms of hydrogen at the high end and methane at the lower end. Figure 35 shows the model predictions compared to previous experimental data from the authors [Krejci et al., 2013; Lowry et al., 2011] for pure hydrogen and methane flames in addition to some of the new mixtures in the present paper, the coal syngas results for comparison. As can be seen, the model does very well with pure hydrogen, the neat syngas, and pure methane. The only noticeable disagreement is in the middle when hydrocarbons are added to the syngas blend.

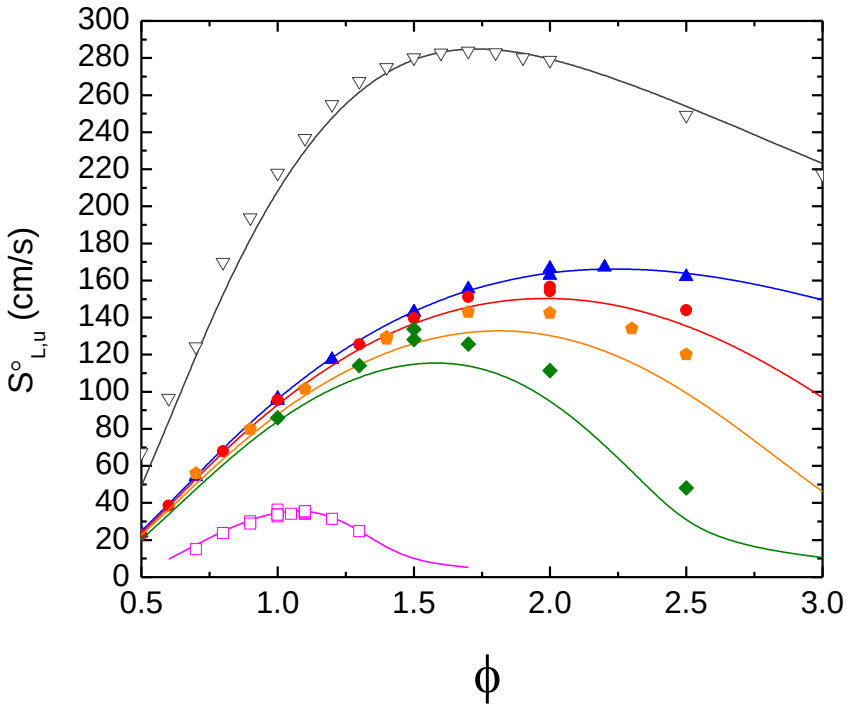

Fig. 35 Laminar Flame Speed Calculations for Hydrogen (gray) and Methane (pink) compared to the results of Coal Syngas in the current study.

Flame Speed Sensitivity Analysis. To determine the important reactions that dominate the flame speeds and control the changes in the chemistry by adding varying quantities of hydrocarbons to the syngas, mixture sensitivity analyses to flame speed were performed. CHEMKIN Pro was used to calculate the first-order sensitivity coefficients for predicting the mass flow rate. The discussions below are based on the sensitivity analyses for Coal Syngas mixtures with 0%, 1.6%, and 7.4% CH_4; and 1.7% C_2H_6, respectively. For each flame, three equivalence ratios of 0.7, 1.4, and 2.1 were selected in the sensitivity analysis to reflect the influence of increasing ϕ.

The flame speed sensitivity analyses for the pure Coal Syngas flames are shown in Fig. 36a. At $\varphi = 0.7$ and $\varphi = 1.4$, the most-sensitive reaction is $CO + OH \leftrightarrow CO_2 + H$. With CO being oxidized, OH radicals are converted to H atoms which further increase flame speed through other chain branching reactions such as $HO_2 + H \leftrightarrow OH + OH$ and $H + O_2 \leftrightarrow O + OH$. The latter reaction is of great significance in the oxidation of hydrogen and all hydrocarbons. Its sensitivity coefficient grows as the equivalence ratio increases, while most other sensitive reactions that increase the reactivity have the opposite trend. At $\varphi = 2.0$, the sensitivity coefficient to $H + O_2 \leftrightarrow O + OH$ is almost equal to that of $CO + OH \leftrightarrow CO_2 + H$. Note that in Coal Syngas the ratio of H_2:CO is 0.4:0.6, therefore higher sensitivity coefficients for this reaction are expected at corresponding conditions in the Bio Syngas flames. Its competitor for H atoms, $H + O_2 (+M) \leftrightarrow HO_2 (+M)$ has a negative sensitivity efficient at lean conditions. However, as the equivalence ratio increases this chain propagating reaction enhances reactivity because it competes with chain terminating reactions such as $H + OH + M \leftrightarrow H_2O + M$ and $HO_2 + OH \leftrightarrow H_2O + O_2$ in which the radicals recombine into molecules and decrease reactivity.

With the adoption of CH_4 in the Coal Syngas, the influence of C_1 chemistry upon the flame speed can be seen in Figs. 36b and 36c, which show the flame speed sensitivity analyses for 1.6% and 7.4% CH_4 in Coal Syngas, respectively. Although CO + OH ↔ CO_2 + H remains the most-sensitive reaction under fuel-lean conditions, its importance decreases markedly as the equivalence ratio increases. In contrast, the chain branching reaction H + O_2 ↔ O + OH becomes more important, especially at higher equivalence ratios when more CH_4 is adopted, as shown in Fig. 39c. This increase in importance of this reaction is mainly due to the competition from the reaction CH_3 + H (+M) ↔ CH_4 (+M) induced by the addition of CH_4 to the fuel mixture. This chain terminating reaction consumes H atoms and therefore greatly decreases the reactivity, which has been shown in the experimental and simulated results as described earlier. As can be seen in Figs. 36b and 36c, this effect becomes more pronounced when the percentage of CH_4 in the fuel is higher. Meanwhile, the reaction CH_3 + O ↔ CH_2O + H shows positive coefficients that increase with φ because this is the major consumption pathway for CH_3 radicals at rich conditions. Moreover, the decomposition reaction HCO + M ↔ CO + H + M also contributes to the consumption of CH_3 radicals through the sequence CH_3 + O = CH_2O + H and CH_2O + R = HCO + RH, and therefore has positive sensitive coefficients. However, the negative effect of CH_4 adoption upon flame speed dominates. The reactivity of the system gets further reduced by the oxidation of CH_4 that starts with H abstraction by the radical pool, consuming the radicals while producing CH_3 radicals.

As the equivalence ratio increases, the chain branching reaction H + O_2 ↔ O + OH is further inhibited because of the lower concentration of O_2 and the enhanced competition from CH_3 + H (+M) ↔ CH_4 (+M). As can be seen in Fig. 36c, at φ = 2.1, these two reactions dominate flame speed with much higher sensitivity coefficients compare to the other reactions. As a result, the flame speed is sharply decreased with increasing φ, leading to the difference between the flame speed profiles for pure Coal Syngas and that with CH_4 adopted. This trend is more obvious for the 7.4% CH_4 condition (Fig. 33), in which case the flame speed becomes very low at φ > 2.5. Note that the flame speeds for the CH_4-adopted mixtures are under-predicted by the model, while that for pure coal gas is well-predicted. This may indicate that the recombination of CH_3 radicals with H atoms, as well as other sensitive reactions such as CH_3 + O ↔ CH_2O + H and H-atom abstraction reactions of CH_4 remain to be refined to improve the performance of the mechanism.

Figure 36d shows the flow rate sensitivity analysis for the 1.7% C_2H_6-adopted Coal Syngas. Although only 1.7% of C_2H_6 is added, the negative effect upon flame speed is quite obvious, as can be seen from both the analysis and the experimental observations. However, the inhibition is mainly from the C_1 chemistry, CH_3 + H (+M) ↔ CH_4 (+M), while C_2 chemistry appears to be of only minor importance. This minor influence of the C_2 chemistry is because after the H abstraction of C_2H_6, the C_2H_5 radical can be readily converted into the CH_3 radical via the reaction C_2H_5 + H ↔ CH_3 + CH_3, which is the major consumption pathway at rich conditions. Therefore the reactions leading to the formation of C_2H_5 radicals show minor contributions to the decrease of reactivity, while the recombination of CH_3 and H plays the key role. The conversion of C_2H_5 radicals into CH_3 radicals itself also has a slight negative effect upon the reactivity because it consumes H atoms. However, CH_3 radicals are a much stronger competitor for H atoms, and two CH_3 radicals are produced from one C_2H_5 radical and an H atom. Thus, the decrease in flame speed is much more obvious than that with 1.6% CH_4 adoption. The model under-predicts the flame speed for the C_2H_6-adopted fuel, especially at high equivalence ratios.

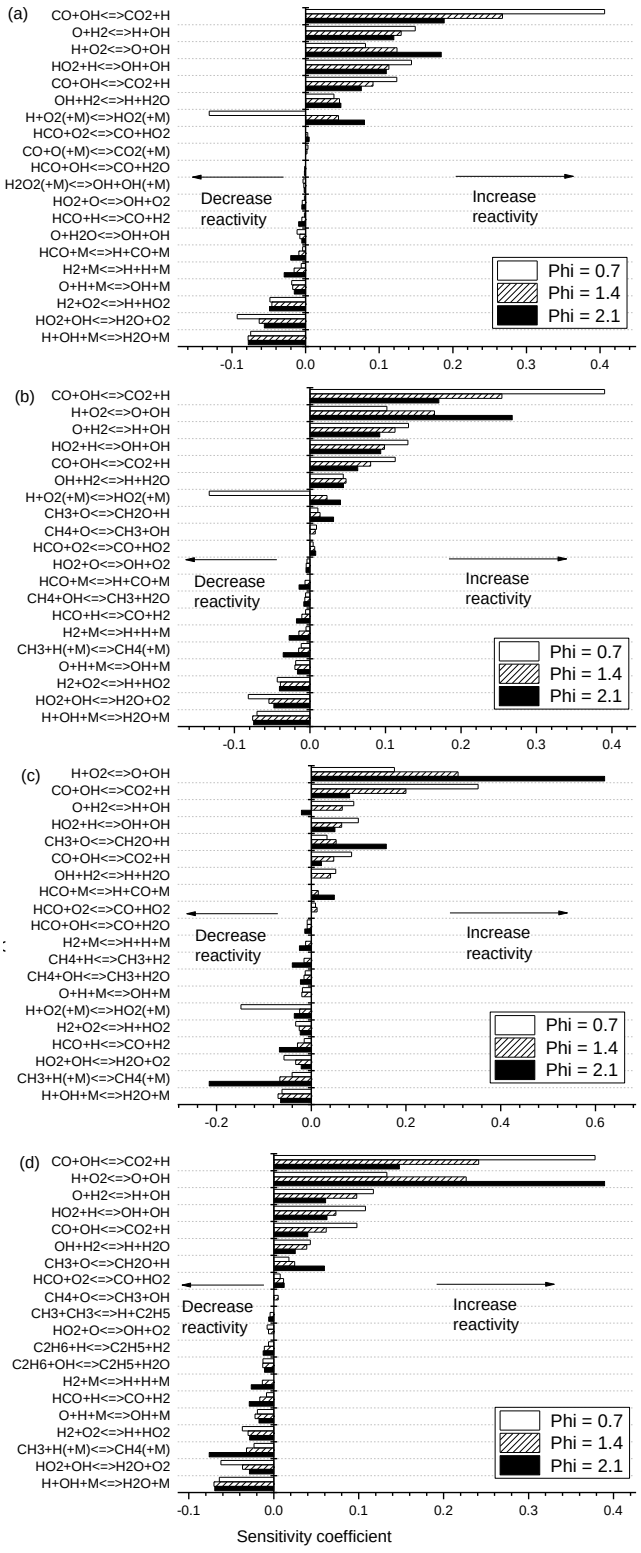

Fig. 36 Flow rate sensitivity analyses of laminar flame speeds for Coal syngas with (a) 0% CH_4, (b) 1.6% CH_4, (c) 7.4% CH_4, (d) 1.7% C_2H_6. Initial conditions 1.0 atm, 296 K, Φ = 0.7, 1.4, and 2.1.

Radiation Effects. The effects of radiation on the flame speed can also be considered. Santner et al. (2014) found the reduction in flame speed due to radiation heat loss from the flame to be small, on the order of a few percent. In the present results, the experimental data are consistently at faster flame speeds than the model predictions, indicating that if a radiation correction were included, the data would move further above (and away from) the predictions. Hence, radiation effects do not explain the current differences between data and model. For the present study, the effects of radiation are neglected.

Image Analysis. Image analysis of the growing flame showed two things. First, leaner mixtures tended to be less stable then rich mixtures, and second, hydrocarbon addition increased the stability of the flame. Figure 37 shows a small but representative selection of recorded images from a wide range of the data collected. These images are examples of trends seen throughout the data set. Note that the electrodes have been removed from the images to make the details of the flames easier to see.

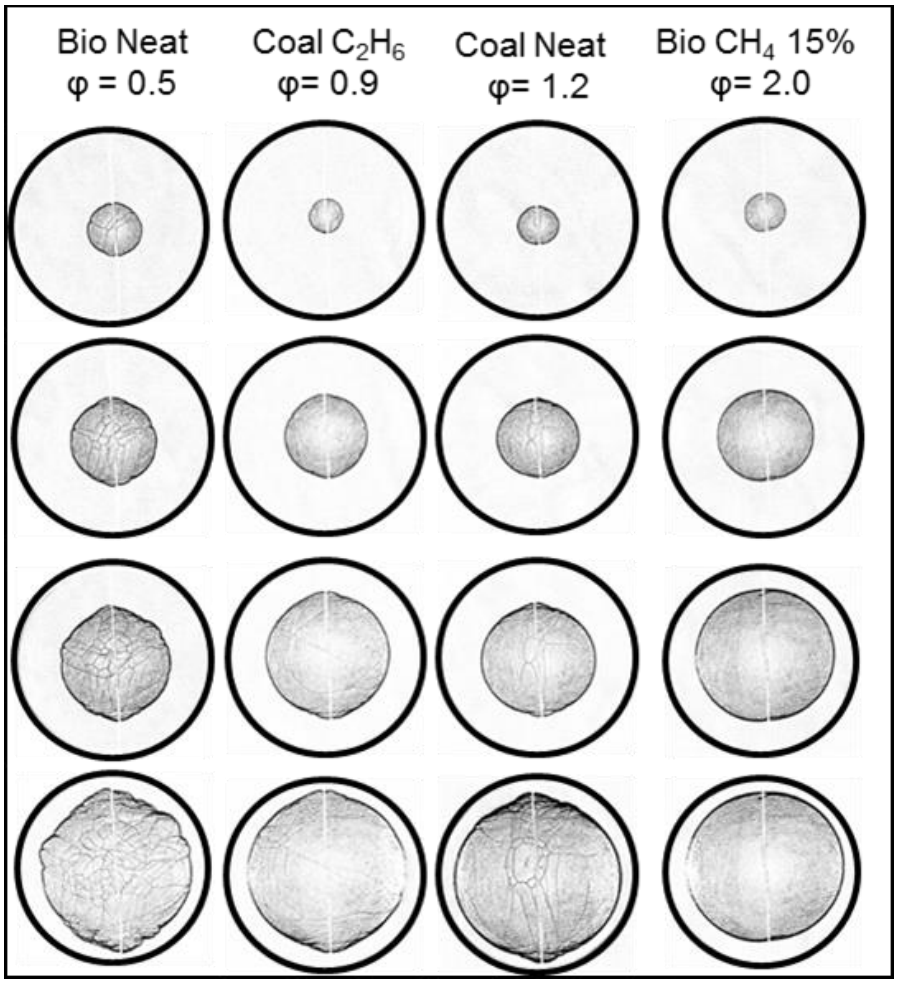

Fig. 37 Sample flame images for four different syngas blends at different equivalence ratios. Time increases in each column from top to bottom.

The flame for the neat bio-syngas blend became unstable almost immediately. This flame is the leanest condition tested, making instability expected per the Markstein lengths and Lewis numbers for these mixtures (see below). Signs of a wrinkled flame are visible in the first of the images shown. By the last images presented in Fig. 37, the flame is very wrinkled, and no longer very spherical. The two coal syngas cases presented are very similar to each other. Both are flames near $\phi = 1$, with the ethane addition being a slightly lean flame ($\phi = 0.9$), and the neat case slightly rich ($\phi = 1.2$). Both of these coal syngas flames are noticeably more stable than the lean bio-syngas. The coal neat flame begins to noticeably show instabilities in the second to last image shown. The coal flame with ethane although at a leaner condition ($\phi = 0.9$) stays stable longer. There might be a slight hint of instabilities beginning in the last of the ethane coal images. The bio-syngas blend with 15% methane is the most stable. The flame stays nearly perfectly spherical throughout the images presented, with no hint of instabilities beginning. Note that the present data for un-stretched, unburned laminar flame speed were derived from the data using a method that determines numerically when the occurrence of instabilities begins to influence (i.e. accelerate) the flame propagation. Therefore, the S_L° data herein do not contain the effects of the instabilities. Further details on this data reduction procedure can be found in Lowry et al. (2011).

Markstein Length. The Markstein lengths for the coal syngas blends showed good agreement across all blends and equivalence ratios investigated. As can be seen in Fig. 38, the Markstein length averaged around 0.05 cm for all mixtures investigated. The only significant deviations from this value range were at the leanest and richest equivalence ratios investigated. Negative Markstein lengths were calculated for the neat mixture at $\phi = 0.5$ and 0.7, and for the low-methane mixture at $\phi = 0.5$ and 0.6. The methane added in the lower case significantly increased the Markstein length and moved the flame closer to being stable. It is also worth noting the significant increase in Markstein length for the higher methane case, at $\phi = 2.5$, which was also the richest case investigated.

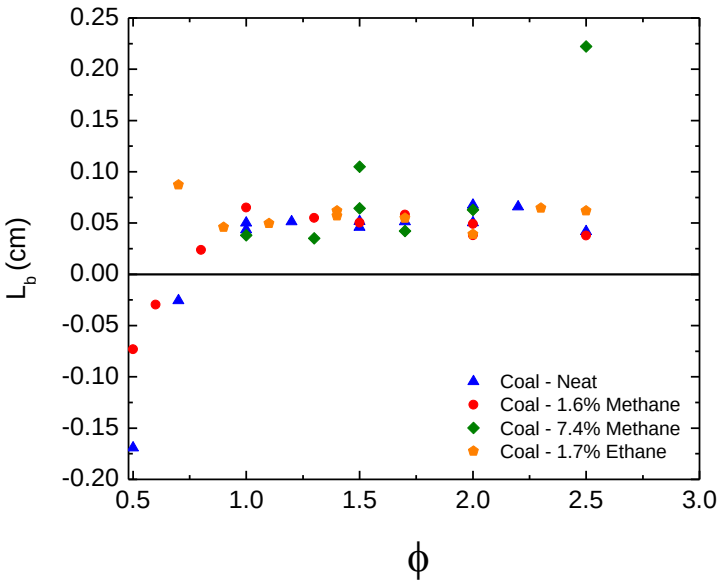

Fig. 38 Burned-gas Markstein Lengths for Coal Syngas Blends with and without hydrocarbon addition to the baseline mixture at 1 atm and initial temperature of 296 K.

The Markstein lengths for the bio-syngas mixtures investigated showed similar trends. Over a majority of the equivalence ratios investigated, all mixtures had an average Markstein length just over 0.06 cm. As can be seen in Fig. 39, the greatest variance was at the leanest and richest equivalence ratios. Like the coal syngas blend, the high-methane mixture returned a relatively large Markstein length for the richest case investigated. The Markstein lengths calculated in this study for the neat mixture are close to those reported by Prathap et al. (2008) for syngas blends.

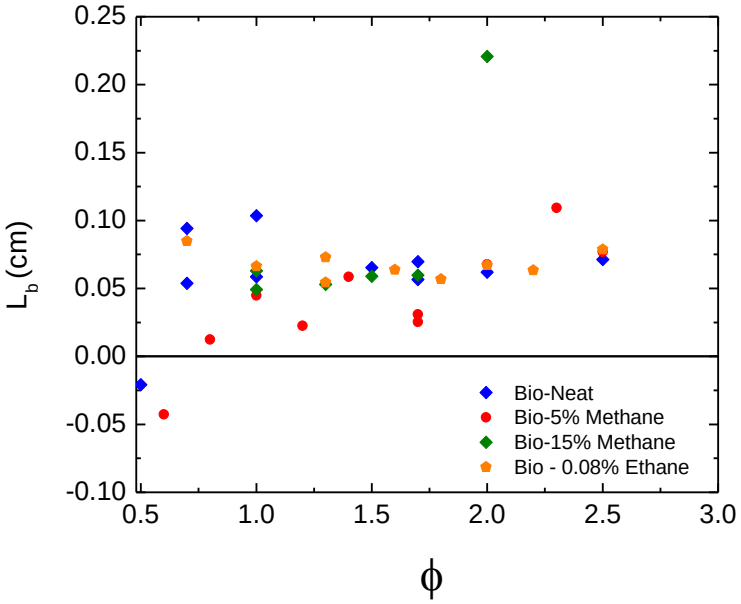

Fig. 39 Burned-gas Markstein Lengths for Bio-Syngas Blends with and without hydrocarbon addition to the baseline mixture at 1 atm and initial temperature of 296 K.

Lewis Number. Calculating the Lewis number of a fuel mixture can vary from study to study in the literature depending on the definition used. Bouvet et al. (2013) found that there were several proposed, effective Lewis number-formations that could be used in fuel mixtures. In the present study, Lewis numbers were calculated using the chemical equilibrium function in COSILAB, and the volumetric-based effective Lewis number calculation from Bouvet et al. (2013).

As was seen with the Lewis Number of pure hydrogen in air in the study by Hu et al. (2009), Le jumps from below unity to above unity as the mixture crosses $\phi = 1$. This step increase is due to the deficient species changing from the fuel in the mixture to the oxygen as the mixture stoichiometry changes from fuel lean to fuel rich.

The Lewis numbers for the coal-derived blends are shown in Fig. 40. There is very little deviation amongst the Lewis numbers of the lean mixtures. All the blends were found to have a relatively constant Lewis number throughout the lean equivalence ratios investigated, near 0.75. As hydrocarbons were added, the Lewis number slightly increased, moving it toward unity. The same trend can be seen in the bio-syngas blends, shown in Fig. 41. However as there is more hydrogen in the mixtures, and over twice as much CH_4 in the rich case, the Lewis numbers deviate slightly

more for those mixtures. The Lewis number values less than unity on the lean side tend to support the trends mentioned above wherein the leaner flames tended to be less stable.

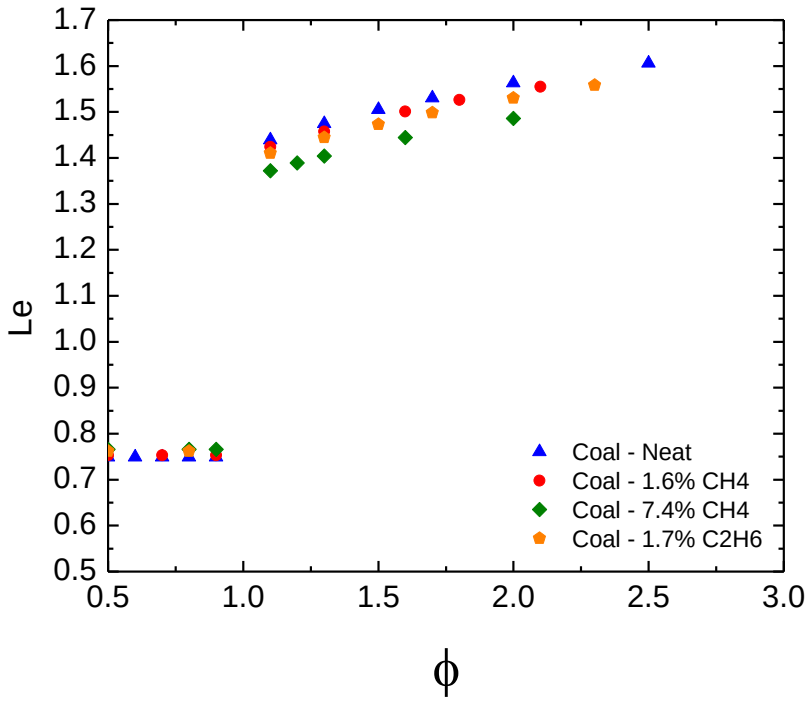

Fig. 40 Lewis Numbers for Coal Syngas Blends with and without hydrocarbon addition at various equivalence ratios at 1 atm and 296 K.

The Lewis numbers for the fuel rich equivalence ratios show a similar trend. Like the fuel lean cases, it was found that the addition of hydrocarbons moved the Lewis number closer to unity. Similar to the flame speed, the effects of the hydrocarbon addition are much clearer at the fuel rich equivalence ratios. The Lewis number was also found to increase for all mixtures as the equivalence ratio increased, ranging from values near 1.4 to 1.6 ($\phi = 2.5$).

The Lewis Number of all syngas mixtures in this study is closer to 1.0 than are the Lewis numbers for pure Hydrogen reported in Hu et al. (2009). For their lean mixtures, they found the Lewis number to be around 0.3, and for the rich mixtures around 2.0. Therefore, the most-significant impact on the Lewis number is the addition of the carbon monoxide, which also has a significantly greater concentration in the fuel blends then any of the hydrocarbons added to the neat syngas mixtures.

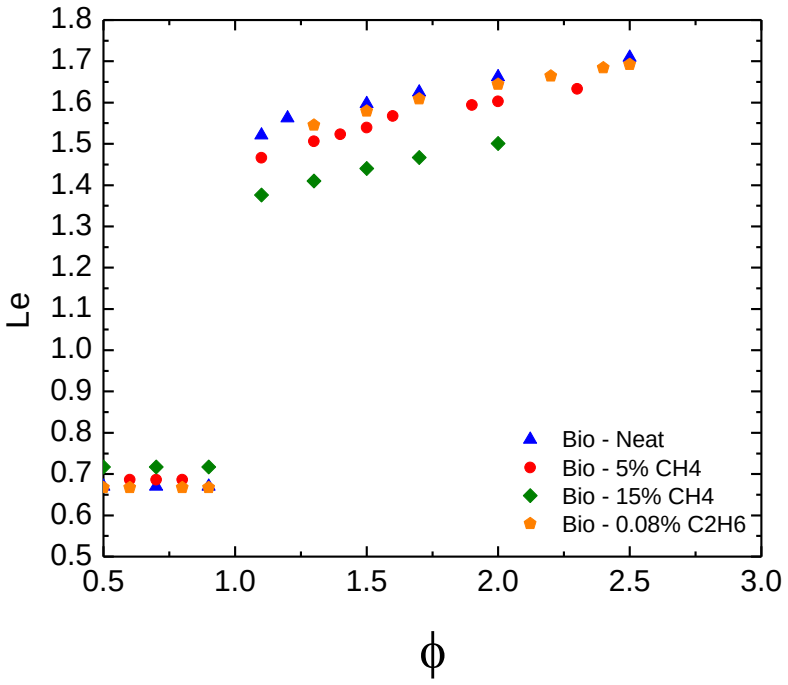

Fig. 41 Lewis Numbers for Bio-Syngas Blends with and without hydrocarbon addition at various equivalence ratios at 1 atm and 296K.

Effect of H_2S Impurities on Syngas Laminar Flame Speeds

Table 4 shows the mixtures that were studied. They are centered on a baseline mixture of "coal" syngas, used by our group in earlier studies, where the CO/H_2 ratio is 60/40. The results for laminar flame speed and Markstein length are shown in Figs. 42-45. A difference in these tests however is the fact that the diluent species is Argon instead of Nitrogen. This use of Ar is because the mixture containing H_2S that was readily available at TAMU was with H_2S diluted in Argon. One advantage of this switch in diluent is that the effect of Argon on the flame speed kinetics can be assessed. The ratio of Argon to O_2 in the oxidizer (85.5/14.5) was chosen to match the adiabatic flame temperature observed for regular air over the same range of fuel-oxidizer equivalence ratios. Figure 44 shows a comparison of the Argon- and N_2-based baseline mixtures, with no H_2S. Note that the flame speeds with Ar are markedly lower than those with N_2. In general, the addition of H_2S seems to change the flame speed on the lean side very little, while there is a slight decrease in laminar flame speed on the rich side.

Table 4 Mixtures for the flame speed experiments with H_2S across all equivalence ratios.

Mixture	Fuel			Oxidizer		
	CO	H_2	H_2S	O_2	N_2	Ar
Coal-Neat, Air	0.6	0.4	-	0.21	0.79	-
Coal-Neat, Argon	0.6	0.4	-	0.145	-	0.855
Coal - 1% H_2S, Argon	0.594	0.396	0.01	0.145	-	0.855

The chemical kinetics model (NUI Galway's AramcoMech) seems to predict the trends rather well, including the decrease in flame speed with Argon compared to N_2 and the decrease due to H_2S on the rich side. However, the model in general over predicts the flame speed by a few percent, more notably on the rich side (Fig. 21). The model agrees much better with the data for the air mixture as oxidizer, as seen in Fig. 44.

As seen in Figs. 43 and 45, the H_2S has little effect if any on the Markstein length. Similarly, there is little difference between the N_2 and Ar inert species within the scatter in the data. Further analyses are underway.

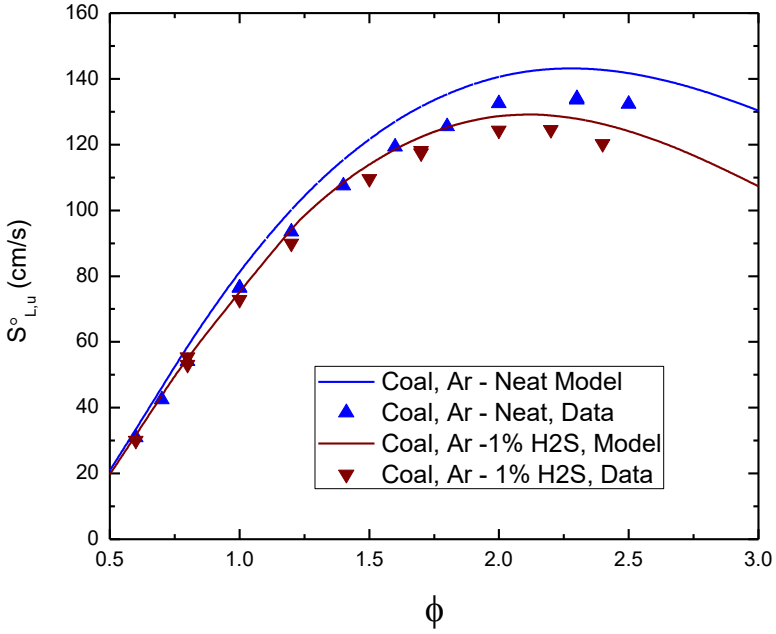

Fig. 42 Model Predictions and Experimental Data for Coal Syngas (60/40 CO/H_2) mixtures in 14.5/85.5 O_2/Ar at 294 K and 1 atm. The model appears to under-predict the effect of argon as the diluent, while it over-predicts the effect that 1% H_2S in relation to the baseline data.

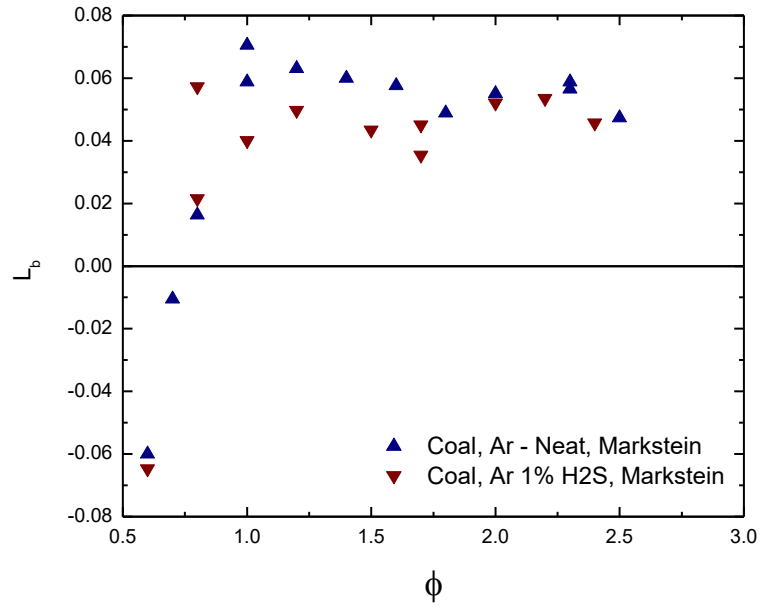

Fig. 43 Burned-gas Markstein lengths calculated for Experimental Data points. Scatter in data are similar to what has been previously seen. Addition of H_2S slightly decreases the Markstein length.

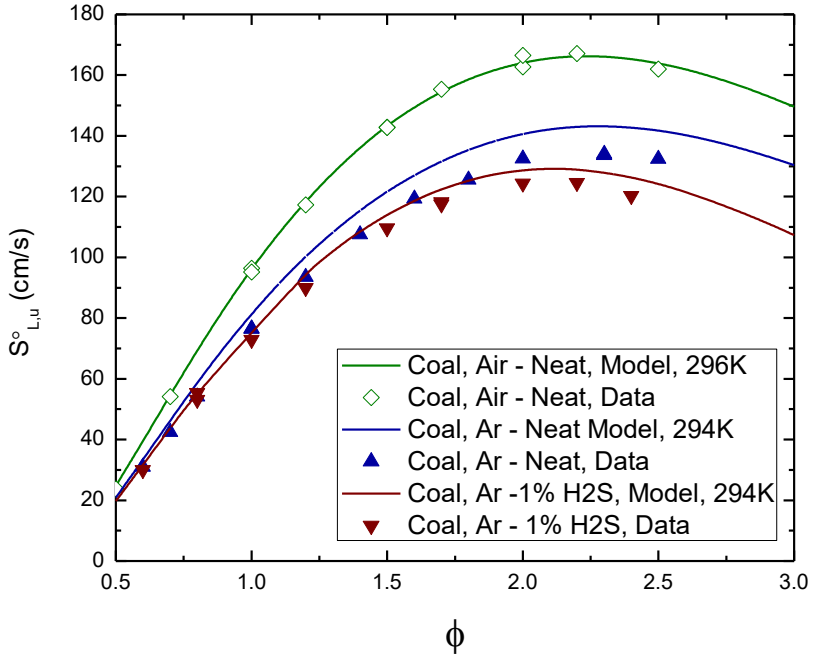

Fig. 44 Model Predictions and Experimental Data plotted in comparison to previous data of Coal Syngas in Air at 296 K.

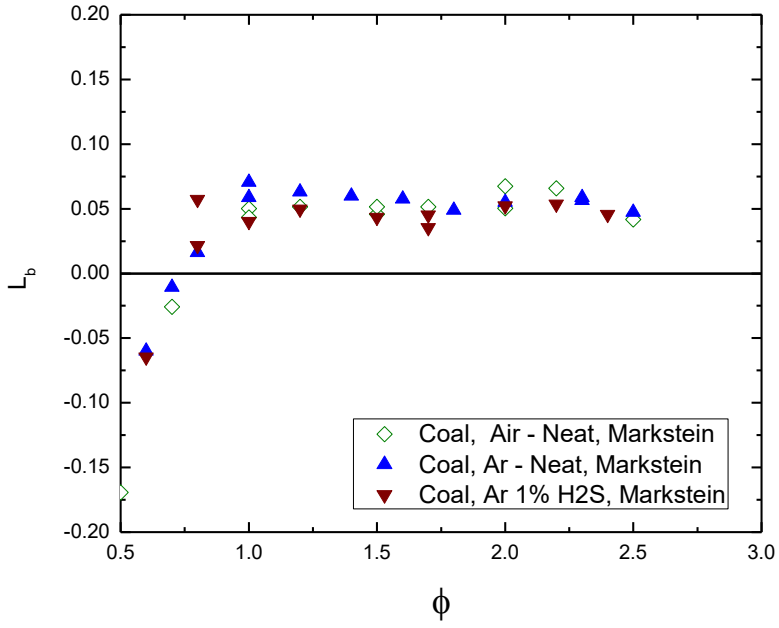

Fig. 45 Burned-gas Markstein lengths from current study compared to those of Coal Syngas in air. Markstein lengths show good agreement with similar trends and scatter.

Hydrogen Sulfide Oxidation Kinetics and Measurements

Experiments on H_2S oxidation have been performed in two of the shock tubes at TAMU during this second year of the project. The mixtures were composed of H_2S and O_2 highly diluted in 98% Ar by volume, with equivalence ratios (ϕ) of 0.5, 1.0, and 1.5. Measurements included ignition delay times using OH* chemiluminescence. Figure 46 shows a typical OH* time history in comparison with the current kinetics model, currently under development at TAMU. Additional experiments were performed wherein the concentration of H_2O was measured using a tunable diode laser near 1.38 microns. Figure 47 shows a schematic and photograph of the laser diagnostic setup at the shock tube. Figure 48 compares typical water time histories for $\phi = 1$ for a range of temperatures, and Fig. 49 compares H_2O concentrations at around the same temperature (about 1780 K) but for the three different equivalence ratios. Figure 50 shows a comparison of the OH* signal with the H_2O signal for the same experiment. Note that water begins to form prior to the main ignition event, as defined by the sharp rise in OH*. The rise in temperature due to the chemical reaction was incorporated into the measured H_2O time histories through its effect on the H_2O absorption coefficient. The ignition delay time results are shown in Fig. 51.

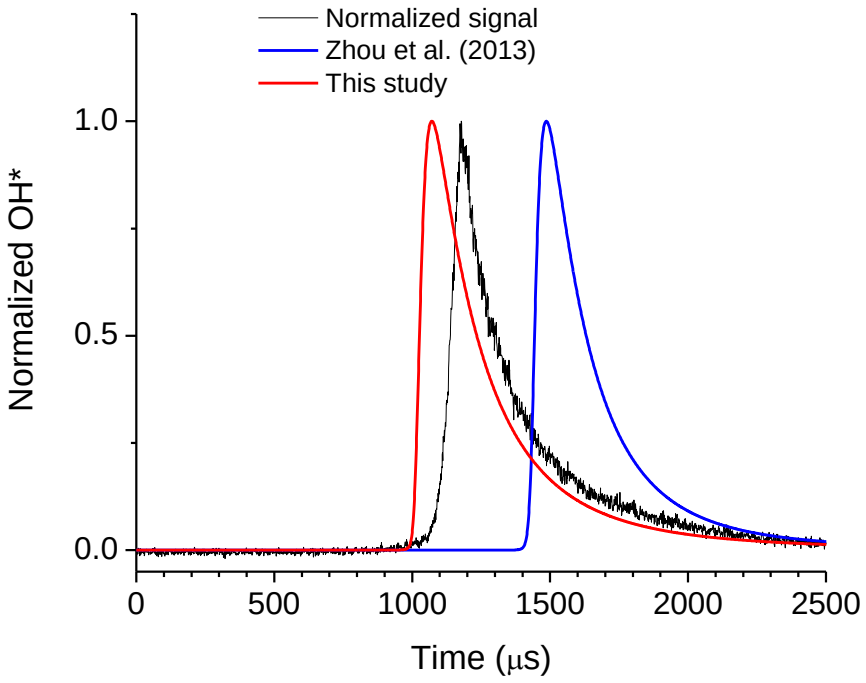

Fig. 46 Measured OH* time history from the shock-tube experiments (1611 K, $\phi = 1$, 1.2 atm, 98% Ar) compared to the current model and that of Zhou et al. (2013). Ignition delay time is defined as the intersection of the steep rise in OH* with the initial value (in this case around 1050 μs).

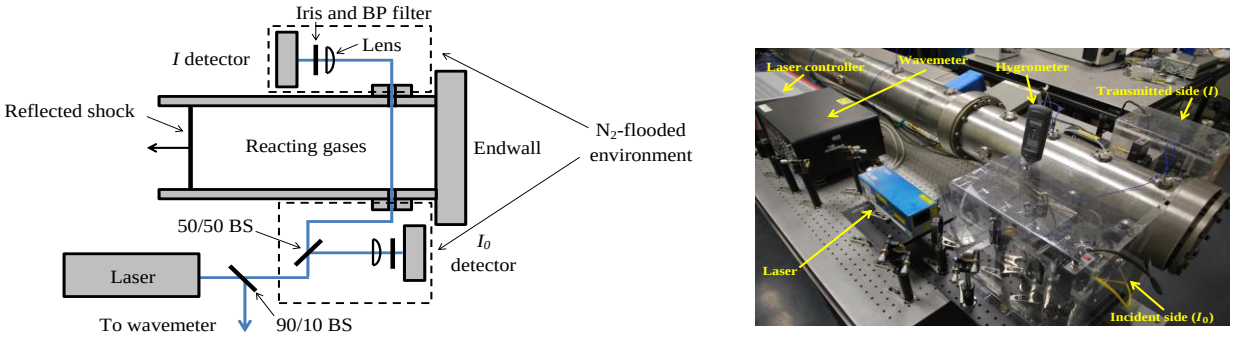

Fig. 47 Infrared diode laser absorption setup used to measure water concentration in the shock tube. Schematic diagram (left) and photograph (right).

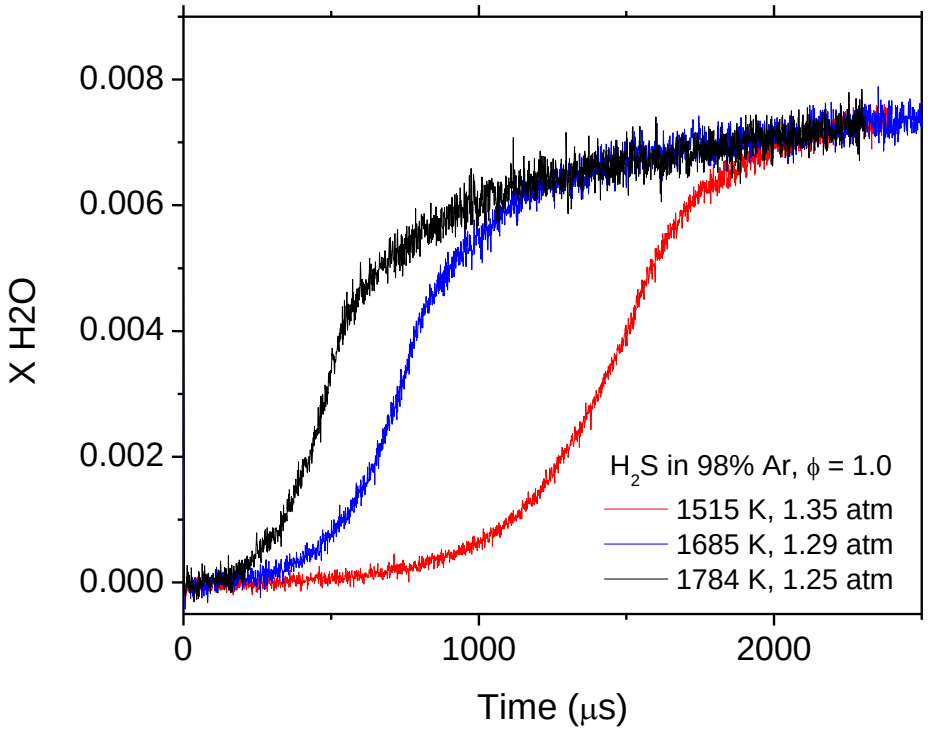

Fig. 48 Water concentration time histories at $\phi = 1$ for a range of temperatures.

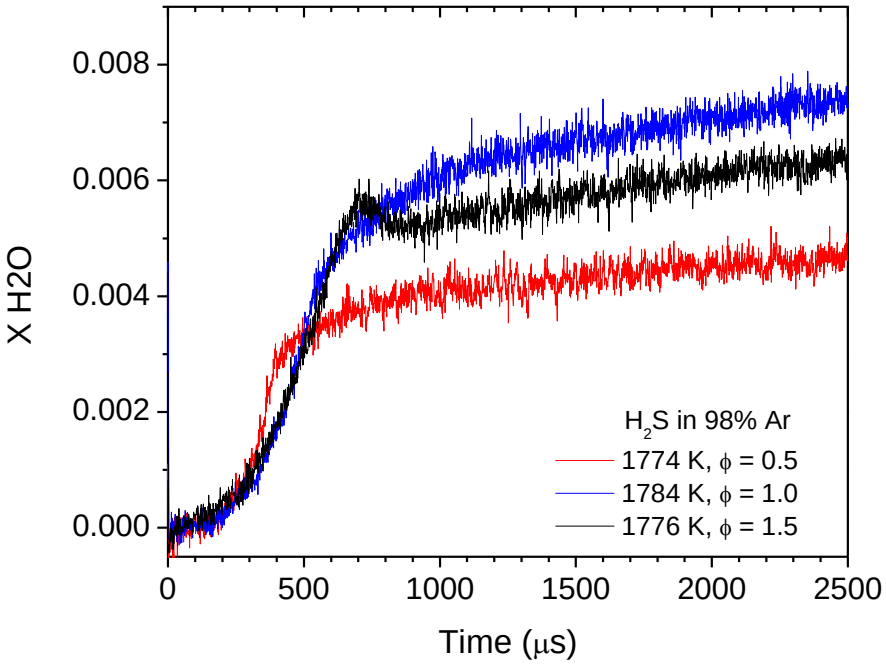

Fig. 49 Water concentration time histories at a similar temperature over a range of equivalence ratio.

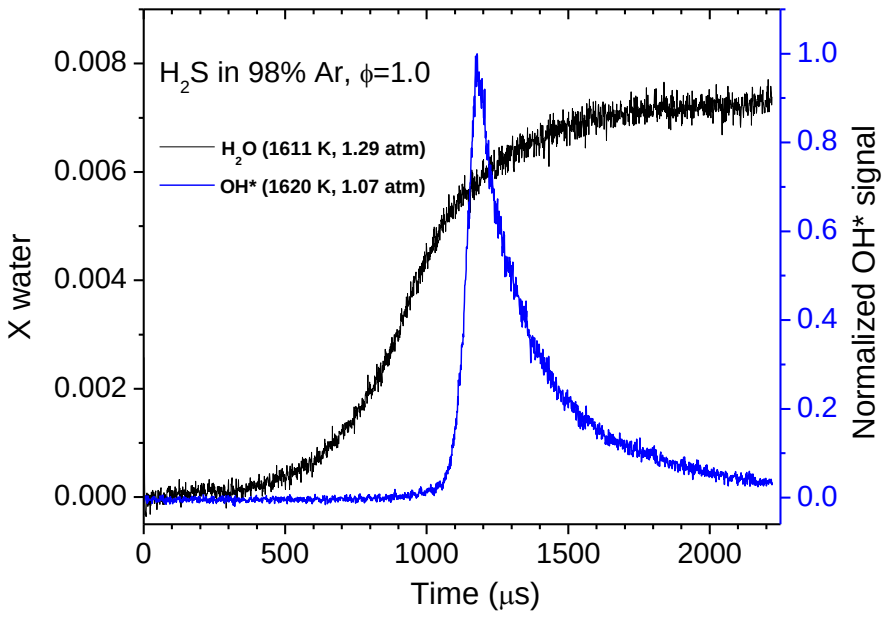

Fig. 50 H_2O and OH* traces at a similar condition, comparing ignition delay time with water measurement.

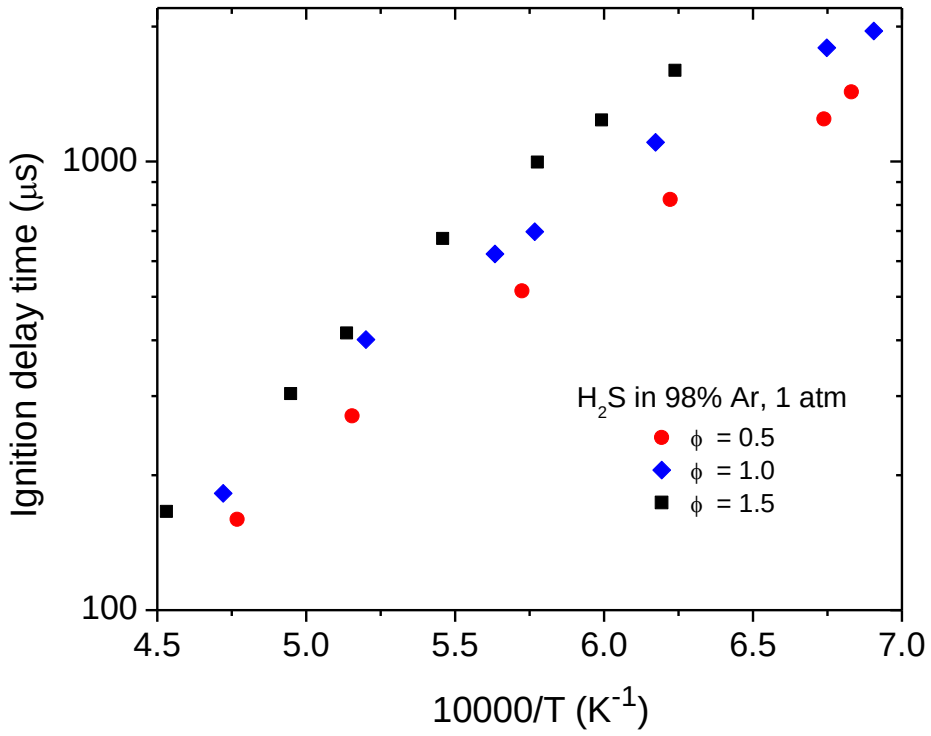

Fig. 51 Ignition delay time measurements for the H_2S oxidation tests in the shock tube.

Much work has been done with regard to modeling the hydrogen sulfide oxidation, and only a brief summary is provided in this report. A journal paper is currently being prepared with more details on the kinetics work and the shock-tube measurements. Figure 52 shows a comparison of the current kinetics model with the new data and with several other mechanisms available in the literature for H_2S oxidation. Note the wide variability. It should be mentioned that it currently is not possible to model the ignition delay times simultaneously with some other measurements available in the literature, such as from flow reactor studies. The H_2O concentration measurements help to add an additional method of comparison and calibration for the mechanism development. Figure 53 shows a typical water time history from experiment compared to various versions of the kinetics mechanism.

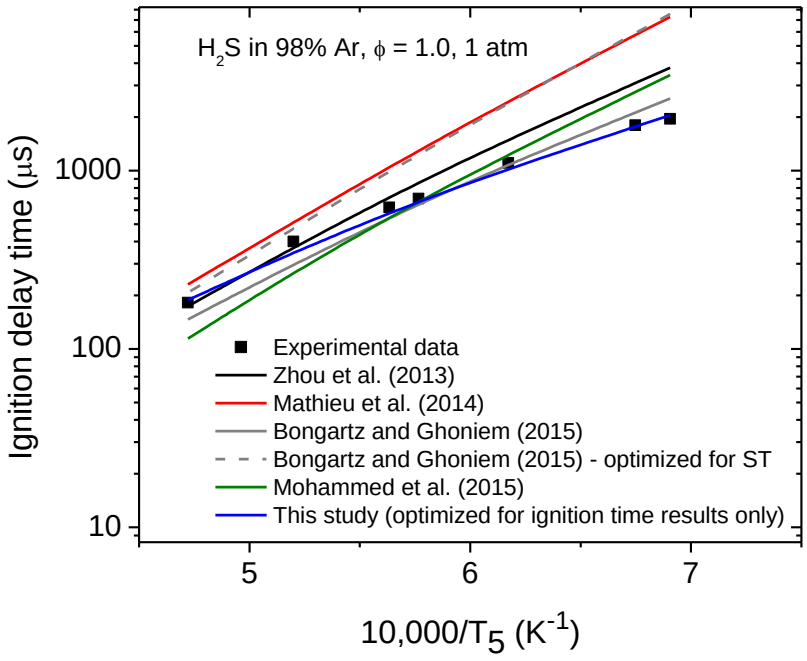

Fig. 52 Ignition delay time predictions from current and other models, in comparison with the experimental data for the stoichiometric case.

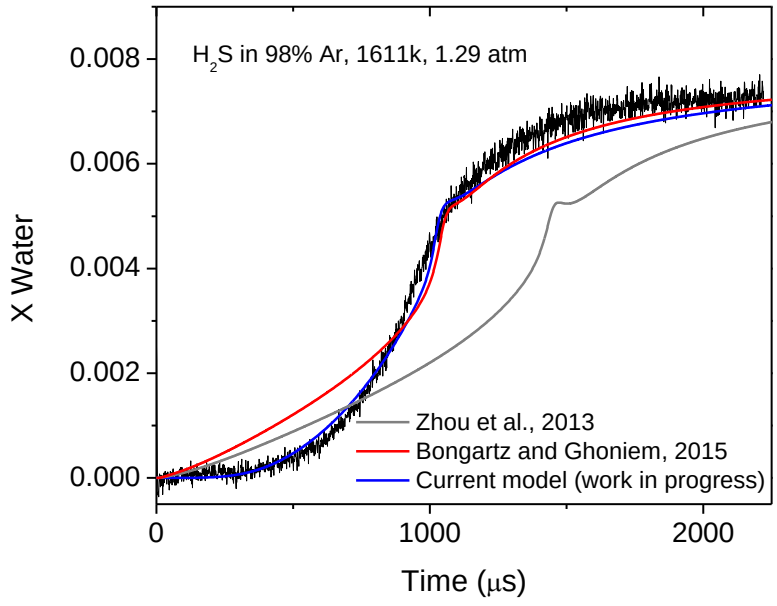

Fig. 53 Water time history (1611 K, 1.29 atm, ϕ = 1) compared to various models.

TURBULENT FLAME SPEED FLOW CHARACTERIZATION

Prior to this work, a laminar flame bomb apparatus was repurposed as a turbulent flame speed vessel with the addition of four fans. The turbulence was characterized with PIV. At that time, homogenous and isotropic flow field and negligible mean flow were found at the plane of measurement, but the study was limited to a small area and one fan speed. The turbulence characterization was revisited during the present project effort with a newly acquired LDV system. The details are summarized below. Further details can be found in the M.S. thesis of Morones (2015).

Experiment Description

Two fan speeds were tested with 2D LDV in this work, namely 8,000 and 12,000 rpm. The motor speed was verified to be within ±200 rpm from the target speed with a photo tachometer and a stroboscopic lamp. Both speed levels used the same impeller with 20 AOA, as designed by Ravi et al. (2013). The region under study was defined as the cubic volume located at the center of the vessel, with a length size of 60 mm, here after referred to as the test region. The center of the test region, the geometric center of the vessel, and the coordinate system origin are coincident, see Fig. 54.

Four-run repetitions were performed at each location for the 8,000 rpm. In total, more than 1400 runs where performed to scan the test region at this fan speed. The test region was discretized in even spaced lattice grid of 1 cm. There were in total 343 measurement locations. In the case of 12,000-rpm experiments, fewer locations where chosen within the region of study. As a matter of fact, the measurements were limited to one plane and the grid was evenly spaced at 1.5 cm. There were also fewer repetitions per location. A minimum of two (2) and a maximum of three (3) repetitions were performed at each location. Results are presented herein following this coordinate system convention. The triad depicted in Fig. 54 indicates the positive direction of the X, Y, and Z axes. Notice that the Z axis and the cylindrical axis are collinear and the electrode rods are along the Y axis. The X axis will be referred to as the "horizontal" direction; the Y axis as the "vertical" direction; and the Z axis as the "cylindrical axis" in the rest of the text.

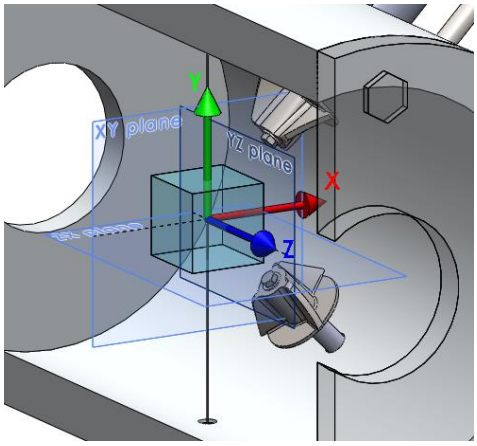

Fig. 54 Test region inside the flame bomb. Notice that the cylindrical axis and the Z axis are collinear.

Results

The results are presented in detail for a fan speed of 8,000 rpm at a cross section parallel to the X-Y plane that cuts the vessel in two mirrored cylinders. This cross section contains the origin of the coordinate system and is perpendicular to the Z axis. The relevant overall results are discussed in this section as well, along with those pertaining to a fan speed of 12,000. However, the plots of the rest of the test region and for higher speed are left for the annexes. It was decided that the plots chosen here represent well the features observed in the study.

Average Velocity

Figure 55 is an arrow or vector plot. This figure was prepared by first obtaining the average of the velocity time series for every run. Then, the measurements taken at the same location were averaged to produce one result per location. The arrow horizontal and vertical components are proportional to the local average of horizontal and vertical velocity, respectively. There is one arrow per each grid location, in other words, the test region was scanned at evenly spaced intervals of 1 cm for this fan speed. The duration of each time series is approximately 20 seconds.

An anticlockwise vortex pattern is suggested by Fig. 55. The minimum average velocity is found at the center of the cross section, which is in the vicinity of the cylindrical axis according to the coordinate system used for this work. The magnitude of the 2D average velocity increases away from the [0, 0] coordinate or in the radial direction. The vortex is visible when the average velocity data are used to create a streamline plot, Fig. 56. This pattern agrees with a previous study [Ravi et al., 2013].

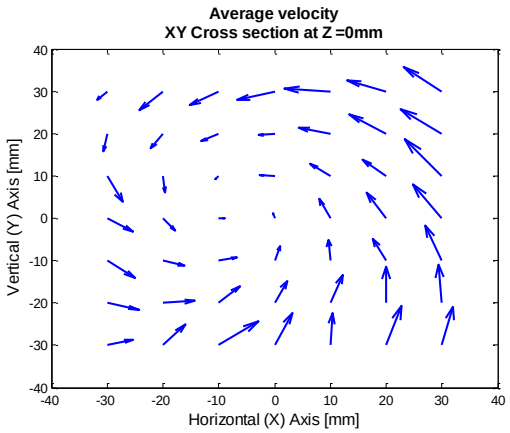

Fig. 55 Average velocity vector plot at the midplane.

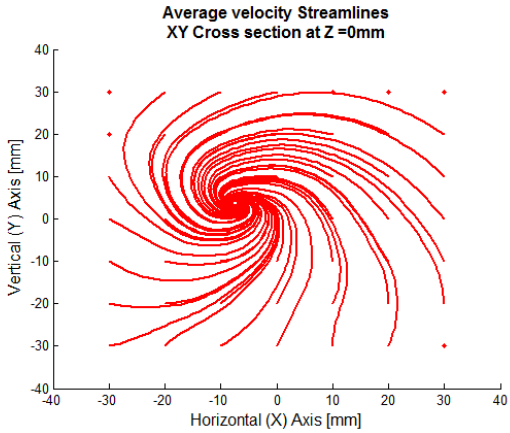

Fig. 56 A vortex is well defined and is evident.

The magnitude of the average velocities and their distribution is better described in a contour plot like Fig. 57 and Fig. 58. Roughly speaking, the plots are divided diagonally in two zones that have particles moving in opposite directions at each side of the line labeled 0. The particles converge to the diagonal division.

The highest average velocity component in the horizontal direction is found in the upper right corner of Fig. 57. The particles there are moving something between 0.6 and 0.8 m/s in direction

to the left. The fastest particles moving in the opposite direction are in the bottom left corner, clocking 0.4-0.6 m/s.

A similar inspection of the vertical velocity component shows that the highest average vertical velocity zone is the bottom right corner of Fig. 58, ranging 0.8-1.0 m/s. These particles are moving upwards, while particles on the other side of the diagonal move downwards with a maximum speed of 0.6-0.4 m/s.

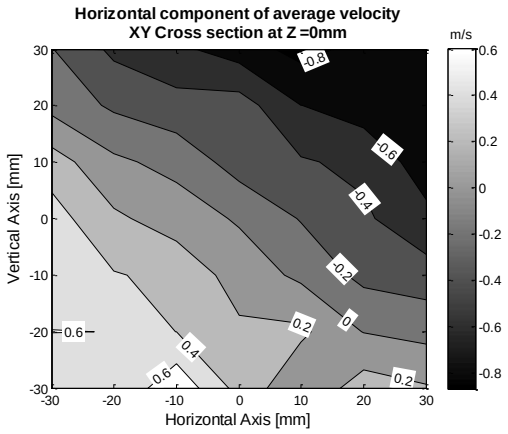

Fig. 57 Negative sign denotes particle moving to the left.

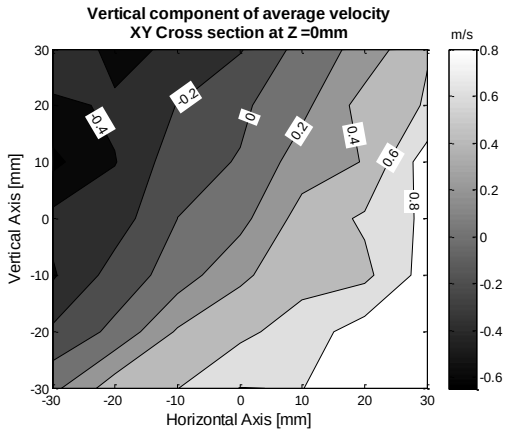

Fig. 58 Negative sign indicates particle moving downwards.

Both horizontal and vertical components can be combined in a 2D vector. Figure 59 presents the magnitude of the resultant 2D average velocity vector. The contours shown here complement the qualitative description of the flow field in Fig. 55. The ideal scenario for turbulent spherical flame speed experiments involves zero mean flow. It is clear that the average velocity results presented up to this point do not comply with this criterion, at least on the local scale. However, the mean average velocity in the horizontal and vertical components is negligible not only in the cross section discussed in the previous figures, but also in the entire test region.

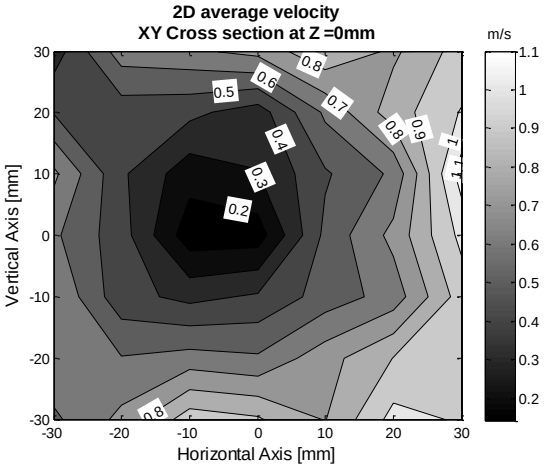

Fig. 59 2-D average velocity magnitude at the midplane.

Since the 2-D average velocity seems to be function of radial distance away from the vortex eye, a crude estimation of the rigid body rotation speed can be obtained by choosing a radius and a tangential velocity. A radius of 3 cm and a tangential velocity of 1.1 m/s was assumed to calculate a rotational speed of 36.66 rad/s, or 350 rpm.

Axial Velocity

It is possible to get insight on the velocity component that was not measured by invoking the incompressible flow assumption, the commute properties of the divergence and time averaging operators, Eq. 1. It is also necessary to assume the flow is statistically stationary. The velocity magnitudes found so far are negligible compared to the sound speed at room temperature, so the incompressibility claim should be safe. The turbulence was allowed to develop before acquiring readings, and the run time is very large compared to integral time scale, therefore the stationary flow assumption is not unreasonable. This exercise should at least reveal some of the tridimensional features of the flow, even if it is assembled from independent local measurements that are not simultaneous. The result is displayed in Fig. 60. Most of the test region was found to have a mean velocity component in the positive Z direction. The color bar shows the magnitude of the curl. The overall test region average velocity in the Z direction is 0.40 m/s.

$$\overline{\nabla \bullet \tilde{\mathbf{u}}(t;\mathbf{x})} = \nabla \bullet (\overline{\mathbf{U}(\mathbf{x})} + \cancel{\overline{\mathbf{u}(t;\mathbf{x})}}) = \nabla \bullet \mathbf{U}(\mathbf{x}) = 0 \qquad (1)$$

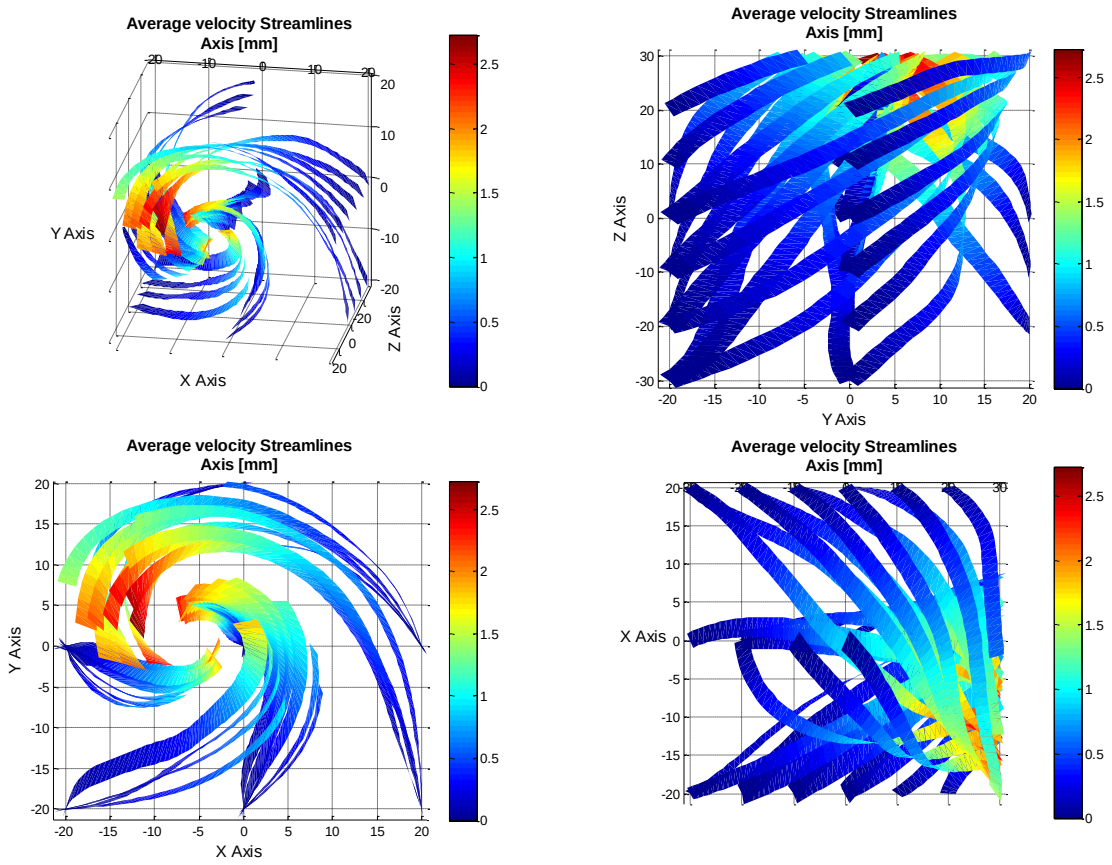

Fig. 60 Tridimensional flow. Velocity along the Z axis was calculated.

Higher Moments

The skewness and the kurtosis were computed for every run. The overall average kurtosis was 3.41 and 3.37 for the horizontal and vertical direction, respectively, and it was found very uniform in the entire test region. The kurtosis of a Gaussian distribution is 3.0, and therefore we can say the "peakness" of "flatness" of the velocity measurements resembles a Gaussian distribution.

The skewness was on average negligible for the overall test region, but a distinctive distribution was observed when the results were assembled in contour plots, Fig. 61 and Fig. 62. A zero skewness distribution has symmetric tails. A negative skewness means a heavier left tail, while the opposite is true for positive skewness. The plots are divided in two halves. One half has positive skewness while the other half has negative skewness. A relatively narrow band of near zero skewness separates these two zones. The nature of this skewness distribution is not evident to the author.

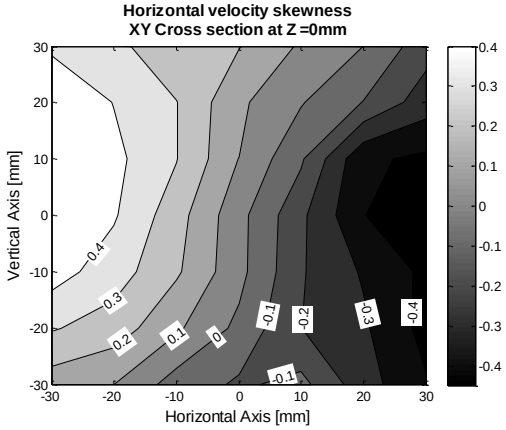

Fig. 61 Horizontal velocity skewness.

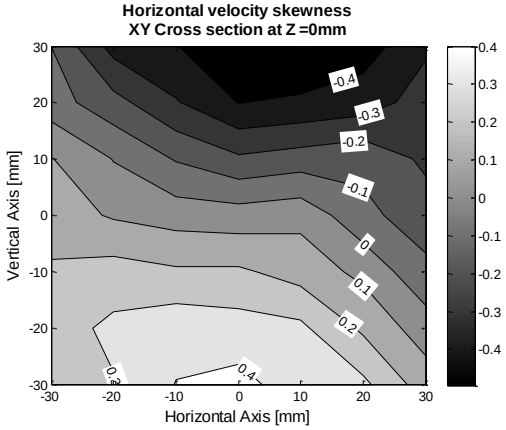

Fig. 62 Vertical velocity skewness.

Turbulence Fluctuation

The turbulence fluctuation rms in the horizontal and vertical directions is presented in Fig. 63 and Fig. 64, respectively, per Eq. (2). In both cases, the turbulence fluctuation is less intense at the center of the cross section, near the coordinates [0, 0]. The fluctuation magnitude goes from 1.5 m/s to 1.9 m/s approximately in this plot. The test region overall average rms fluctuation is 1.60 and 1.63 m/s in the horizontal and vertical directions, respectively. These results are slightly higher than what was found in an earlier study [Ravi et al., 2013] but agrees very well with the simulation of an independent group [Davani and Ronney, 2015].

$$u_{i,rms}(\mathbf{x}) = \overline{u_i^2}^{1/2}(\mathbf{x}) = \sqrt{\frac{1}{N}\sum_{n=1}^{N}(u_i(t_n;\mathbf{x}))^2} \qquad (2)$$

Where:

$u_{i,rms}(\mathbf{x})$ Turbulence fluctuation rms in direction i at positon $\mathbf{x}$

N	Total number of samples in time series
t_n	Time stamp

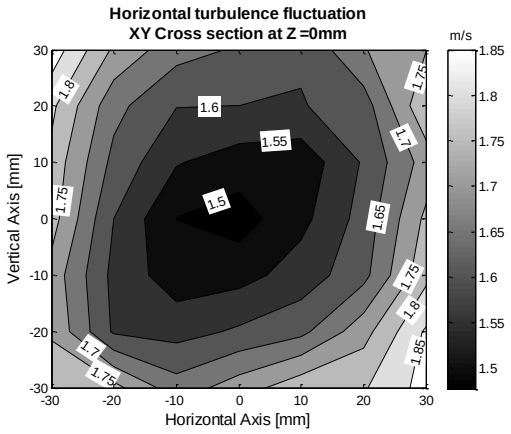

Fig. 63 Horizontal turbulence fluctuation at midplane.

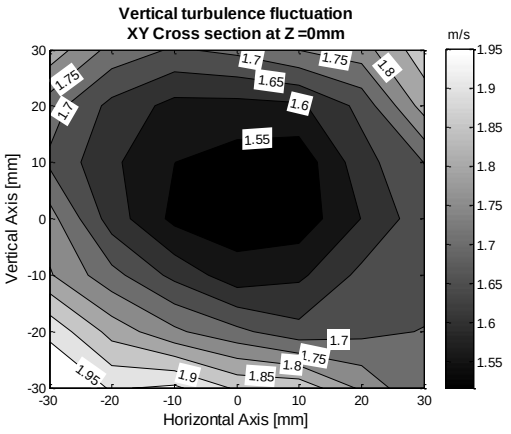

Fig. 64 Vertical turbulence fluctuation at midplane.

The turbulence fluctuation homogeneity is defined as the ratio of the local turbulence fluctuation rms to the overall spatial average, Eqs. (3) and (4). The ideal case would be to have a unity homogeneity everywhere, which implies that the local turbulence fluctuation and the overall average are numerically identical in the entire test region. However a deviation of ±10% from the overall average is acceptable. The flow is in general homogenous, with the exemption of the outer margin, where the turbulence fluctuation exceeds the test region average by more than 10%; see Fig. 65 and Fig. 66. The turbulence fluctuation in the vertical direction is slightly less homogenous. Furthermore, the rms of the residual local turbulence fluctuation and the spatial average is 0.11 and 0.13 in the horizontal and vertical directions, respectively.

$$H_i(\mathbf{x}) = \frac{u_{i,rms}(\mathbf{x})}{\overline{u_{i,rms}}} \tag{3}$$

$$\overline{u_{i,rms}} = \frac{1}{M}\sum_{1}^{M} u_{i,rms}(\mathbf{x}_m) \tag{4}$$

Where:

$H_i(\mathbf{x})$	Turbulence homogeneity in direction i at location $\mathbf{x}$
$\overline{u_{i,rms}}$	Spatial average of the turbulence fluctuation in direction i
$\mathbf{x}_m$	Coordinates of the mth sampling location
M	Total of sampling points in test region grid

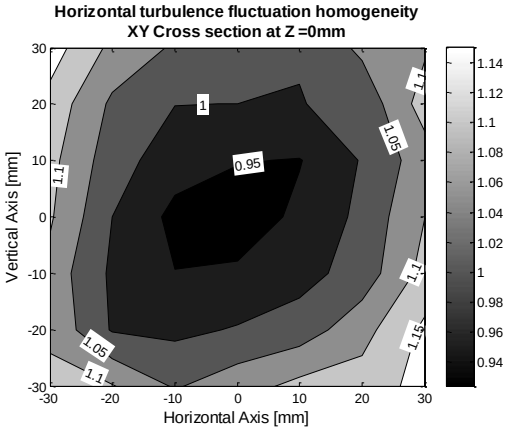

Fig. 65 Horizontal turbulence fluctuation homogeneity.

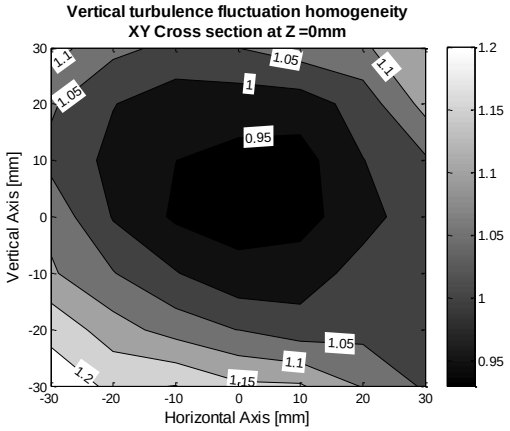

Fig. 66 Vertical turbulence fluctuation homogeneity.

For the turbulent spherical experiments demands no preferential direction in the turbulence fluctuation has strength. The isotropy tests the relative strength of the turbulence fluctuation components at each location. In this study, only the horizontal and vertical components were considered since no simultaneous measurements exist for the third component, Eq. (5). It was found that the turbulence fluctuation had no preferential direction in general, see Fig. 67. The isotropy was also observable in the u_x versus u_y scatter plots, of which Fig. 68 is an example. Notice the relatively round shape of the scatter plot, where the fluctuation in both directions is comparable. Furthermore, this scatter plot also indicates that u_x is uncorrelated with u_y, or independent. This claim is confirmed later on with the Reynolds stress results.

$$I_{xy}(\mathbf{x}) = \frac{u_{x,rms}(\mathbf{x})}{u_{y,rms}(\mathbf{x})} \tag{5}$$

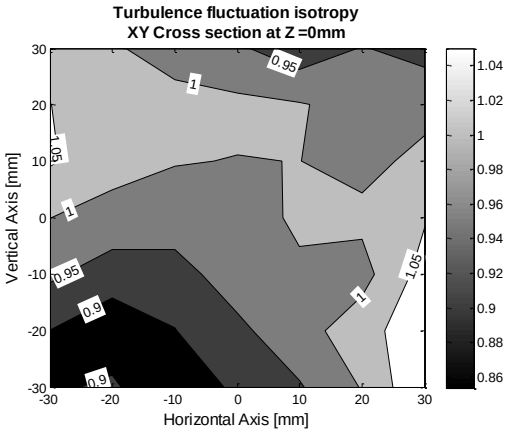

Fig. 67 Turbulence fluctuation isotropy.

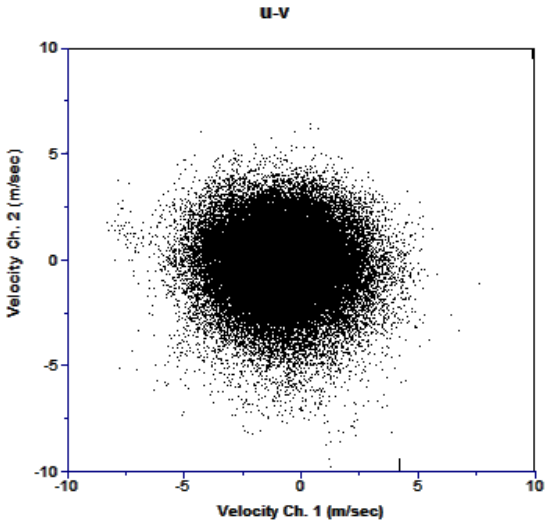

Fig. 68 u_x Vs. u_y scatter plot of run#1100.

Ratio of Average Velocity to Turbulence Fluctuation

So far, the average velocity and the turbulence fluctuation have been discussed independently. Ideally, the average velocity magnitude is desired to be zero, but if that is not possible, then at most 10% of the rms of turbulence fluctuation should be present. Figure 69 and Fig. 70 have been prepared for that comparison. It can be noticed that the average velocity magnitude meets the target in a narrow band. Most of the visible area is characterized with average velocity that is between 20 and 50% of the turbulence fluctuation rms. The figures shown here are representative of what was observed in the rest of the test region.

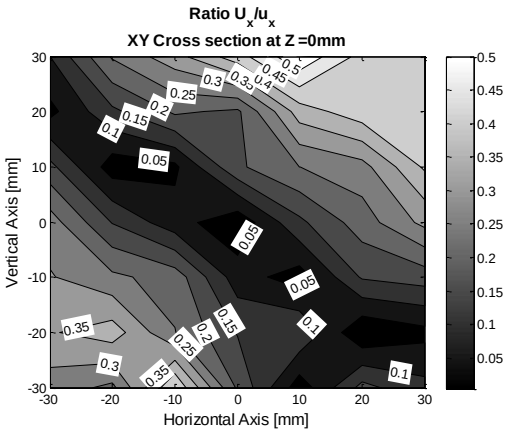

Fig. 69 Ratio of average velocity to turbulence fluctuation in the horizontal direction.

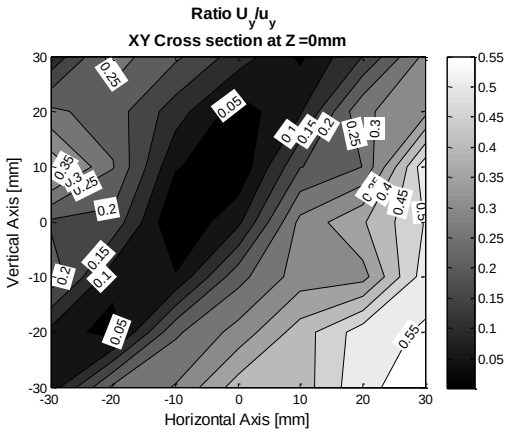

Fig. 70 Ratio of average velocity to turbulence fluctuation in the vertical direction.

Reynolds Stresses

Reynolds stresses were calculated thanks to the simultaneous measurements of the vertical and horizontal components of velocity at every location. It is evident from Fig. 71 that the normal stresses $\overline{u_x u_x}$ and $\overline{u_y u_y}$ are significantly larger than the shear stress $\overline{u_x u_y}$. As of matter of fact, this finding is positive, since for homogenous isotropic turbulence the shear Reynolds stress $\overline{u_x u_y}$ vanishes [Bradley et al., 1994; Libby, 1996].

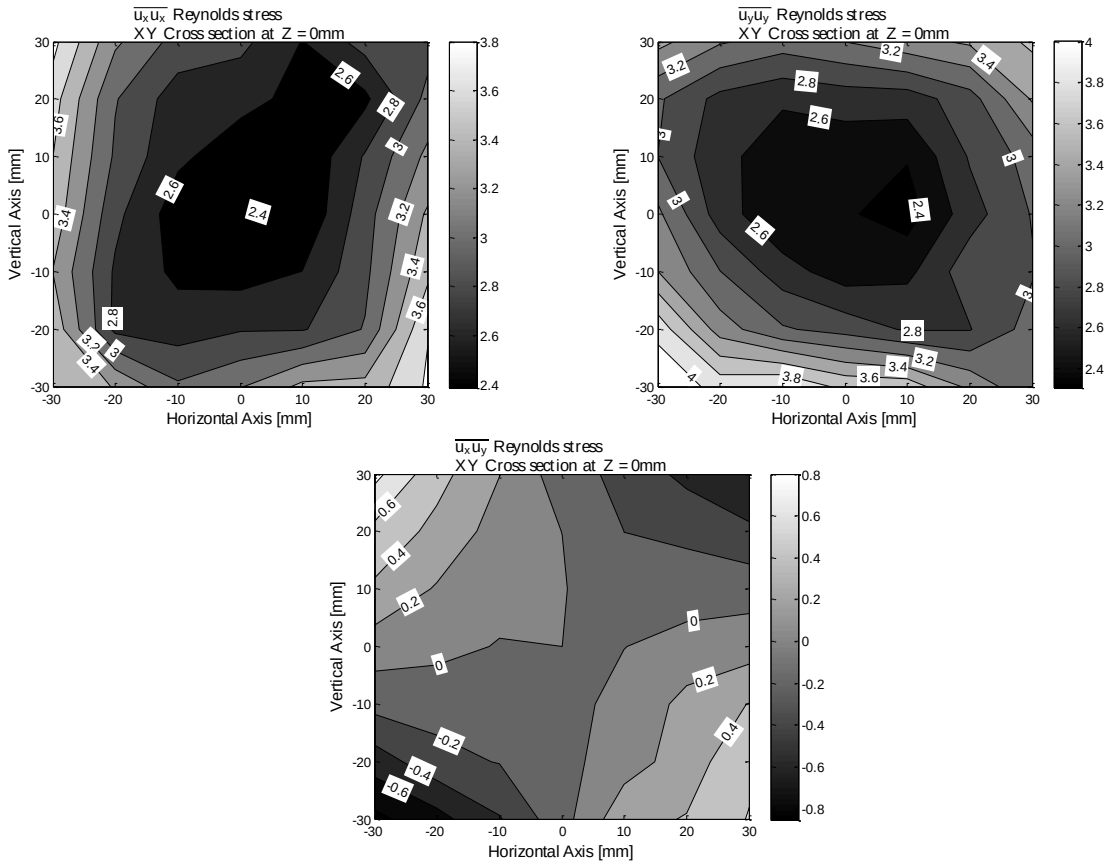

Fig. 71 Reynolds stresses at midplane.

Time Scales

Before the time scales are discussed, the long term transient or oscillation in the turbulence fluctuation should be introduced. Figure 72 presents a time series of turbulence fluctuations. The real time data are shown in blue, while the red line has the same information after being aggressively filtered. The mean of the values of this series, in green, is zero, however there is a noticeable, low-frequency oscillation. For the first five seconds, the red line stays mostly above zero and for the last 9 seconds, the red line hardly leaves the negative side.

The low-frequency wobble described above is extremely slow compared to flame speed experiments, which are in the realm of milliseconds in duration. Although, strictly speaking, this oscillation is part of the temporal coherence of the turbulence, the full length of the time series wasn't used for the calculation of the temporal correlation coefficient and thus the integral time scale. Instead, shorter segments were employed, just enough to get the correlation coefficient to vanish.

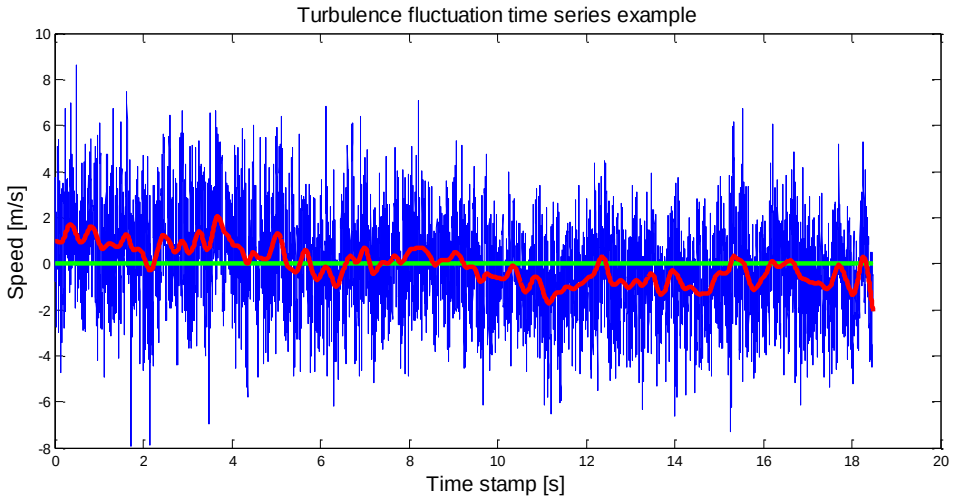

Fig. 72 Turbulence fluctuation in horizontal direction. Run # 1656 at coordinates (0,10,30) mm.

The time scale was investigated in several locations by getting the coefficient of temporal correlation of which Fig. 73 is an example. The integral time scale Λ_t is numerically equal to the area under the curve of the temporal correlation coefficient, Eq. (6). The Taylor microscale λ_t is defined as the curvature of the autocorrelation peak at $\tau = 0$, Eq. (7) [Kundu et al., 2012]. The integral time scale is on the order of 10 ms, while the Taylor microscale range from 0.4-2.0 ms.

$$\Lambda_t \equiv \int_0^\infty r(\tau)\, d\tau \tag{6}$$

$$\lambda_t^2 \equiv -2 \Big/ \left. \frac{\partial^2 r}{\partial \tau^2} \right|_{\tau=0} \tag{7}$$

The time scales at different locations are condensed in Table 5. The eddy turn over integral time scale reported Ravi et al. (2013) is at least three times greater than the integral time scales found here. It must be reminded that in their study, the macro scale was defined as the ratio of the turbulent kinetic energy and its dissipation rate, so the difference does not imply a conflict.

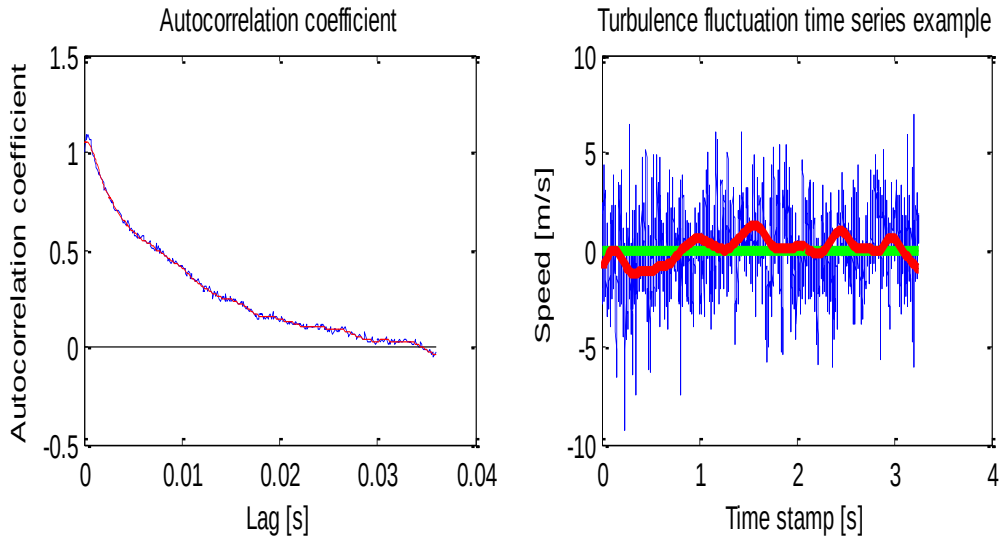

Fig. 73 Autocorrelation of run # 1592 vertical turbulent fluctuation component. Notice that after 30 ms, the turbulence becomes uncorrelated with itself, i.e. the correlation coefficient goes to zero.

Table 5 Time scales at different locations. Fans running at 8,000 rpm.

Run #	Location	Integral time scale [ms]		Taylor microscale [ms]	
		Horizontal	Vertical	Horizontal	Vertical
285	0, 0, 0	13.5	12.5	0.60	0.45
1112	30, 0, 0	10.2	8.5	0.53	0.38
943	-30, 0, 0	10.5	8.8	1.66	0.46
1015	0, 30, 0	11.3	11.6	1.36	2.09
1040	0, -30, 0	13.2	15.9	1.9	1.95
436	0, 0, 30	12.4	11.4	1.85	1.95
1592	0, 0, -30	10.1	9.9	1.43	1.43

DESIGN AND CONSTRUCTION OF A HIGH-PRESSURE TURBULENT FLAME SPEED FACILITY

The design and analysis of the new vessel was performed during this project. This section summarizes the details of the design. Detailed drawings are provided in the Appendix.

Overview

A new turbulent flame speed rig has been designed, shown in Fig. 74. The bomb will be constructed in forged alloy stainless steel. The main body of the vessel has a cylindrical shape and is closed by two end caps. A vented deflagration with double chamber approach has been opted to gain access to the expected high-pressure conditions. For high-temperature experiments, the vessel interior walls will be insulated with a liner and the reactants will be heated with a resistive element. A high intensity turbulent field will be created with a set of four fans. The following paragraphs describe some of the key features of this rig.

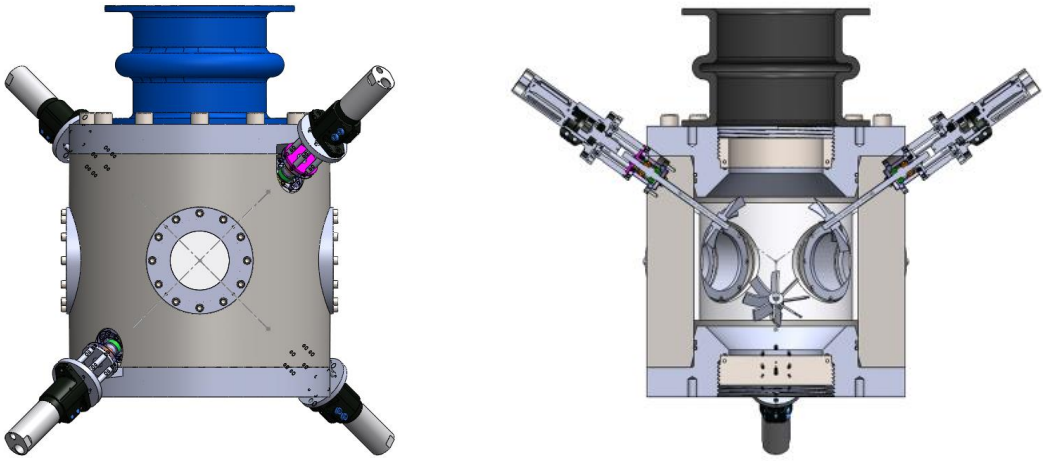

Fig. 74 Fan-stirred turbulent flame bomb schematic.

The Stirring Assembly

The stirring assembly was one of the most challenging aspects of the design of this apparatus. The maximum desired rotational speed, 10,000 rpm, was relatively high compared to the speed rating of the vast majority motors, of both pneumatic and electric. The selection of the motor is also constrained by the power demand and weight. The motor has to be strong enough to drive the fan and overcome the seal friction while being light enough to be easily handled by one person and flange-mounted directly on the bomb. The air motors are a natural choice for this kind of application; they are easily controllable in terms of speed and they are fairly powerful compared to electric motors with similar dimensions. However air motors are expensive. The final decision regarding the motor choice was to cover the operating speed range with a combination of two motors. The lower end, from 0 to 6000 rpm, will be operated with DC brushed motor, Pittman

brand, model ID33005. The DC motor main characteristics are listed in Table 6 and its physical dimensions detailed in Fig. 75.

Table 6 Technical specifications of Ametek Pittman ID33005 DC brushed motor.

Specification		
Supply Voltage	90	Vdc
Continuous Stall Torque	7.50	lb-in
Speed @ Cont. Torque	6000	rpm
Current @ Cont. Torque	8.33	A
Continuous Output Power	323	W
	0.429	hp
Maximum speed	6000	rpm
Peak Current	33.20	A
Peak Torque	37.50	lb-in
Weight	7.20	lbs

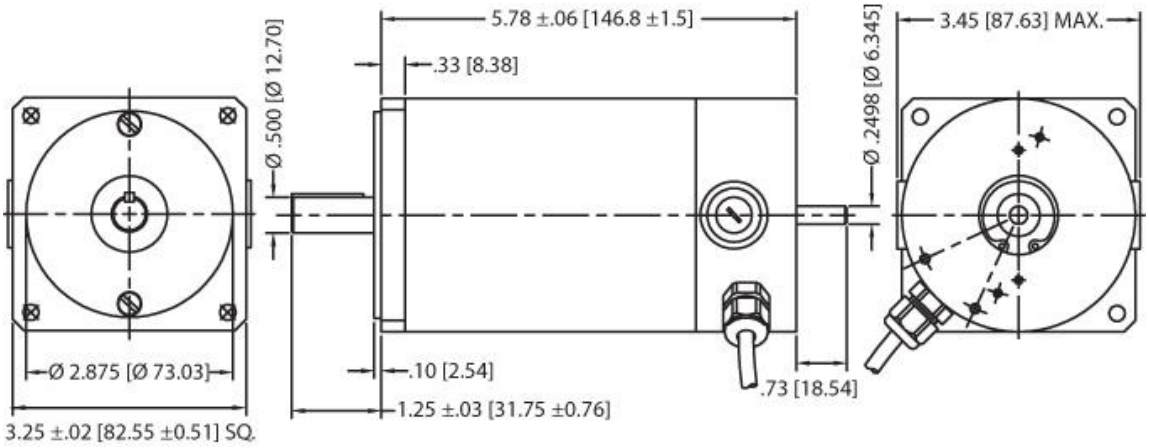

Fig. 75 DC brushed motor. Pittman ID33005.

The higher end of the speed range, 8,000 - 10,000 rpm, will be powered with router motor pack, Dewalt brand, model DW618. Some relevant figures about the motor pack are collected in Table 7. The motor pack has a built-in speed controller that allows adjusting the rotational speed from 8,000 to 24,000 rpm, albeit no very precisely. A fixed router base, Dewalt DW6184, permits a convenient coupling with the receiving flange of the stirring assembly. The motor pack and the fixed based shown in Fig. 76.

Table 7 Technical specifications of Dewalt DW618 motor.

Specification		
Supply voltage	125	Vac
Power	2.25	hp
No-load speed	8 - 24	krpm
Current	12.00	A
Collet diameter	¼, ½	in
Weight	10.1	lbs

Fig. 76 Dewalt DW618 motor pack and fixed router base DW6184.

The fan shaft was designed to have a maximum speed of 10,000 rpm. An excerpt of the shaft engineering drawing is presented in Fig. 77. The critical speed was estimated with the Rayleigh–Ritz method, expressions (8) through (11), assuming that the fan weight is applied at the very tip of the shaft. The shaft has been approximated as cantilever beam 6.5 in long for this crude analysis, considering the distance from the guide bearing to the shaft tip.

$$N_{crit} = \frac{30}{\pi}\sqrt{\frac{1}{\delta_{st}}} \tag{8}$$

$$\delta_{st} = \delta_{shaft} + \delta_{fan} \tag{9}$$

$$\delta_{shaft} = \frac{m_{shaft} L^3}{8EI} \tag{10}$$

$$\delta_{fan} = \frac{m_{fan} L^3}{3EI} \tag{11}$$

Where:

N_{crit}	11,798	rpm	shaft critical speed
δ_{st}	6.48	µm	total shaft static displacement
δ_{shaft}	2.33	µm	shaft displacement under its own weight
δ_{fan}	4.15	µm	shaft displacement due to the weight of the impeller
m_{shaft}	0.258	kg	mass of shaft (cantilever end)
m_{fan}	0.173	kg	mass of impeller (early prototype)
L	16.51	cm	cantilever length of shaft (6.5 in)

E	196	GPa	modulus of elasticity
I	3.12E-9	m^4	area moment of inertia

The numbers have been scaled for reading convenience. Proper unit concordance must be enforced before computation is executed.

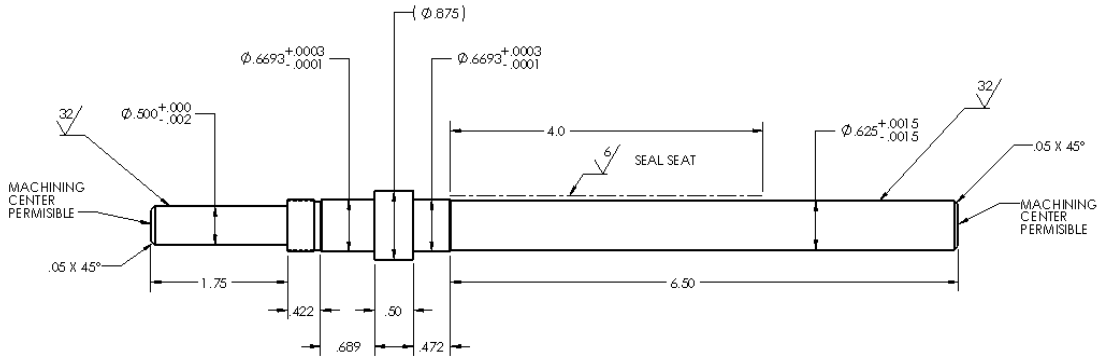

Fig. 77 Fan shaft drawing detail.

A hammer impact test was performed to a stirring assembly and the natural frequency acquired was 176 Hz with the Toro leaf blower impeller installed at the tip of the shaft. This corresponds to a critical speed of 10,560 rpm which confirms that the approximations taken for the Rayleigh–Ritz calculation were reasonable. A different configuration, with the leaf blower installed with a close clearance the bomb interior wall, produced a natural frequency of 448 Hz. The alternative fan location critical speed, 26,880 rpm, is much higher and well away from the operation range of the stirring assembly.

The shaft was opted to be machined without keyways. Balanced-keyless torque couplings, adapters, and locknuts were chosen. This decision produces a rotating assembly that is more balanced from design and also provides flexibility regarding the relative location the shaft coupling and impeller along the shaft. This is needed because the fan shaft is to be connected with at least two different motors and possibly several impellers. While the motors were chosen to have the same shaft diameter, so that a single coupling could be used for both (Fig. 78), their shaft length is not identical.

Fig. 78 Shaft bellows coupling.

Fig. 79 Keyless shaft hub connector.

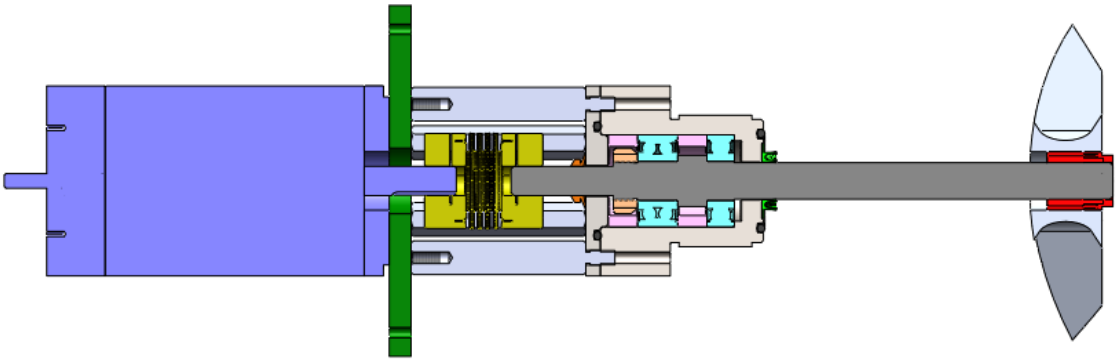

Fig. 80 Stirring assembly cross section.

The bellows coupling can be slid to facilitate assembly, colored yellow in the assembly cross section Fig. 80. With the proper machining tolerances, keyless shaft-hub connector provides a very secure interference fitting with the impeller at any position along the shaft. The keyless connector, Fig. 79, has been colored bright red in the assembly view, Fig. 80.

The primary seal around the shaft and the bomb penetration is a spring loaded PTFE lip seal, shown in bright green in Fig. 81. The lip seal has a flanged profile that is clamped between the bomb body and the bearing housing to ensure that the seal does not spin with the shaft. The lip seal material is chemically inert at elevated temperatures and pressures and is capable of running without lubrication at high surface speeds. It is rated for 3000 psi at maximum rotary surface speed of 1500 ft/min. The shaft was ground to surface finish of R_a 6 µin as recommended by the seal manufacturer. Secondary containment seals have been placed in tandem. A pair of o-rings closes the static path, while a v-ring, orange in Fig. 81, keeps contaminants out of the bearing cavity and weakly assists vacuum seal.

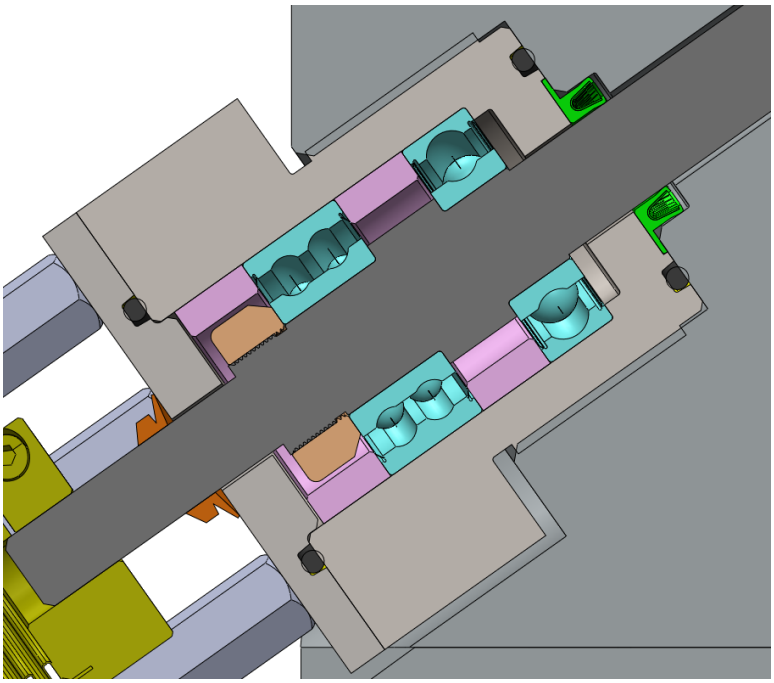

Fig. 81 Vessel and stirring assembly detail cross section.

A cage is created with 6 standoff bolts that serve multiple purposes as they secure the bearing housing lid, enclose the shaft coupling and provide a mounting structure for the motor receiving flange. The concentric design makes robust assembly because the maximum possible misalignment of the shafts is limited by the clearance and machining tolerances. Nevertheless, the metal bellows coupling absorbs and accommodates any leftover misalignment.

Windows

Two sets of orthogonal windows is a key feature of this apparatus. Orthogonal lines-of-sight enable optical techniques that potentially resolve the 3D structure of the flame in tomography or even stereoscopy, as opposed to the 2D projection of schlieren imaging. For example, the instantaneous flow field at a given cross section can be rendered using PIV or the concentration of a specific species can be mapped across the flame at any time applying planar laser induced fluorescence. Two windows are visible in Fig. 82.

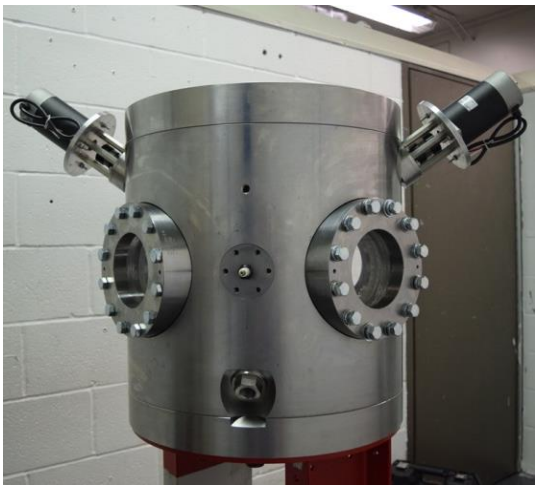

Fig. 82 Turbulent flame bomb during assembly. Plumbing and wiring work is missing in this picture.

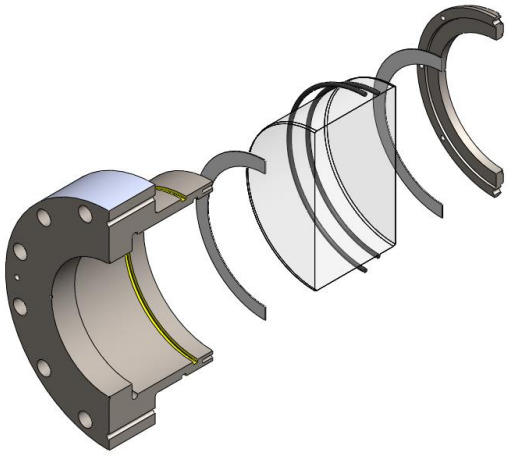

Fig. 83 Exploded cutaway view of the window subassembly.

The window substrate is padded with 1/32 thick PTFE gaskets and is gently clamped inside the cell. The clamp does not need very strong because it function is to retain the substrate in place in vacuum. A couple of circumferential o-rings shut the gas path. The o-rings glands are highlighted in yellow in Fig. 83. This arrangement makes the viewport airtight and keeps the window in low stress state.

The quartz window substrate was designed for a pressure of 3000 psi using the following expression (Harris, 1999):

$$t_w = 0.5\bar{}_a \sqrt{k_w f_s \frac{\Delta P}{\sigma_y}} \tag{12}$$

Where,

t_w	3.50	in	window thickness
$\varnothing_a$	5.00	in	aperture diameter
k_w	0.75	dim	support condition (clamped = 0.75, unclamped = 1.25)
f_s	7.58	dim	safety factor
ΔP	3000	psi	pressure differential
σ_y	8700	psi	fracture strength

A 7.6 safety factor was chosen exacting a minimum thickness of 3.5 in. according to Equation (12) Simulations show an overall low level stress with a maximum tension stress of 2.3 ksi on the center of the exterior face when an internal pressure of 3000 psi is applied; see Fig. 84 and Fig. 85.

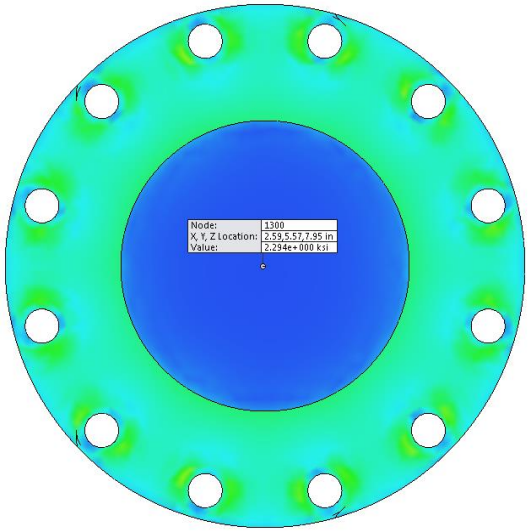

Fig. 84 Contour plot of von Mises stress of window assembly, front view.

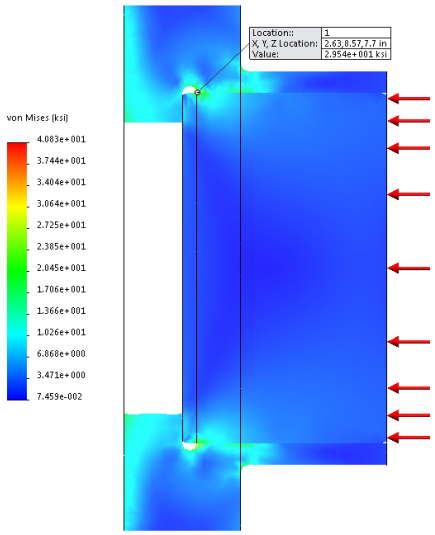

Fig. 85 Von Mises stress of window assembly, cutaway view.

Pressure Vessel

The vessel is intended to perform spherical flame experiments at 10 atm prior to ignition. An instantaneous peak pressure of roughly 10 times the initial pressure is expected typically in closed volume combustion. Therefore, the design maximum pressure is chosen to be 100 atm (1,469.6 psi).

The material chosen for this apparatus is forged martensitic stainless steel. The ASTM grade specification in its hardened condition is A182 F 6A Class 4. The material was shaped into seamless rings. The construction of the pressure vessel out of forged cylinders eliminates welding procedures. See Tables 8 and 9 (ASTM, 2016).

Table 8 Class 4 heat treating requirements for stainless steel ASTM grade F 6A.

Heat Treat Type	Austenitizing/Solutioning Temperature, min, °F [°C]	Cooling Media	Quenching Cool Below °F [°C]	Minimum Tempering Temperature °F [°C]
Anneal	Not specified	Furnace cool	N/A	N/A
Normalize and temper	Not specified	Air cool	400 [205]	1000 [540]

Table 9 Tensile and hardness requirements for ASTM A182 F 6A class 4.

Tensile Strength, min, ksi [MPa]	Yield Strength†, min, ksi [MPa]	Elongation in 2 in. [50 mm] or 4ø, min, %	Reduction of Area, min, %	Brinell Hardness Number, HBW
130 [895]	110 [760]	12	35	263–321

† Determined by the 0.2 % offset method.

According to the ASME pressure vessel code UG-27 (ASME, 2015), the formulas for the circumferential and longitudinal stress in cylindrical shells subject to internal pressure are given in equations (13) and (14) respectively.

$$t = \frac{PR}{SE - 0.6P} \tag{13}$$

$$t = \frac{PR}{2SE + 0.4P} \tag{14}$$

Where

E	1.00	dim	joint efficiency. Seamless-forgings have no joints, therefore efficiency is 1.0.
P	1500	psi	internal design pressure.
R	7.0	in	inside radius of the shell course under consideration
S	55	ksi	maximum allowable stress value. Chosen as ½ of yield strength.
t		in	minimum required thickness of shell

The minimum cylinder thickness found for circumferential stress and longitudinal stress is 0.3947 in and 0.19 in. The vessel was built with a wall thickness of 3.5 in, which yields a safety factor of 8.9.

The minimum thickness of unstayed flat heads, cover plates and blind flanges shall conform to the requirements given the ASME Pressure Vessel Code Section VIII UG-34 (ASME, 2015). The minimum required thickness of flat unstayed circular heads, covers and blind flanges shall be calculated by the following formula:

$$t = d\sqrt{CP/SE} \tag{15}$$

Where

C	0.25	dim	a factor depending upon the method of attachment of head, shell dimensions, and other items as listed in (d) below, dimensionless. End cap factor 0.25.
d	14	in	diameter, or short span, measured as indicated in Figure UG-34
E	1.0	dim	joint efficiency. Seamless forging efficiency of the joint is 1.0
P	1500	psi	internal design pressure.

The endcap does not have constant cross section; it is thinnest at the bolt flange, 2.5 inches, and much thicker in around the retaining ring thread and vent opening. Plugging the bolt flange thickness into Equation (15), produces a safety factor of 1.63. The highest stress areas are very

localized and limited to the fillet between the bolt flange and the cylindrical projection that is inserted into the bomb body, see Fig. 86 and Fig. 87. For this reason, the fillet radius was generously sized to 0.4 in, which make it the largest fillet feature among all the bomb components.

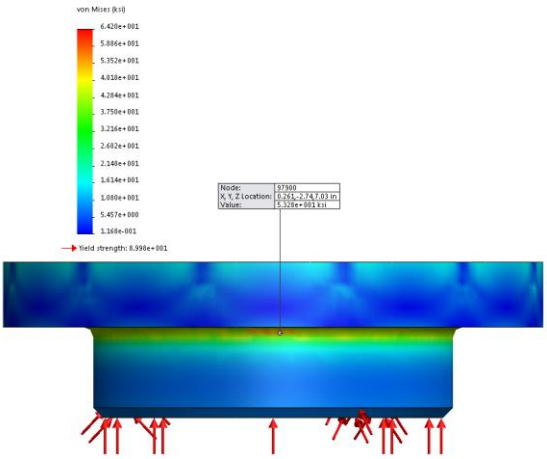

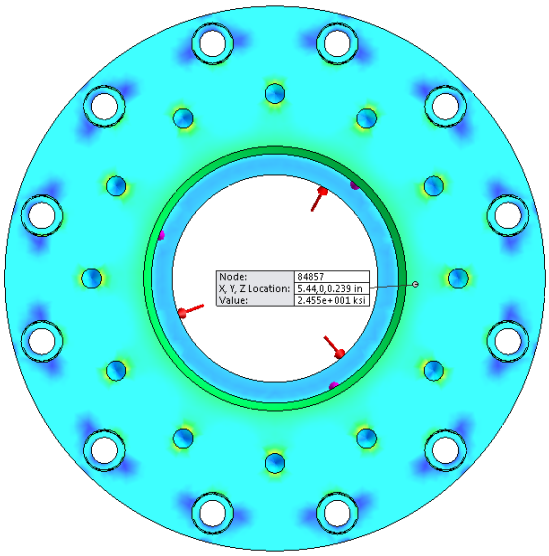

Fig. 86 Von Mises stress plot of end cap, side view.

Fig. 87 Von Mises stress plot of end cap, top view.

Fasteners

The selection and design of fasteners was done following the guidelines of the Machinery's Handbook (Oberg et al., 2012). The typical bolt strength is 170 ksi. For the minimum engagement length, the fact that the internal threads are machined into the forged stainless steel with a lower strength has to be considered. The forged rings strength is 110 ksi and the engagement length has been corrected so that the bolt would fail before the internal threads strip. The minimum engagement requirement was relaxed in the case of the bearing housing thread since it has a very generous safety factor. Table 10 summarizes the fasteners engineering.

The endcaps have an 8 in diameter breech and retaining ring, Fig. 88. The retaining ring holds in place accessories fitted at the breech, of which the simplest option is a plug blank, as presented in Fig. 89. The thread chosen for these elements is a standard 10-3 BUTT 3A buttress screw, known for being particularly strong in one direction. Table 11 details the features of the lead screw design.

Fig. 88 End cap and retaining ring.

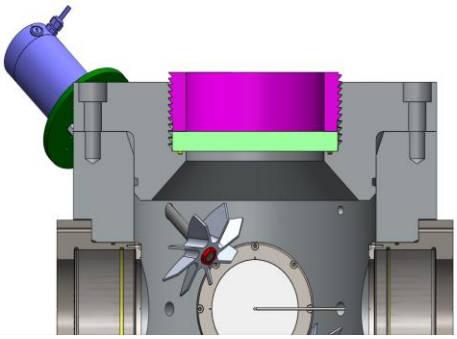

Fig. 89 Detail cutaway showing the retaining ring in magenta and a blank plug disk in light green.

Table 10 Fasteners Calculations.

Application	Thread	Number of fasteners	Q, corrected engagement length, in	Fastener strength, ksi	Pressure, psi	Total load, lb	Load per fastener, lb	Fastener, load capacity, lb	Safety factor
Window clamp	8-32 UNC 2A	8	0.137	180	15	416	52	2,522	48.5
Housing cover	1/4-20 UNC 2A	12	0.182	170	3,000	9,425	785	5,410	6.9
Side port	5/16-18 UNC 2A	6	0.238	170	3,000	4,455	742	8,913	12.0
Window cell	9/16-12 UNC 2A	12	0.442	170	3,000	107,355	8,946	30,931	3.5
Spark plug	1/2-14 NPT	1		110	3,000	1,663	1,663	51,277	30.8
Expansion joint	7/8-9 UNC 2A	12	0.705	170	3,000	235,619	19,635	78,495	4.0
End cap	1-8 UNC 2A	12	0.802	170	3,000	461,814	38,485	102,977	2.7
Bearing housing	2 1/4 -10 UNS 2A	1	1.853	110	3,000	2,356	2,356	400,311	169.9
Retaining ring	10-3 BUTT 3A	1	0.1439	63.5[†]	3,000	235,619	235,619	3,928,462	16.7

Table 11 Dimensions for 10-3 BUTT Class 3 buttress thread.

Symbol	Value	Unit	Formula	Description
D	10	in	D = 10	Major diameter (nominal)
tpi	3	threads/in	tpi = 3	Threads per inch
p	0.3333	in/thread	p = 1 / tpi	Pitch
H	0.2969	in	H = 0.89064 * p	Height of sharp V-thread
h	0.2	in	h = 0.6 * p	Basic height of thread engagement
r	0.0238	in	r = 0.07141 * p	Root radius
s	0.0275	in	s = 0.0826 * p	Root truncation for either round or flat root
S	0.0309	in	S = 0.0928 * p	Flat width of flat root form
G	0.0093	in	G = 0.0093	Allowance
h_e	0.1954	in	h_e = h - 0.5 * G	Height of thread engagement
f	0.0484	in	f = 0.14532 * p	Crest truncation
F	0.0544	in	F = 0.16316 * p	Crest width
D_n	10.0418	in	D_n = D + 0.12542 * p	Major diameter of internal thread
D_s	9.9907	in	D_s = D - G	Major diameter of external thread
E_n	9.8	in	E_n = D - h	Pitch diameter of internal thread
E_s	9.7907	in	E_s = D - h - G	Pitch diameter of external thread
h_n	0.2209	in	h_n = 0.66271 * p	Height of thread of internal thread
h_s	0.2209	in	h_s = 0.66271 * p	Height of thread of external thread
K_n	9.6	in	K_n = D - 2 * h	Minor diameter of internal thread
K_s	9.5489	in	K_s = D - 1.32542 * p - G	Minor diameter of external thread
L_{s45}	0.2438	in/thread	L_{s45} = H - f - 0.5 * G	Shear length per thread under 45 degree flank
L_s	0.2737	in/thread	L_s = L_{s45} * (1 + tan(7°))	Shear length both flanks, 7° and 45°
A_s	8.5913	in^2/thread	A_s = π * D_s * L_s	Shear area per thread

Hydrostatic Test

A hydrostatic test was performed on April 18th 2017 by FESCO, Ltd. The vessel was filled with water and then pressurized 2000 psi with a pneumatic pump, Fig. 90, Fig. 91, and Fig. 92. No leaks or pressure loss were observed, however, one quartz window fractured. Even in its broken state, the window did not disintegrated; it continued to hold pressure without releasing water. The hydrostatic test was considered successful as the worthiness of the vessel was verified. As a corrective measure, PTFE gaskets were added to the window assembly to avoid direct contact between metal and quartz on the flat faces and minimize stress concentration, as shown in Fig. 93.

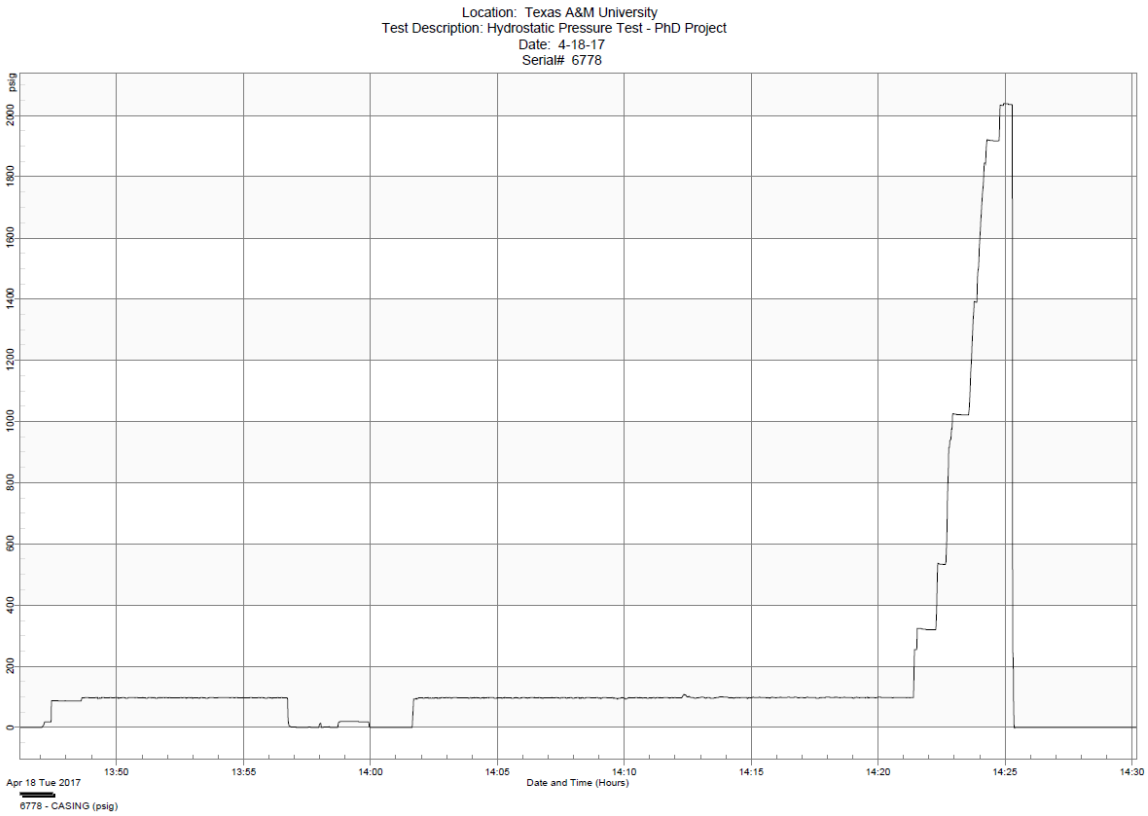

Fig. 90 Hydrostatic test pressure trace.

Fig. 91 Pneumatic pump and pressure transducer with data log.

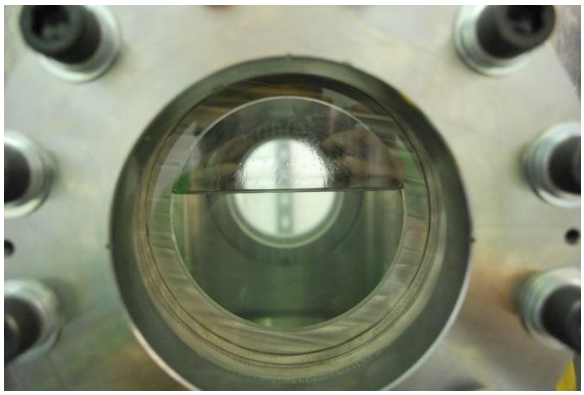

Fig. 92 Water level while preparing the vessel for hydrostatic test.

The subsequent investigation showed that the quartz substrate failed due to contact stress. A fractrographic inspection by Dr. Miladin Radovic identified the origin of fracture and propagation direction, Fig. 93. The fail started at the exterior window seat, the annular region at the bottom of the window cell socket where window substrate is supported. The fracture then branched from this point. All the quartz pieces present inclusions and defects observable with naked eye. These defects weaken the material; however it was shown that the fail started elsewhere.

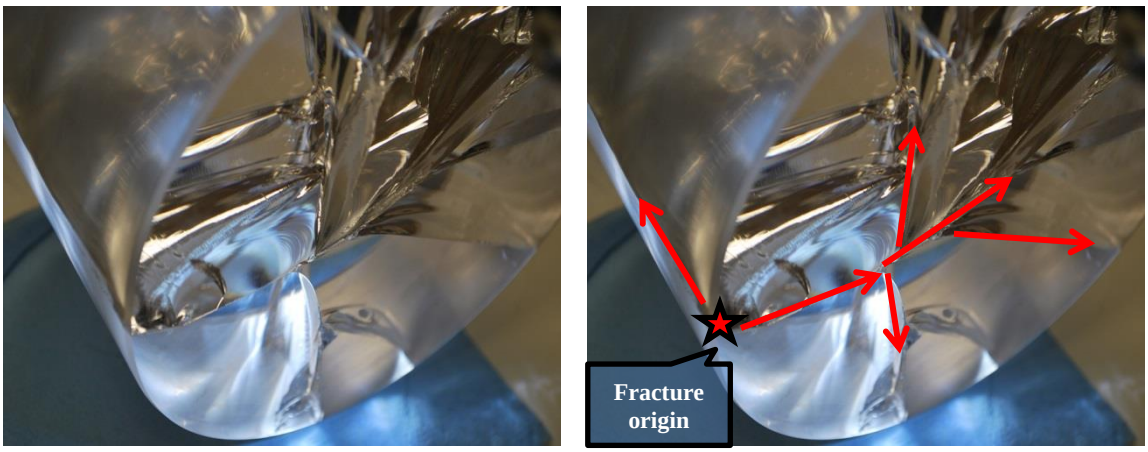

Fig. 93 Fracture propagation.

TURBULENT FLAME SPEED VESSEL CHARACTERIZATION

Background

A study showed that the first attempt of fan-stirred bomb at Texas A&M University performed poorly compared to analogous devices elsewhere [Morones, 2015; Morones et al., 2017]. Figure 94 collects the response of the turbulent field fan rotational speed. A steeper line implies that higher turbulence fluctuation is produced for a given fan speed. The first generation of fan-stirred bomb at Texas A&M University operates at a rather fast motor speed regime to produce only modest levels of turbulence fluctuation. Other research groups achieved a more effective way to stir the bomb. This fact motivated the search for improved stirrers. The impeller chosen for the first generation flame bomb is shown in Fig. 95 while its mounting configuration can be seen in Fig. 96.

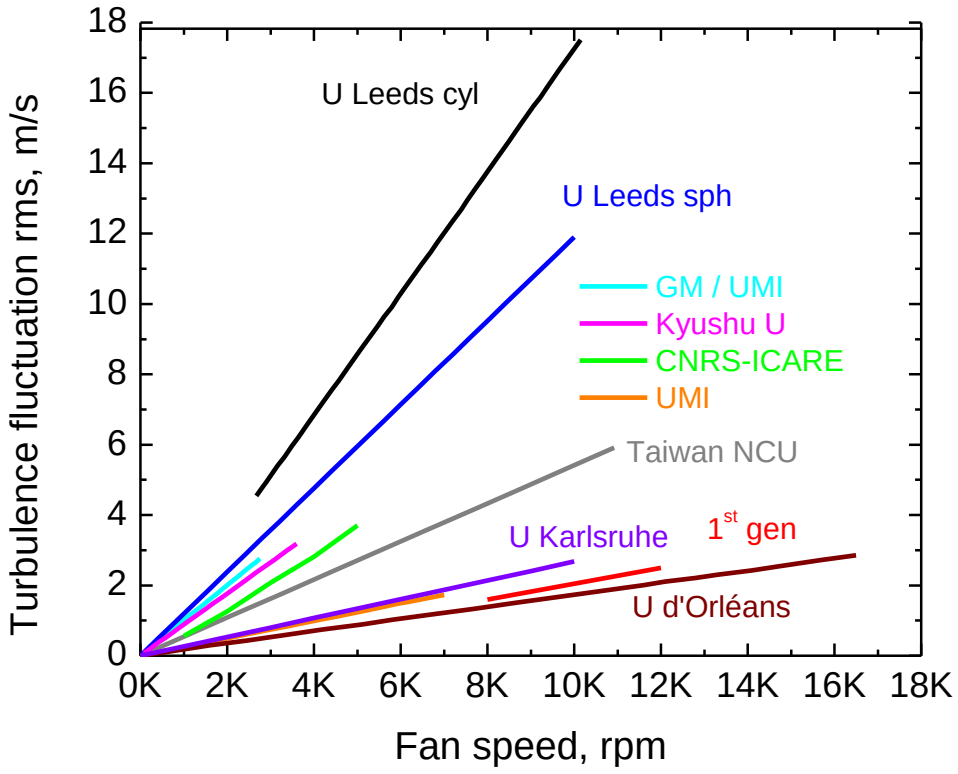

Fig. 94 Turbulence fluctuation rms and fan rotational speed of several fan-stirred bombs.

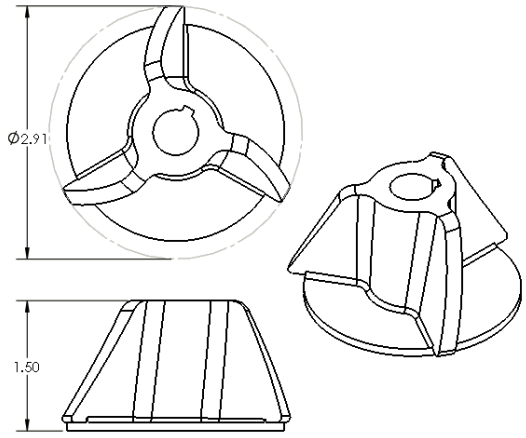

Fig. 95 Backward-curved, three-bladed impeller for the first generation of fan-stirred flame bomb at Texas A&M University. The pitch is 20°. Dimensions are in inches.

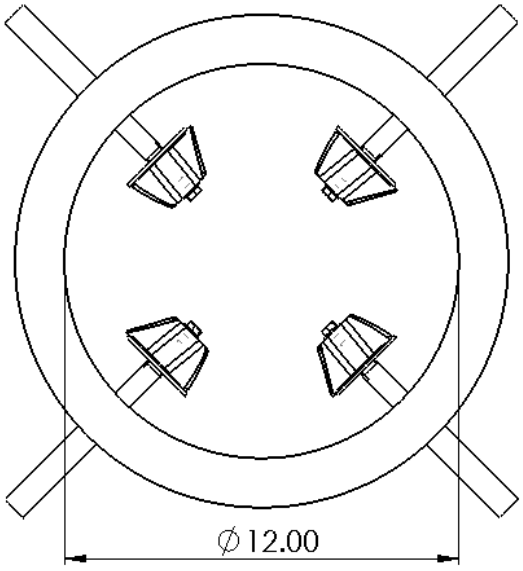

Fig. 96 Sketch of the interior of the first generation flame bomb with impellers. The internal length of the bomb cylindrical body, perpendicular to the page, is 14 in. Drawn to scale.

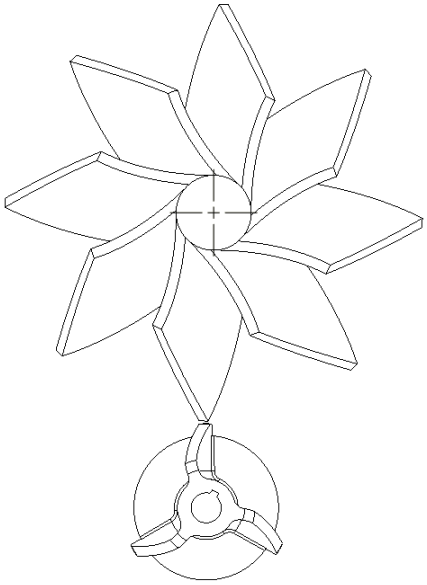

Fig. 97 Impeller of University of Leeds versus the three-bladed impeller at Texas A&M University (Abdel-Gayed, 1978).

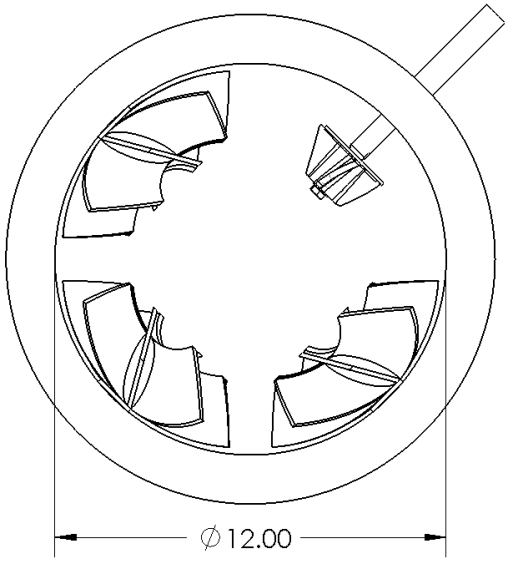

Fig. 98 Juxtaposition of impellers in a 12 in diameter vessel. Drawn to scale.

A review of the design of impellers used in other flame bombs revealed that three-bladed impeller was considerably smaller. The best performer in Fig. 94 is the cylindrical bomb built by the University of Leeds (Abdel-Gayed, 1978). Their impeller was modeled following their description

and is compared to the three-bladed impeller in Fig. 95. The British impeller is substantially larger despite the fact that both bombs have identical internal diameter, Fig. 96.

A second impeller was created for the first generation bomb to test the effect of impeller size on turbulence generation. A simple 8-bladed radial design was chosen Fig. 99. This kind of impeller has been used by other groups [Shy et al., 2000; Smallbone et al., 2006]. The axial length was kept identical to the three-bladed impeller at 1.5 in, but the diameter was increased to 4 in, or 37% larger. The total blade surface area almost folded in five.

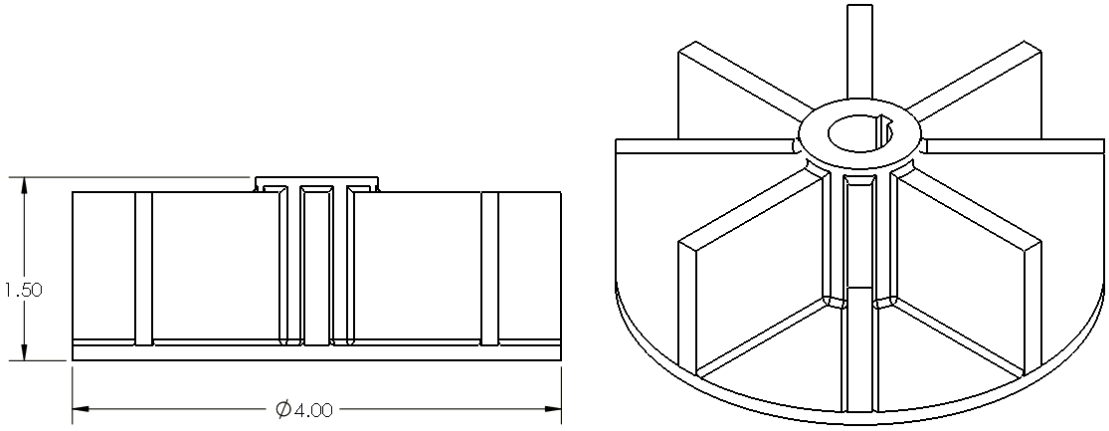

Fig. 99 Alternative design of radial impeller for first generation flame bomb at TAMU.

The turbulent field produced by the radial impeller was scanned and characterized with a 2D solid state LDV system in a similar fashion as in Morones (2015). The flow was seeded with a mist of olive oil atomized by TSI 9306 six jets particle generator. The velocimeter measures two orthogonal components simultaneously with a pair lasers, 532 and 561 nm, rated 300 mW each. The transceiver unit stands off 512.3 mm away from the probe volume created by the confluence of the laser beams. The emitting and receiving optics are combined in one device that collects the backscattered light of particles crossing the probe volume.

The measurements taken inside a 60 mm cube located at the center of the vessel. LDV results are a sequence of discrete velocity measurements that occur at random times, as particles cross the fringe pattern created by the interference of the beams. The measurements are fairly localized, as the probe volume is a tridimensional ellipsoid 3.3-3.5 mm long and with diameter 161-170 μm, so it is fair to consider them point measurements. A region of interest can be explored by moving the probe volume. If enough points are scanned, a statistically stationary snapshot of the flow field can be constructed. The LDV is a tool that needs no calibration and is particularly suitable to the study of the temporal coherence of the flow, provided that the particle cross the probe volume to a high enough frequency. However, LDV cannot capture and instantaneous plane of flow as PIV does, and generally cannot be used to investigate the length scales unless in the special case of a "frozen" flow that is being advected, as required by the Taylor's hypothesis. Frozen flow approximation is easier to justify in pipe flow with high mean flow or by traversing the LDV probe volume rapidly across the turbulent field, but these situations are not found in this flame bomb.

The nature of LDV technique allows to clock particles travelling perpendicularly to the optical axis of the probe. A 2D LDV acquisition produces a pair of velocity time series, namely $\tilde{u}(\mathbf{x},t)$ and $\tilde{w}(\mathbf{x},t)$, which correspond to the horizontal and vertical components of the tridimensional velocity $\tilde{\mathbf{a}}(\mathbf{x},t)$ (Eqn. 9). For the sake of convenience in communicating the results of the fluid mechanics characterization, instead of keeping track of all 3 components in the *X*, *Y* and *Z* directions, a characteristic vector will be constructed. The characteristic vector $\tilde{\mathbf{c}}(\mathbf{x},t)$ has the same magnitude than the actual instantaneous velocity vector $\tilde{\mathbf{a}}(\mathbf{x},t)$, but with identical components in the *X*, *Y*, and Z directions, so that $\left|\tilde{\mathbf{c}}(\mathbf{x},t)\right| = \left|\tilde{\mathbf{a}}(\mathbf{x},t)\right| = \sqrt{\tilde{u}^2 + \tilde{v}^2 + \tilde{w}^2} = \sqrt{3\tilde{c}^2}$. The notation adopted in this work will use tilde ~ to denote instantaneous, **bold** to distinguish vectors, and hat ^ for the orthogonal unity vectors along the *X*, *Y* and *Z* directions.

The $\tilde{v}(\mathbf{x},t)$ component along the line of sight of the LDV transceiver, i.e. along the *Y* axis, cannot be resolved by this laser system, see Fig. 100. The characteristic velocity will be estimated with the measurements in the *X* and *Z* directions. It must be said that this assumption cannot be confirmed in the first-generation flame bomb because it lacks adequate optical access, but it is justified in the new design discussed featured in this work. The missing component, $\tilde{v}(\mathbf{x},t)$, would be best handled by a separate LDV system with an optical axis perpendicular to the first 2D LDV system.

$$\tilde{\mathbf{a}}(\mathbf{x},t) = \tilde{u}(\mathbf{x},t)\hat{\mathbf{i}} + \tilde{v}(\mathbf{x},t)\hat{\mathbf{j}} + \tilde{w}(\mathbf{x},t)\hat{\mathbf{k}} \qquad (16)$$

A velocity time series, say $\tilde{u}(\mathbf{x},t)$, can be decomposed into a mean value $U(\mathbf{x})$ and its fluctuations $u'(\mathbf{x},t)$ **Error! Reference source not found.**. This known as Reynolds decomposition and is depicted in Fig. 101.

$$\tilde{u}(\mathbf{x},t) = U(\mathbf{x}) + u'(\mathbf{x},t) \qquad (17)$$

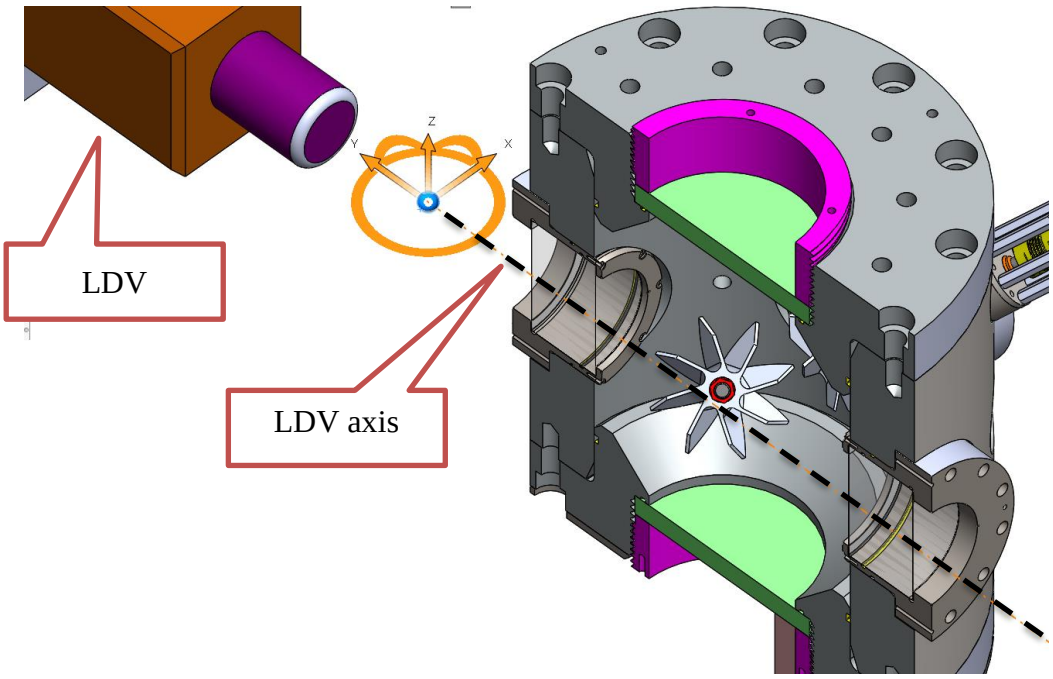

Fig. 100 Sketch of LDV transceiver and bomb. The LDV optical axis is parallel to the Y axis. The Z axis points up. The origin of the coordinate system is the bomb center.

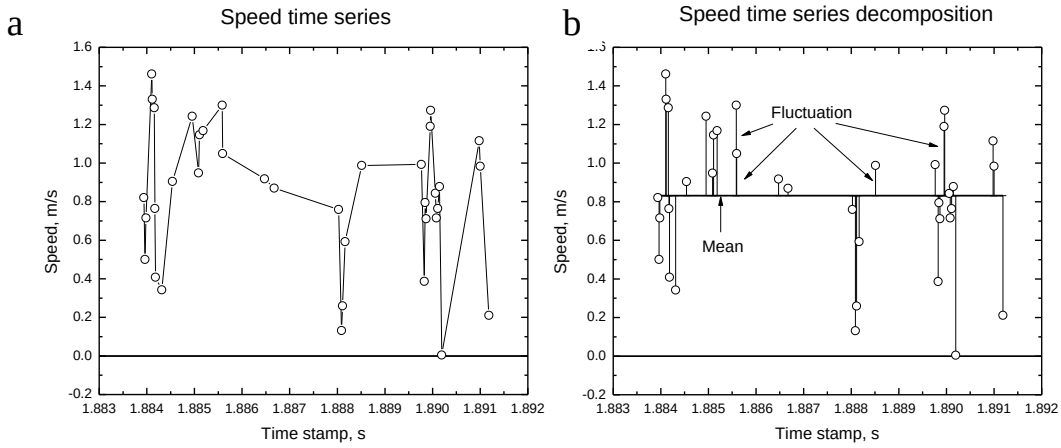

Fig. 101 Speed time series Reynolds decomposition in mean value and fluctuation.

The mean flow at a particular location, i.e. $U(\mathbf{x})$, is simply the arithmetic mean of all the velocity observations at location $\mathbf{x}$ (Eqn. 19). Locations are defined by corresponding position vector $\mathbf{x}$ (Eqn. 18), where the origin of the coordinate has arbitrarily chosen to be the center of the bomb. The characteristic mean velocity C is a scalar obtained by evaluating Eqn. 21. The reader is reminded of the underlying assumption in Eqn. 21; the component along the LDV axis, namely V, is presumed of similar magnitude as U and W. The sub-indices m and n below denote the discrete character of the measurements.

$$\mathbf{x} = x\hat{\mathbf{i}} + y\hat{\mathbf{j}} + z\hat{\mathbf{k}} \tag{18}$$

$$U(\mathbf{x}) = \overline{\tilde{u}(\mathbf{x},t)} = \frac{1}{N}\sum^{n=N} \tilde{u}(\mathbf{x},t_n) \tag{19}$$

$$U = \frac{1}{M}\sum^{m=M} U(\mathbf{x}_m) \tag{20}$$

$$C = \sqrt{\frac{U^2 + W^2}{2}} \tag{21}$$

Where

N	is the total number of velocity measurements taken at location $\mathbf{x}$.
M	is the total amount of positions scanned within the region of interest.

The flow field driven by the three bladed impeller and radial impeller were qualitatively similar. It was found that the magnitude of the local characteristic velocity $|C(\mathbf{x})| = \sqrt{[U^2(\mathbf{x}) + W^2(\mathbf{x})]/2}$ was a function of the distance to the cylindrical axis of the bomb, see Fig. 102. Parallel surfaces away from the central plane exhibited a similar pattern. The radial impeller had significantly higher mean speed in both vertical and horizontal directions. The overall spatial mean speed C was 0.2 m/s and 1.2 m/s for three-bladed and radial impellers, respectively.

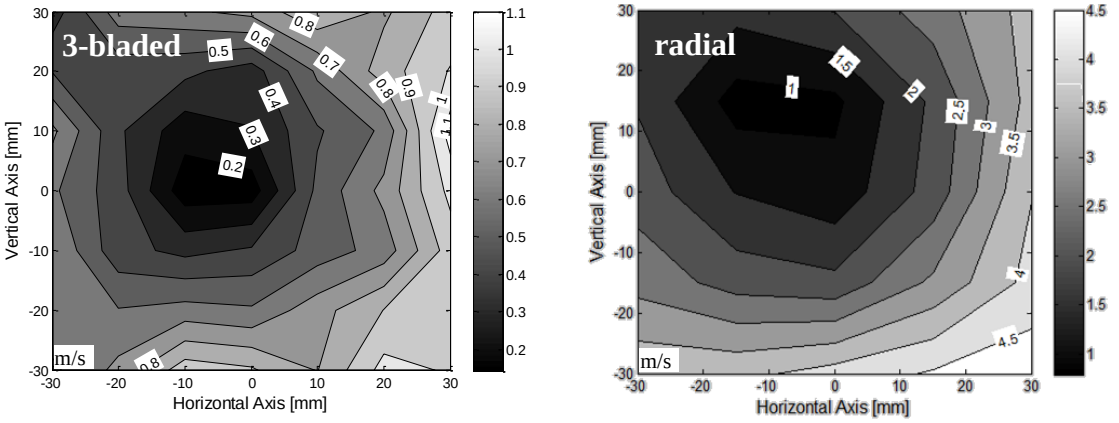

Fig. 102 Local velocity magnitude $|\mathbf{A}(\mathbf{x})|$ contour at central plane. Fan shaft speed is 8000 rpm. Left: three-bladed impeller. Right: radial impeller.

Local turbulence fluctuation root mean square, $u'_{rms}(\mathbf{x})$ and $v'_{rms}(\mathbf{x})$ is defined as Eqn. 22. Figure 103 shows concentric contour lines for both impeller designs. Only the horizontal component is presented for brevity. The radial impeller is a more vigorous stirrer. The overall volumetric average

of turbulence fluctuation c'_{rms} **Error! Reference source not found. Error! Reference source not found.**, for the radial impeller is 6.5 m/s, which is several times greater than the 1.6 m/s of the three-bladed design.

$$u'_{rms}(\mathbf{x}) = \sqrt{\overline{u'^2(\mathbf{x},t)}} = \sqrt{\frac{1}{N}\sum^{n=N} u'^2(\mathbf{x},t_n)} \tag{22}$$

$$u'_{rms} = \frac{1}{M}\sum^{m=M} u'_{rms}(\mathbf{x}_m) \tag{23}$$

$$c'_{rms} = \sqrt{\frac{u'^2_{rms} + w'^2_{rms}}{2}} \tag{24}$$

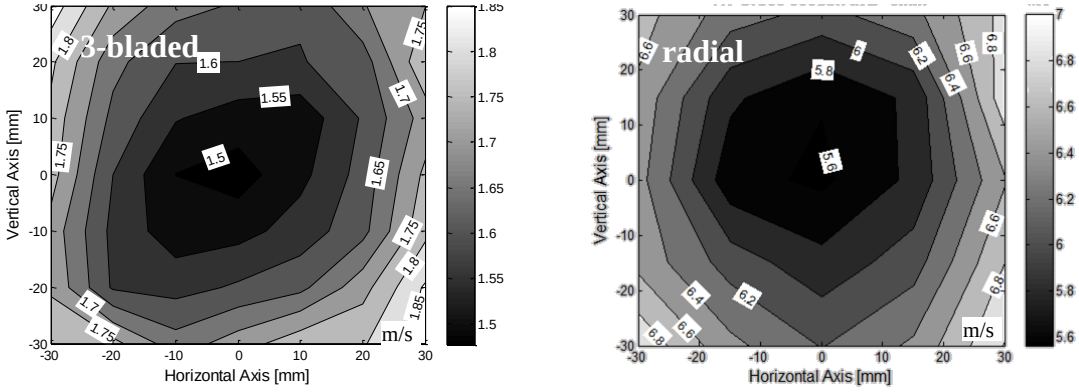

Fig. 103 Comparison of the horizontal component, $u'_{rms}(\mathbf{x})$, of the turbulence fluctuation between the 3-bladed and radial design.

The linear dependence of the turbulence fluctuation rms to the fan rotational speeds has been reported several times, recall **Fig.** . One way to express this scaling is Eqn. 25.

$$c'_{rms} \sim \omega \tag{25}$$

Where

c'_{rms}	m/s	volumetric average of turbulence fluctuation, a scalar.
ω	rad/s	fan angular velocity.

For dimensions to agree, a factor, in length units, must be inserted that allows to write Eqn. 26. Equation **Error! Reference source not found.** has the same form of the linear speed at the periphery of a spinning circle, and sticking to that figurative artifact, factor stands in as the radius.

Such factor can be found by performing a linear regression to the data in Fig. 94 to obtain the slope c'_{rms}/ω, and from now on will be called effective radius, r_{eff}. The effective radii for bombs in Fig. 94 along with other relevant figures are listed in Table 12.

$$c'_{rms} \approx r_{eff}\,\omega \tag{26}$$

Table 12 Survey of fan-stirred, spherically expanding, flame bombs shape, dimension and their fans.

Apparatus	Format dimensions, mm	Internal volume liters	Impeller diameter mm	Number of fans	Effective radius mm
U Leeds cyl. [16]	Cylinder ⌀ 305, L 305	22.3	187.5*	4	16.54†
GM/UMI [17-19]	Spheroid ⌀ 260, L 265	10.6	135	4	7.26 (9.55‡)
U Leeds sph. [20]	Sphere ⌀ 380	28.3	150§	4	11.36
UMI [21]	Spheroid ⌀ 102	0.8	48	4	2.37
Kyushu U [15]	3 intersecting cylinders ⌀ 265	35.0	200	2	8.84
U Karlsruhe [22, 23]	3 intersecting cylinders ⌀ 80, L 190	2.28	45	8	2.56
Taiwan NCU [14, 24-26]	Cruciform ⌀ 120, 225, L 600, 420	26.6	116‖	2	5.17
U d'Orléans [5]	Sphere ⌀ 200	4.2	40	6	1.64
CNR-ICARE [6]	Sphere ⌀ 563	93.4	130	8	7.48
TAMU 1st gen.[11, 27]	Cylinder ⌀ 305, L 356	25.9	73.9 (101.6#)	4	2.15 (7.76#)
This work	Spheroid ⌀ 356, L 406	33.8	124.5	4	6.60 (10.07Δ)

* The references on this bomb report 147 mm mean diameter. To be consistent with the comparison of other bombs, the outer diameter has been estimated to 187.5 mm. See sketch at appendix.

† Measured with LDV. Previous publications on the apparatus using hot wire anemometry reported significantly lower c' [Abdel-Gayed et al., 1984; Andrews et al., 1975]. The effective radius of hot wire measurements is 7.2-7.5 mm.

‡ r_{eff} = 7.26 mm for fans blowing toward the center of the vessel, and r_{eff} = 9.55 mm for reverse operation.

§ Actual diameter is not found in the reference. Outer diameter guessed is offered here based on pictures and dimensions of other features.

‖ This group has several cruciform bombs. To the author knowledge, no detailed characterization has been released for the spherically expanding flame bomb [Liu et al., 2011a; Peng, 2010], despite the fact that dimensions are not identical to previous downward propagating flame version. Wording in Liu et al. (2011b) implies that the impeller remained unchanged from that of Shy et al. (2011).

Values in parenthesis correspond to the radial impeller, Fig. 99.

Δ Values in parenthesis correspond to the plug impeller.

Explicit linear relationships between fan angular velocity and the turbulence fluctuation rms, have been reported in the literature [Shy et al., 2000; Goff, 1987; Haq, 1998; Weiß, 2008], but not as an artificial radius. The allegory of the effective radius makes the comparison among fan-stirred bombs straightforward and seems to make reasonable predictions despite the disparate nature of the fans, bomb shape and dimensions surveyed, Fig. 104. A crude linear regression indicates that the effective radius is only a fraction of fan radius, ~18%. The message is clear: larger impellers are associated with more intense turbulence fluctuation rms. The outlier in Fig. 104 has the largest impeller among the bombs discussed here, but it only has two of them installed. One more figure of merit can be invoked that takes into account the total amount of fans installed, Fig. 105. Again, a crude takeaway emerges: more installed capacity of fans is linked to better stirring. The outlier point in Fig. 105 belongs to the largest bomb in the survey which has 8 fans, ⌀ 130 mm, to agitate 93.4 liters of internal volume. The nearest vessel is 2.7 times less voluminous.

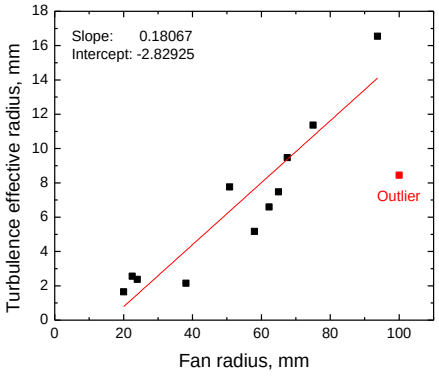

Fig. 104 Turbulence effective radius as a function of fan radius. Outliers have been excluded from linear regression.

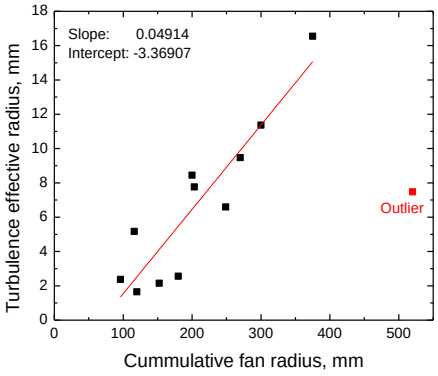

Fig. 105 Turbulence effective radius vs the product of fan radius and the total number of fans installed.

Impeller Selection

Several impeller options were evaluated for the present bomb, Fig. 106. The study of other bombs and their stirring fans showed that the impeller should be significantly larger than previously attempted. The impeller, however, should preferably be small enough to fit through the vessel window bore to facilitate assembly, i.e. $\varnothing \leq 6.747$ in. Early on, it was decided that the maximum velocity would be reduced from 24,000 rpm to 10,000 rpm. The surface speed of the shaft was desired to be low enough to allow the use of lip seals, which are relatively inexpensive and require little overhead hardware to run. One more design restriction was imposed by the motor rated power. The “low speed” DC motor chosen to spin in the range 0-6000 rpm is rated 323 W (0.429 hp), although it can handle overloads for short periods of time. The DC motor control, KB Electronics model KBMD-240D, has been upgraded with a heatsink to increase the power rating to 745.7 W (1 hp).

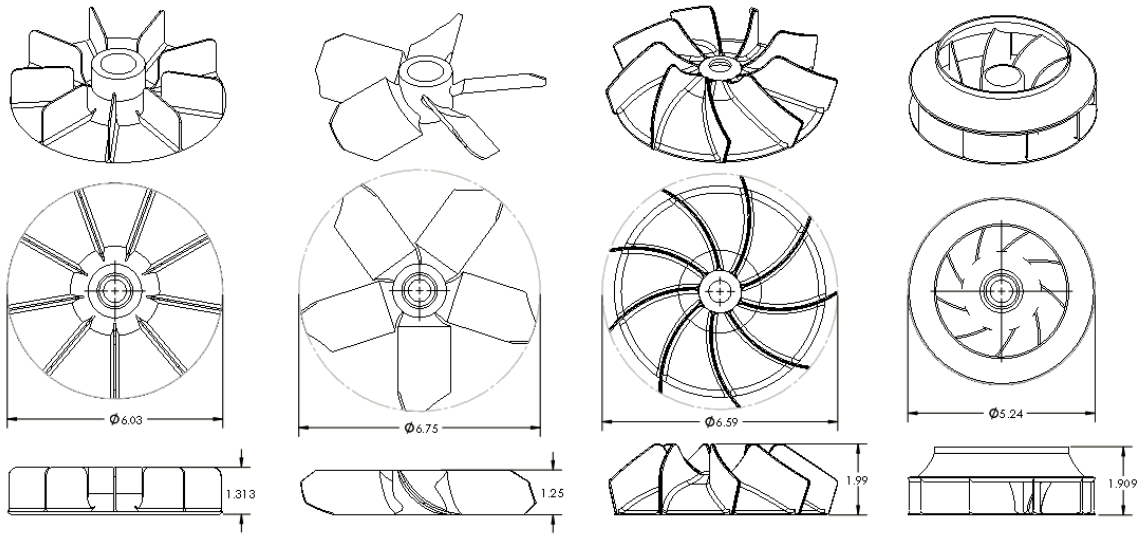

Fig. 106 Impeller prototypes tested. From left to right radial, axial, backward curved, plug design.

The impeller prototypes power consumption was evaluated. In total 5 different impeller designs were assessed: four already introduced in Fig. 106 and a commercial leaf blower / vacuum impeller, Toro 127-7092. The blower impeller is made of magnesium and has backward curved blades. Its diameter is 4.9 inches and the axial length is 1.96 inches. All but one are centrifugal fans. The radial design, or paddle wheel was the most onerous to run. It was not possible to make test beyond 4000 rpm because the power rating of the motor was exceeded. The axial and backward curved impellers also imposed a load greater than the motor capacity at 6000 rpm, but they were still manageable momentarily. The plug and blower impellers were driven by the DC motor from 0 to 6000 rpm. The flow field of these last two models was characterized with LDV measurements inside a central cubic region of 88×88×88 mm with a grid spaced at 22 mm (Fig. 107).

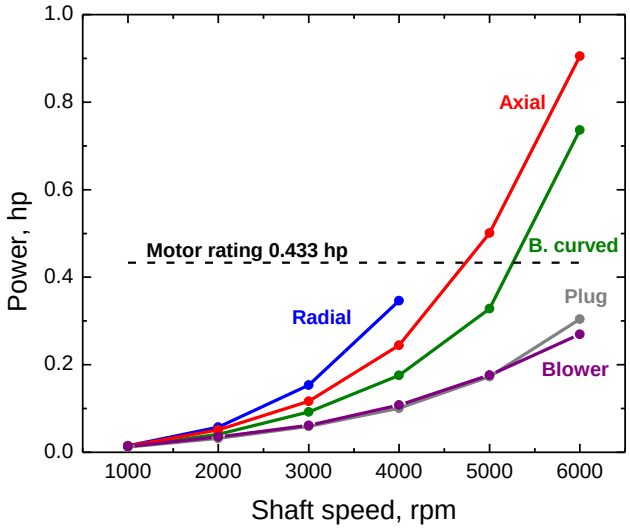

Fig. 107 Power consumption of different impeller candidates. The load does not include the lip seal demand.

LDV characterization

The plug fan flow field main features have been summarized in Table 13. The linear dependence of turbulence fluctuation is evident in u' and w', and in consequence, c'. The same cannot be said about the mean components U and W. The horizontal mean speed U increases geometrically with angular velocity, while the magnitude of W does not even behave monotonically. There is a marked anisotropy in the turbulence fluctuation as u' is only ¾ of w'. The disparity between u' and w' is confirmed by a nonzero shear stress $\overline{u'w'}$. The flow field is however fairly homogenous. In general, the distribution of the turbulence fluctuation around the mean speed resembles a normal distribution. There is almost no skewness and the flatness is close to 3.0 expected for a normal distribution. The mean velocity becomes larger proportion of the turbulence rms as fan speed increase, shows the inverse turbulence intensity C/c'.

The LDV collected velocity measurements at each location for at least 5 seconds after the flow became statistically stationary. This acquisition period is many times longer than the integral time scale. The measurements can be assembled to form a 2D quiver plot such as Fig. 108. The collection of these quiver plots shows the flow towards the suction of the impellers. This is not surprising; in average, the flow will always converge towards the suction and move away the trailing edge of the impeller, if sufficiently long averages are taken. Same pattern recognized with both impellers (i.e. plug and blower) at all tested motor speeds. The rest of the quiver plots will be left as appendix material, and the reader is referred there for further details.

Table 13 Flow field characterization of plug fan. Effective radius r_{eff} = 10.07 mm.

	2k rpm	**4k rpm**	**6k rpm**
U	-0.1784	-0.5354	-1.5134
W	-0.1167	-0.4385	-0.2293
u'	1.6925	3.4937	5.2299
w'	2.2428	4.6451	7.0302
$\overline{u'w'}$	-0.1377	-0.6079	-0.8072
$u'_{skewness}$	-0.0093	0.0153	-0.0072
$w'_{skewness}$	0.0326	0.0206	0.0045
$u'_{flatness}$	3.3017	3.3868	3.2872
$w'_{flatness}$	2.9008	3.0155	2.8892
C	0.1508	0.4893	1.0823
c'	1.9907	4.1157	6.2090
Inverse intensity C/c'	0.0757	0.1189	0.1743
Isotropy u'/w'	0.7600	0.7553	0.7491
Homogeneity std. dev.	0.0827	0.0856	0.0842

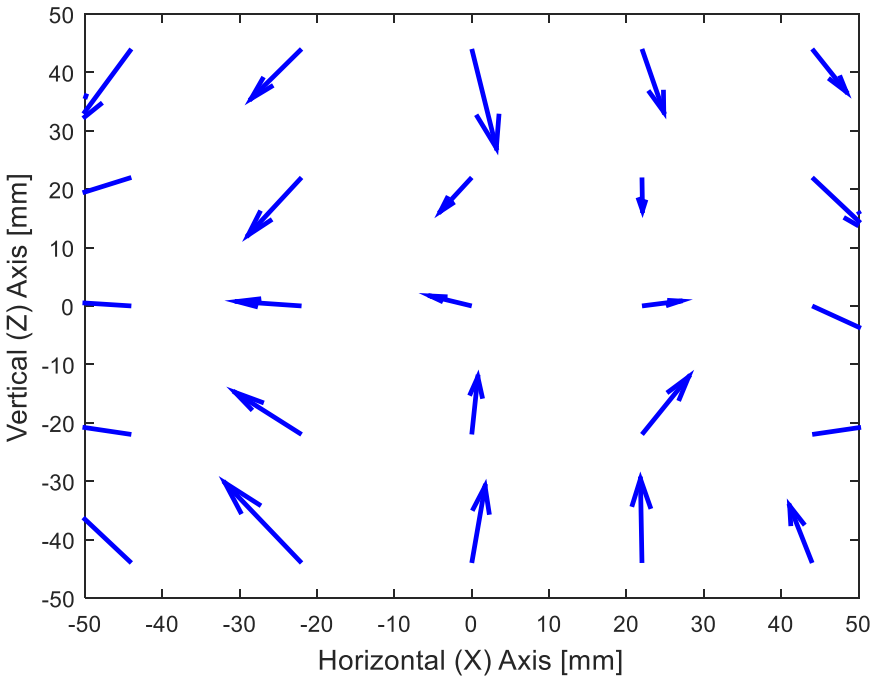

Fig. 108 Quiver plot of the mean flow produced by plug fans spinning at 6000 rpm at the central plane. The length of the arrows indicate the relative magnitude.

The plug fan and the other prototypes in Fig. 104 were 3D printed in PLA, Fig. 109. Excessive vibration was observed at 8000 rpm and for this reason it was not deemed safe to make a characterization at that speed. The leaf blower impeller was installed in two positions along the shaft. The first was at the shaft tip, away from the bomb walls and the second position was close to the wall, leaving only a small clearance between the wall and the impeller blades, as shown in Fig. 110.

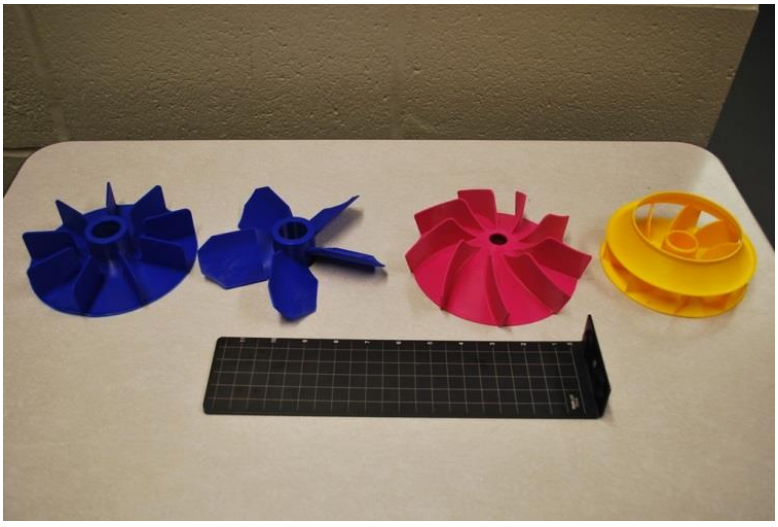

Fig. 109 3D printed impeller prototypes.

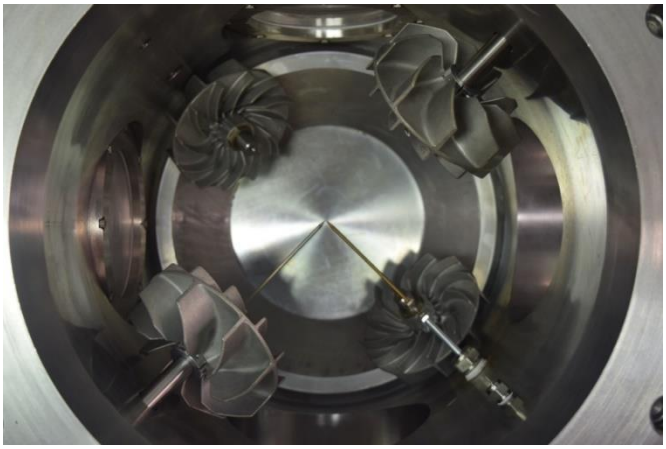

Fig. 110 Leaf blower impellers installed in bomb, top view. The top end cap was removed.

Next on the LDV characterization results is the leaf blower fan, Table 14. A substantially higher mean velocity in the horizontal direction was observed U compared with the plug design. This in turn makes the inverse turbulence intensity C/c' about 21.5% in average. The leaf blower, when installed at the shaft tip, closest to the bomb center, generates slightly less anisotropic turbulence fluctuation. Interestingly, u' is larger than w', in contrast with the plug fan case. The characteristic turbulence c' is produced by the leaf blower is markedly lower than that of the plug fan. As a matter of fact, the effective turbulence effective radius is only 6.6 mm compared to 10.07 mm, despite the fact that both impellers pull nearly the same power from the electric grid to run. The standard deviation of the flow field turbulence homogeneity is 10 %.

Table 14 Flow field characterization of blower fan. Effective radius r_{eff} = 6.6 mm.

	2k rpm	4k rpm	6k rpm	8k rpm	8k (wall) rpm
U	-0.3729	-0.7957	-1.5719	-1.6218	-2.5139
W	-0.0226	-0.0665	-0.0325	0.0572	0.0316
u'	1.5558	3.0794	4.6967	6.0741	5.4113
w'	1.2275	2.4694	3.676	4.9193	5.3317
$\overline{u'w'}$	-0.0075	-0.1081	-0.2822	-0.2149	-0.0908
$u'_{skewness}$	0.0247	0.0777	-0.0029	0.0407	0.0046
$w'_{skewness}$	0.0003	0.0035	-0.0007	0.0054	-0.0025
$u'_{flatness}$	3.0476	3.1399	3.2198	3.1441	3.1312
$w'_{flatness}$	3.1327	3.1078	3.1793	3.0707	3.0235
C	0.2642	0.5646	1.1117	1.1475	1.7777
c'	1.4026	2.7936	4.221	5.5316	5.3769
Inverse intensity C/c'	0.1883	0.2021	0.2634	0.2074	0.3306
Isotropy u'/w'	1.2719	1.2485	1.2786	1.2366	1.0157
Homogeneity std. dev.	0.0957	0.0974	0.1087	0.0971	0.1002

Fan stirred flame bombs aspire to produce a region of isotropic homogenous turbulence with negligible mean flow. The unbalance between the horizontal and vertical components of the turbulence fluctuation is therefore unfavorable. Fortunately, this kind of cylindrical bomb with tetrahedral fan configuration can adjust the relative importance of the horizontal and vertical rms values by sliding the impeller along the shaft closer or away from bomb center, Fig. 111. As the blades come closer to the bomb wall, the later act as a shroud or housing that favors the flow along the cylindrical axis. The first 4 columns in Table 14 were done with the impeller installed at the tip of the shaft. The impellers were then slid towards the wall the measurements at 8000 rpm were repeated. The flow became isotropic while still homogenous. The overall inverse intensity was negatively affected, since it increase from ~21% to 33%.

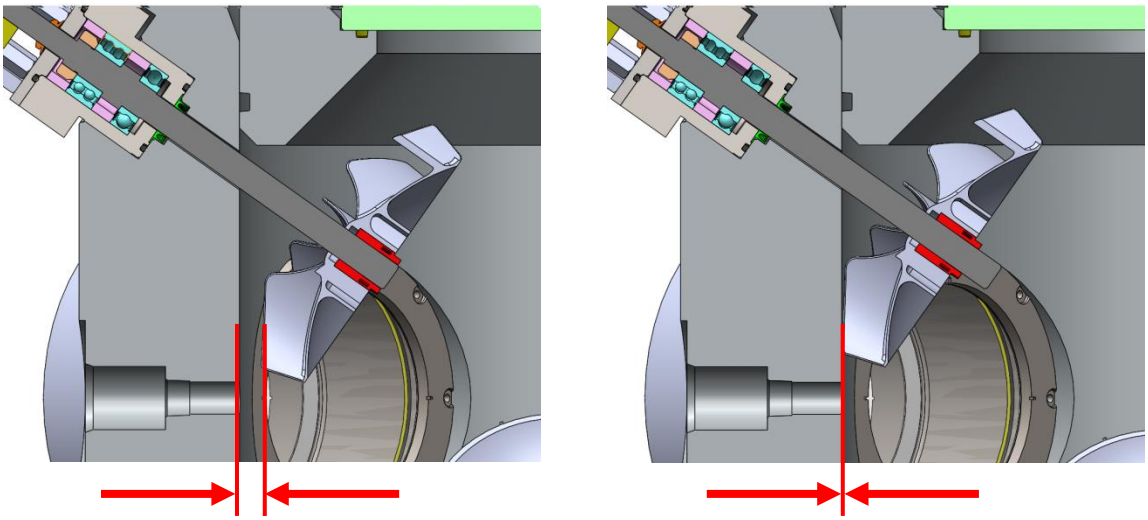

Fig. 111 Comparison of impeller installation position. On the left, the impeller is installed at the tip of the shaft, closest to the bomb center. On the right, the impeller has only a small clearance with the bomb cylindrical wall.

The temporal coherence of the flow field was studied by computing autocorrelations, Table 15. A computer program was written in Fortran and the source code has been included in the appendices. It was found that at the center of the bomb, coordinates [0, 0, 0], the integral time scale of both, $u'(\mathbf{x},t)$ and $w'(\mathbf{x},t)$, decreased monotonically with fan shaft speed regardless of the fan design. However, such dependency was not observed at the point [-44, 44, -44], especially in the case of the blower fan installed at the tip of the shaft. There, at one of the corners of the cubic region scanned with LDV, the time scales of $w'(\mathbf{x},t)$ were consistently short, while those of $u'(\mathbf{x},t)$ were longer and with more spread.

Figure 112 offers autocorrelation plots for the leaf blower fan installed with close clearance to the wall. The self-correlations have been smoothed with the Savitzky-Golay method using 32 points per window to fit a 2nd order polynomial. The integral time scale is numerically equal to the area below the curve from null delay to the first zero crossing. The rest of the self-correlation plots are left in the appendices.

Table 15 Integral time scale of selected locations. Time scales in ms. Coordinates in mm.

	$u'(\mathbf{x},t)$ [0, 0, 0]	$w'(\mathbf{x},t)$ [0, 0, 0]	$u'(\mathbf{x},t)$ [-44, 44, -44]	$w'(\mathbf{x},t)$ [-44, 44, -44]
Plug, 2000 rpm	14.29	12.60	12.42	21.04
Plug, 6000 rpm	3.85	4.40	5.01	5.46
Blower, 2000 rpm	34.51	11.20	8.39	2.94
Blower, 4000 rpm	14.46	8.68	10.12	4.44
Blower, 6000 rpm	11.46	5.88	13.78	2.40
Blower, 8000 rpm	8.85	3.13	4.70	2.27
Blower, 8000 rpm, at wall	4.64	4.29	6.39	2.75

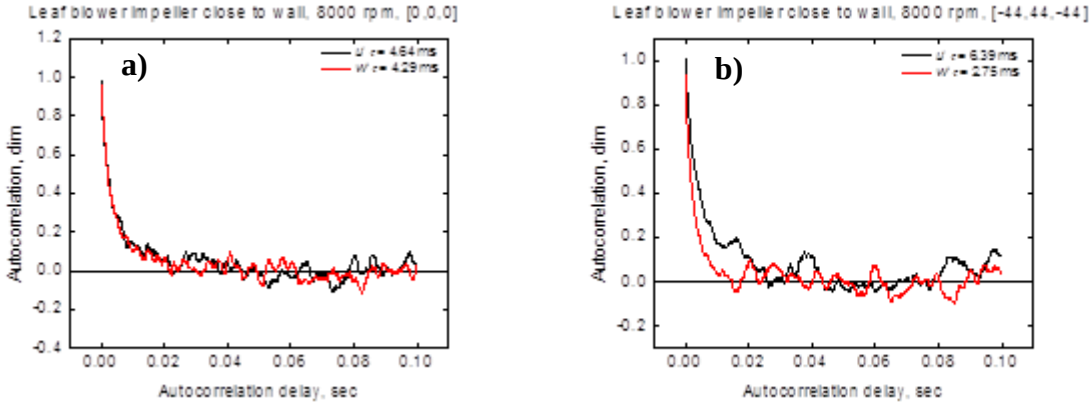

Fig. 112 Autocorrelation of turbulence fluctuation at two locations. The leaf blower fan was installed with a close clearance from the wall.

Configuration

The bomb was fitted with the leaf blower impellers mounted with close clearance to the cylindrical wall. A new schlieren set up was designed that collimates the light coming from a mercury arc lamp and refocus it on the camera with plano-convex lenses as opposed to the parabolic mirrors employed in the past. The light is steered with flat mirrors on kinematic mounts. The blast room layout was overhauled. New stands for the bombs in the room were built so that their optical axis is now at the same elevation plane. This change makes easier to share the same schlieren assembly, reducing downtime between the swaps. A view of the blast room is offered in Fig. 113.

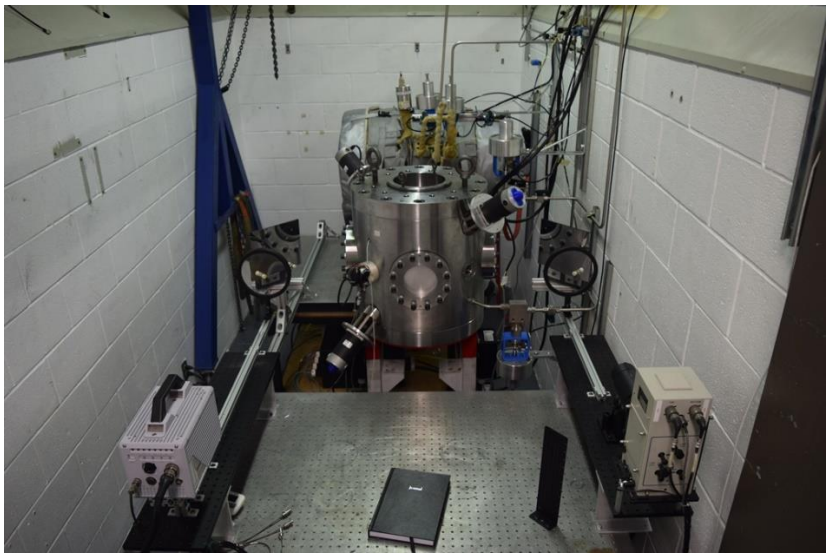

Fig. 113 Blast room layout. The new fan-stirred flame bomb is at center. An existing, heated, stainless steel, laminar flame vessel is partially visible in the back. The schlieren optical elements are shown.

Laminar Flame Speed Validation

Since this is a new device, a validation of the results produce by it is necessary. A series of experiments with hydrogen were chosen as a figure of merit. The bomb not only able to reproduce results obtained in the past by this group (Krejci et al., 2013), but also showed an excellent repeatability, Fig. 114. During the analysis, confinement effect was observable in the burned velocity vs stretch plots. This might be due to the fact that this new bomb diameter and volume is greater than former generations at Texas A&M University [de Vries, 2009; Krejci, 2012].

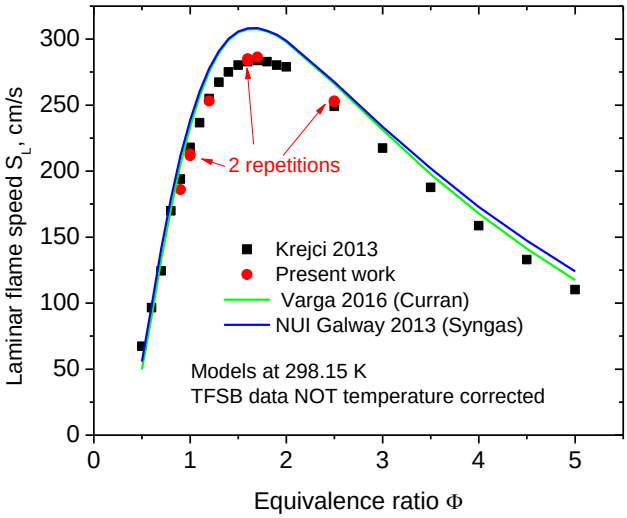

Fig. 114 Laminar flame speed of hydrogen at 1 atm and room temperature. Continuous lines are recent kinetics models for hydrogen and syngas [Kéromnès et al., 2013; Varga et al., 2016].

The maximum operating pressure is 10 atm. This figure refers to the pressure of reactants prior to ignition. The competence of the bomb under static load was judged with the hydrostatic test disclosed elsewhere in this text. A conservative rule of thumb estimates that the pegging pressure, i.e. the momentarily peak pressure, will be tenfold the initial pressure for closed volume combustion. Before commissioning the bomb for operation at 10 atm, trial experiments with aluminum window plugs where performed, Fig. 105. The trials with aluminum window plugs were successful, Fig. 106, and the window cells were again fitted with quartz substrates.

Fig. 105 The quartz substrate on the right window has been substituted by aluminum blank.

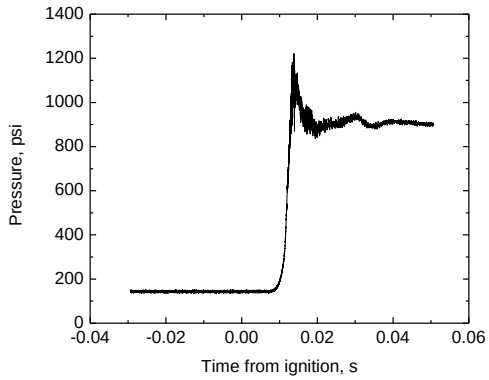

Fig. 106 Pressure trace of ST Run 43. Reactants pressure was 10 atm. Stoichiometric hydrogen in air.

It was noticed that, after high pressure experiments, the combustion products when seen through the window immediately after a run, had a distinctively yellow/greenish coloration, see Fig. 107. The yellow shade was more intense the higher the initial pressure, in other words, combustion products 10 bar experiments were decidedly mustard while the color of those at 2 bar was barely perceptible. Moreover, if the combustion gases were allow to sit in the bomb and cool down, the mustard hue fade gradually. The water that eventually condensed inside the bomb had a bright yellow color while some surfaces were stained with a dark brown/rust patina. To minimize condensation and the residue left behind, the combustion products were vented through the ventilation system as quickly as possible. Even with the extraction system working, a pungent biting smell was perceived for a few seconds following the exhaust release.

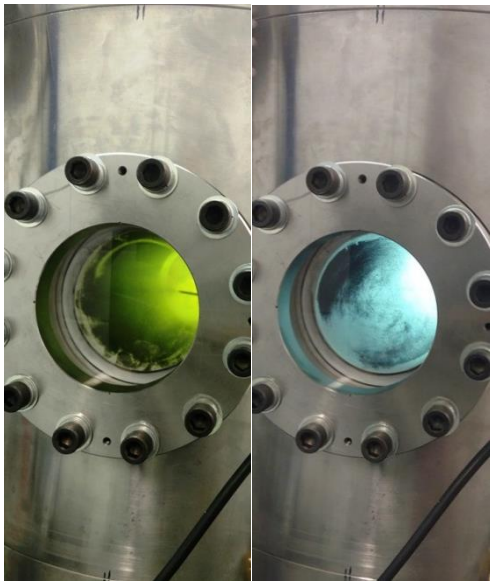

Fig. 107 Combustion products after a 10 bar experiment. The oxidizer for the left side was O_2:N_2::1.0:3.76. The oxidizer for the right side was O_2:He::1:6.

Fig. 108 Water condensed inside the bomb after 10 bar experiment. The oxidizer was air (O_2:N_2:1.0:3.76). Hydrogen was burned at ϕ=0.5. Top view.

It was theorized that the mustard coloration was owed to the formation of nitrogen oxides (NOx). The physical and chemical characteristics of nitrogen dioxide (NO_2) in particular fit the bill observations quite well, including the color (Fig. 109). To test this hypothesis a simple test was devised; to substitute nitrogen in the oxidizer for an inert gas: helium. A 10-atm run of hydrogen at an equivalence ratio of 0.5 was prepared with mixture of oxygen and helium in the following volume ratio: O_2:He::1:6. The combustion products were odorless and colorless, see the right side of Fig. 107. The condensate was also transparent. It was concluded that the coloration air burning experiments was due to nitrogen oxidation. It can be said that, after the experiments, the bomb and the steam generated therein, were acting as an unintended wet scrubber. Nitrogen dioxide is highly soluble in water and decomposes in nitric acid promptly [34], which could explain why the gas phase loses the yellow color while if enough time is allowed, leaving a tarnished condensate behind.

Fig. 109 Nitrogen dioxide at different temperatures. By Eframgoldberg - Own work, CC BY-SA 3.0, https://commons.wikimedia.org/w/index.php?curid=28364789

HIGH-PRESSURE TURBULENT FLAME SPEED MEASUREMENTS

The fuel chosen to demonstrate the capabilities of the new rig is a mixture of hydrogen and carbon monoxide in equal volumetric proportion. The effect of pressure on the laminar flame speed of this particular mixture has been previously studied by this group [29]. Only one equivalence ratio will be studied in the present work, ϕ=0.5. This the approximate air fuel composition at which syngas is burned in gas turbines [35]. Three levels of pressure, 1, 5 and 10 bar were explored. The fans operated at 2000, 4000, and 8000 rpm to induce turbulence fluctuation of 1.4, 2.8, and 5.5 m/s respectively. It was not possible to run experiments past 4000 rpm at 5 and 10 bar. Both, the motors and the electrical installation proved to be outmatched by the torque demand of the lip seal at high pressure. All experiments were held at room temperature. Leaf blower impellers place near the wall stirred the gases.

Some relevant properties of the mixtures and their laminar flame speed values are reported below in Table 16. The integral length scale of the turbulence has been estimated as the length of the leading edge of the impeller, L_T = 20 mm. Turbulent flame regimes are typically shown in a Borghi diagram, Fig. 110. All conditions tested in this work belong to the thin reaction zone and also confined between a 1<Da<10. This region is of particular interest to the gas turbine community.

Table 16 Laminar flame properties of syngas and non-dimensional numbers for the turbulent flame speed matrix.

	$S_{L,u}{}^{\circ}$	$\delta_L{}^{*}$	$\mathrm{Re}_T{}^{\dagger}$		
	m/s	**μm**	**1.4 m/s**	**2.8 m/s**	**5.5 m/s**
1 bar	0.269	649	1621	3242	6369
5 bar	0.130	195	8116	16,231	
10 bar	0.081	142	16,185	32,370	

$*\delta_L = (T_b - T_u) / (dT/dx_{\max})$ $\quad$ $\dagger \mathrm{Re}_T = c' L_T / \nu$

A Photron high speed camera, Fastcam SA1.1 was used to acquire schlieren images at 25,000 frames per second like, e.g. Fig. 111 for the 5-bar case. The still images were post-processed with a Matlab script that finds the edge of the window and flame. The area enclosed by the flame edge is tallied and the radius of a circle with the same area is calculated. The radius of such circle would be 3.06 cm radius in the case of Fig. 111.

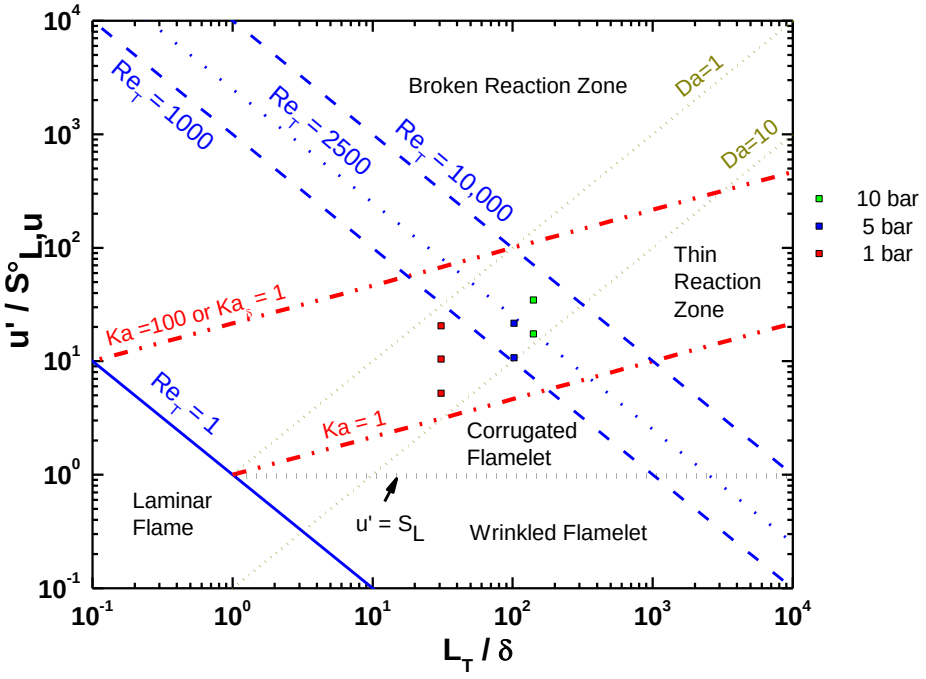

Fig. 110 Borghi diagram showing the conditions achieved in this work.

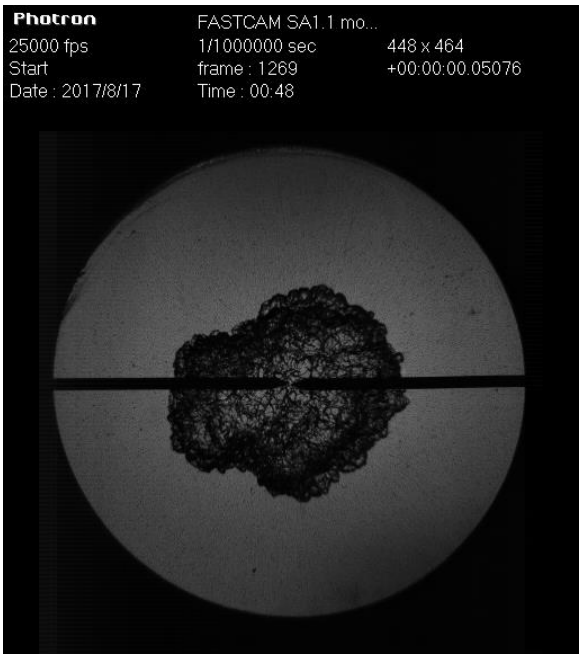

Fig. 111 Schlieren image of a syngas flame stirred at 2000 rpm. The initial pressure was 5 bar. Approximately 10.6 ms have elapsed since ignition.

Figure 112 show typical flame results for the 1-bar experiments, and Fig. 113 plots the flame radius as a function of time for the 3 different fan speeds. Note that 3 tests were performed for each condition, as seen in Fig. 113.

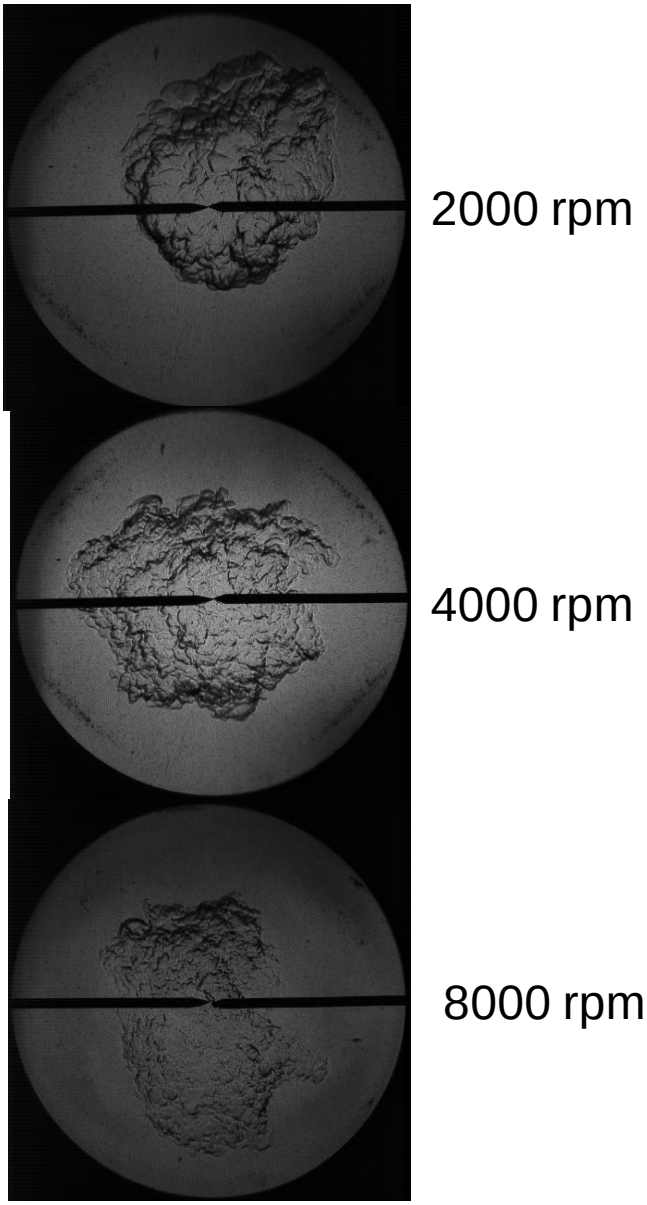

Fig. 112 Snapshot schlieren images for the 1-bar experiments for 3 different fan speeds.

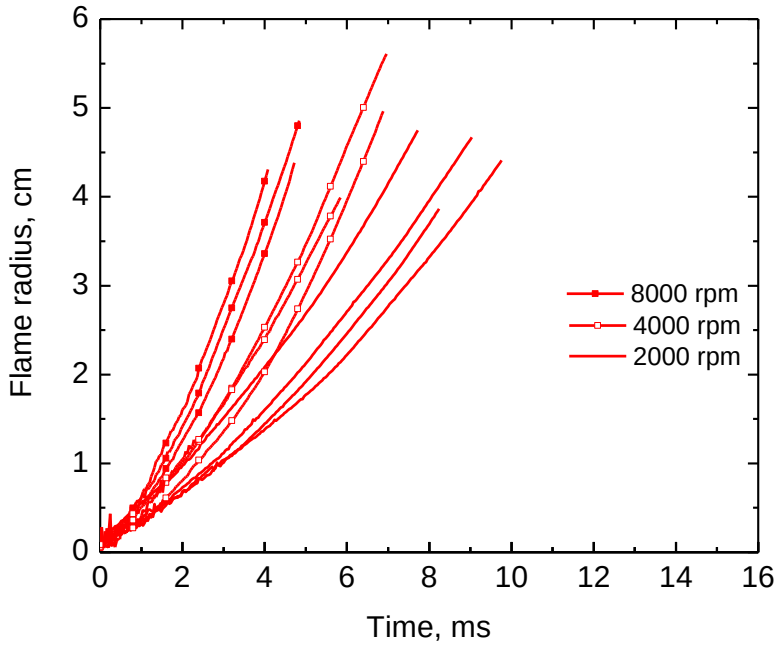

Fig. 113 Flame radius results for the 1-bar experiments.

Figure 114 show typical flame results for the 5-bar experiments, and Fig. 115 plots the flame radius as a function of time for two different fan speeds. Finally, Fig. 116 show typical flame results for the 10-bar experiments, and Fig. 117 plots the flame radius as a function of time for 2 different fan speeds.

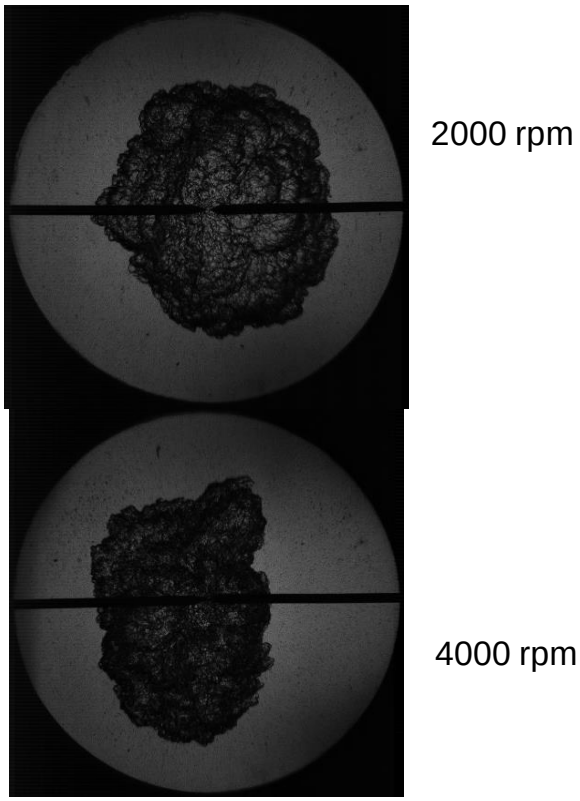

Fig. 114 Snapshot schlieren images for the 5-bar experiments for 2 different fan speeds.

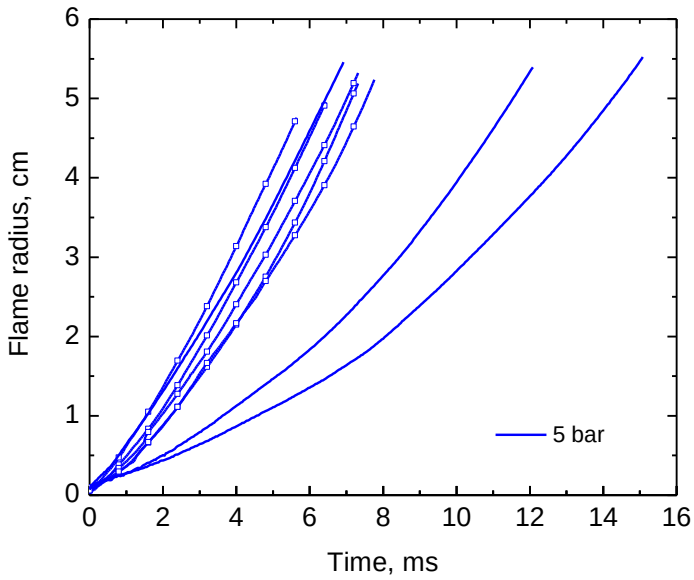

Fig. 115 Flame radius results for the 5-bar experiments at 2000 (lower) and 4000 (upper) rpm.

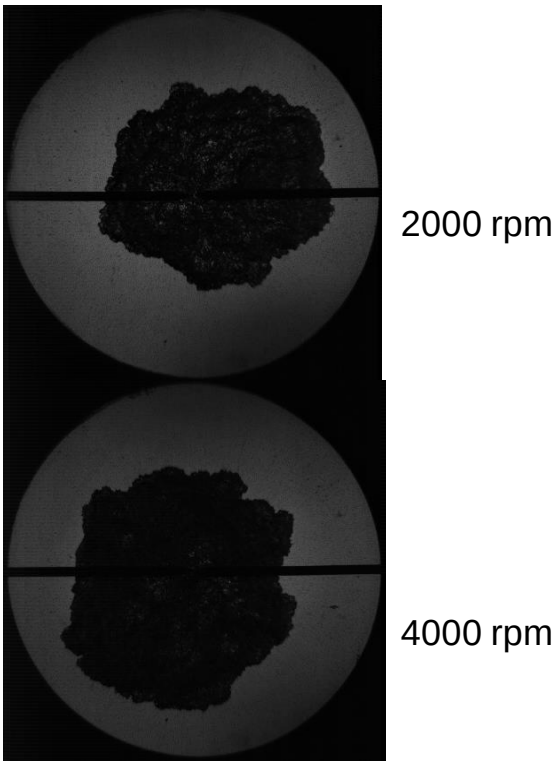

Fig. 116 Snapshot schlieren images for the 10-bar experiments for 2 fan speeds (2000, 4000 rpm).

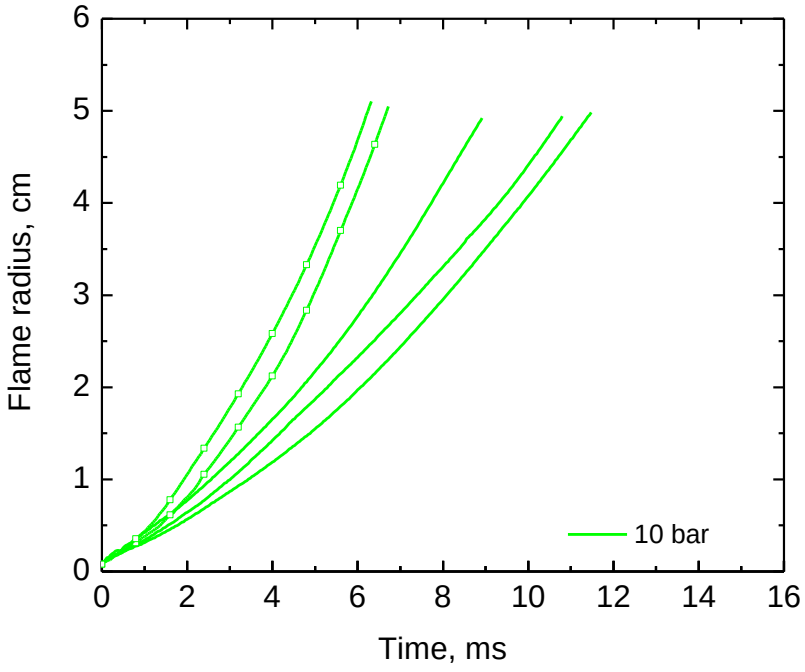

Fig. 117 Flame radius results for the 10-bar experiments.

A collage of the flame radius as a function of time has been assembled in Fig. 118. Each conditions was repeated three times. The stochastic nature of this phenomena is manifested the spread of results. It seems like the radius history is more sensible to the stirring level than it is to pressure. As a matter of fact results at 4000 rpm are lumped together in a region that contains the curves of all pressures tested here. The radius history evolves more rapidly as the turbulence level increases.

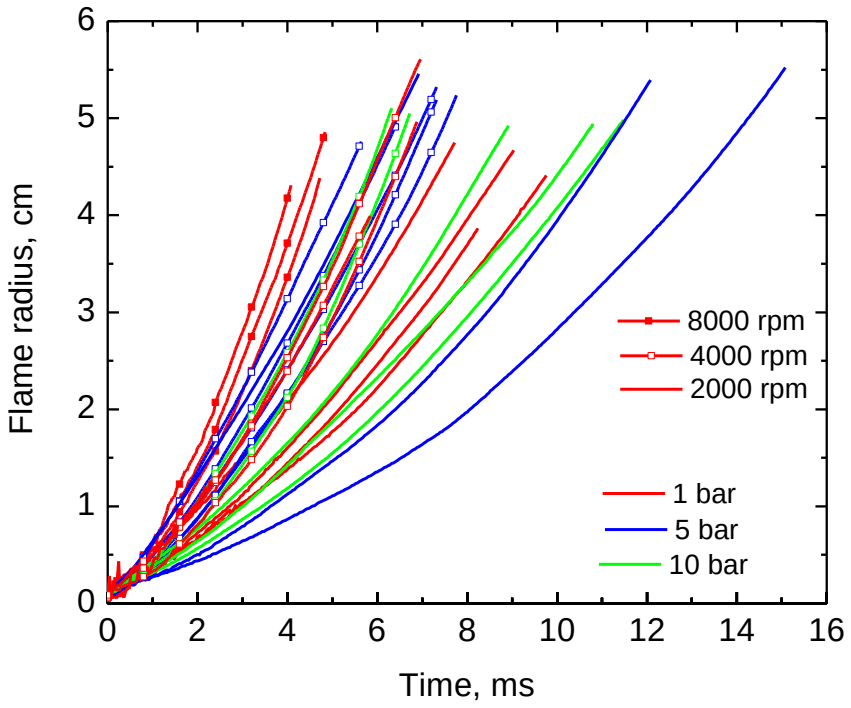

Fig. 118 Flame radius as a function of time for different conditions of pressure and fan speed.

If the derivative of radius versus time were taken, turbulent displacement velocity of the burned gases is obtained. The derivatives are very noisy, so the radii history was smoothed with a Savitsky-Golay method (2^{nd} order polynomial, 10 points per window). Furthermore, the repetitions averaged and the turbulent displacement velocity of the burned was plotted in Fig. 119. Again, the results are loosely grouped by level of turbulence, but there is now distinction between pressure treatments, that matches order of their respective laminar velocity.

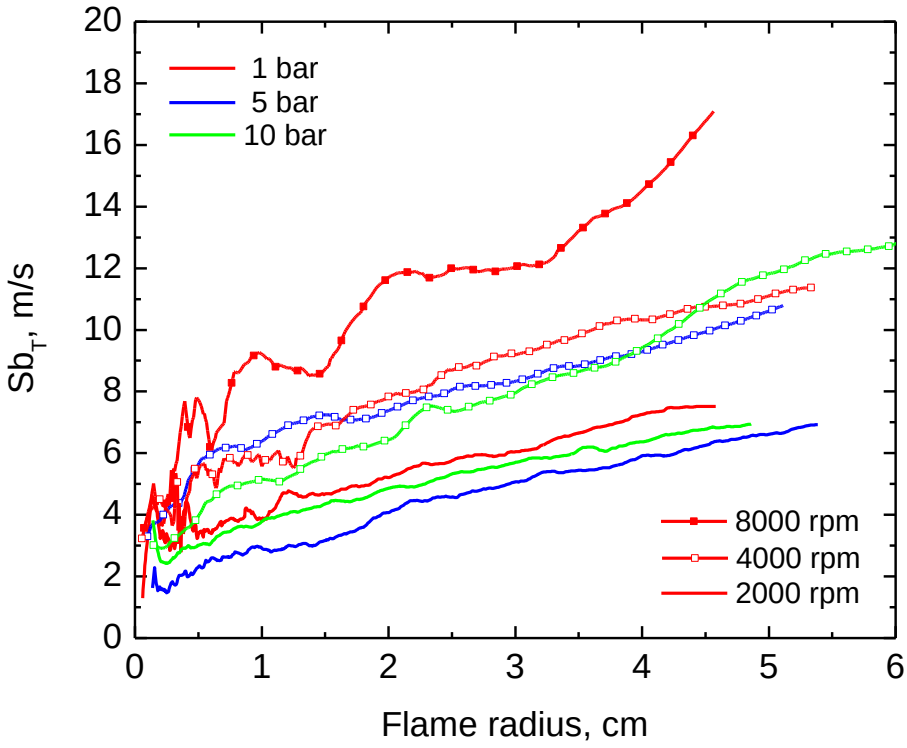

Fig. 119 Displacement velocity of burned gases. Each curve is the average of 3 repetitions.

CONCLUSION

The effects of impurities on fundamental combustion properties of premixed systems fueled with bio- or coal-derived syngases were investigated over a wide range of conditions relevant to gas turbine combustion. The results of this study show that not all the impurities have an effect on the ignition delay time or laminar flame speed. The concentration of the impurities, the temperature, and the pressure are also important factors governing the influence of impurities. While the effects of impurities are typically less important than for hydrocarbons, these effects appear to be linked to the chemistry only, as no noticeable flame temperature change was observed. NO_2 showed some promoting effects on the ignition delay time at conditions where the HO_2 radical was dominating. For the high-temperature flame speed process, HO_2 radicals do not play an important role, explaining the lack of effect of NO_2 on the laminar S_L. When H_2S, NH_3, and HCN are in the mixture, they will tend to react with H radicals and to produce radicals that present a lower reactivity than OH, hence reducing the reactivity of the mixture by limiting r1 ($H + O_2 \rightleftarrows OH + O$). However, H_2S will also have a promoting effect on the ignition delay time for conditions where the HO_2 radical is important (low-temperature, high-pressure conditions for the ignition delay time predictions). This lower-temperature behavior is due to a decrease in the r2 pathway ($H + O_2 + M \rightleftarrows HO_2 + M$) due to the reaction r6 ($H_2S + H \rightleftarrows SH + H_2$) followed by enhancing reactions (compared to r2) that will lead to r10 ($O + H_2 \rightleftarrows OH + H$).

COS and SO_2 are the only impurities that do not exhibit any effect on both the syngas laminar flame speed and the ignition delay time under the conditions investigated. One can conclude that these two species can be neglected for realistic syngas mixtures at gas turbine conditions.

Hydrocarbon addition significantly impacts the flame speed of syngas blends. This decelerating effect is especially noticeable for rich mixtures. The model does a very good job of predicting the flame speed for the syngas mixtures in the neat case. When hydrocarbons are added, the model still does a good job of predicting the general shape of the curve and accurately predicts the equivalence ratio of the peak flame speed. However, experiments found that when hydrocarbons were added, the model under predicts the flame speed by several percent. This under prediction is especially noticeable at the richer mixtures. While the current Aramco model under predicts the flame speed for syngas with hydrocarbon addition, it still does a very good job for the pure fuels involved.

Analysis of the flame images found that lean mixtures were typically less stable than the fuel rich ones. The addition of hydrocarbons was found to noticeably increase the flame stability. Hydrocarbon addition however was found to have little impact on the burned-gas Markstein lengths of the mixtures. The leanest mixtures tested were the only ones to show a negative Markstein length. On average, all mixtures had a consistent Markstein length with the bio-syngas mixtures having a noticeably wider deviation. The Lewis numbers of the mixtures were found to also be consistent. For the leaner cases, there was almost no change as hydrocarbons were added, although there was a slight change toward unity Lewis Number. For the rich mixtures, the Lewis number moved noticeably closer to 1.0 as hydrocarbons were added. In general, hydrocarbon addition seems to increase the stability of the flame. This result of hydrocarbon addition to the syngas mixture is especially important in the fuel lean regions which will typically be used in gas turbine and other industrial applications.

Detailed measurements of the turbulence field in the first generation turbulent flame speed rig were performed. The results obtained agree qualitatively with the previous work of Ravi et al. (2013). This result is encouraging considering the differences in the technique employed, the vessel geometry, and the extent of the measurements. The test region exhibits features that were fairly consistent in all the XY planes analyzed. Many of the features had a radial profile with an axis of symmetry along the cylindrical axis of the vessel. The turbulence fluctuation rms from the present LDV results was found to be slightly higher than the PIV results and overall homogenous and isotropic throughout the test region. The isotropy of the turbulence fluctuation was ratified by the $\overline{u_x u_y}$ Reynolds stress and the scatter plots of $\tilde{u}_x$ Vs. $\tilde{u}_y$. The local average velocity magnitudes were higher than expected, and the vortex pattern found during the impeller evaluation was confirmed to be present along the cylindrical axis. It was estimated that the vortex swirls at 350 rpm with the fans running at 8,000 rpm. While the two measured components of velocity had essentially zero mean flow at the test region level, a calculation for the axial component found a resultant mean flow of 0.4 m/s. The turbulence intensity ratio is within the target range only in the vicinity of the cylindrical axis. The integral time scale was at most one third of the macro time scale reported by Ravi et al. (2013). The turbulence fluctuation rms scales as expected with the fan speed. However, other parameters such as average velocity and the axial velocity deteriorated. In summary, while the flow presents some of the characteristics desired for spherical turbulent flame speed experiments, it has opportunities that can be addressed in the next iteration of flame bomb, perhaps shaping the bomb and fan arrangement closer to a regular polyhedron as other groups have tried [Galmiche et al., 2014; Ali, 1995; Davani and Ronney, 2015; Mével et al., 2009].

Chemical kinetics experiments were performed for hydrogen sulfide oxidation in both the laminar flame speed vessel and in the shock tube. The flame speed experiments involved mixtures of syngas (coal-derived) with 1% H_2S, but with argon as the diluent instead of nitrogen. The kinetics model agreed well with the data, although some improvement can be made in the fuel-rich region. In addition, some interesting kinetics were seen when comparing the argon-based results with baseline results with nitrogen. The shock-tube experiments have provided new data on the ignition delay times of H_2S-O_2 mixtures highly diluted in Ar (98%) as well as water time histories. An updated kinetics mechanism is currently underway, but the agreement with the data is rather good at this time. However, it is becoming clear that it will be difficult to reconcile the differences seen with some other data from the literature, and more work needs to be done in this regard for H_2S oxidation.

A new fan-stirred bomb has been built to study spherically expanding flames. This effort encompassed a great portion of the last 2.5 years of the project. The bomb is intended to access higher temperature and pressure (10 atm+) pre-ignition conditions compared to its predecessor (1 atm). It has been designed to support advanced optical techniques (LDV, PIV, PLIF, high-speed schlieren, etc.) and vented deflagrations. Different impeller geometries will be employed to modify the characteristics of the turbulent flow. The new vessel was characterized using a high-speed LDV setup, and an optimum impeller design for the fans was selected. Experiments were performed at pressures of 1, 5, and 10 bar for syngas mixtures in air, modeled as a 50:50 mixture by volume of H_2:CO. These tests demonstrate the achievement of the target regime on the Borghi diagram, and the details of the results in terms of schlieren images and flame radius versus time show the capabilities of this new device. Further analysis of the results and a broader range of conditions are required for future experiments of interest to the gas turbine community.

REFERENCES

Abdel-Gayed, R. G. (1978) "Mechanisms of turbulent flame propagation," Ph.D. Thesis, University of Leeds.

Abdel-Gayed, R. G., Al-Khishali, K. J., and Bradley, D. (1984) "Turbulent burning velocities and flame straining in explosions," *Proceedings of the Royal Society of London. Series A, Mathematical and physical sciences*, 391(1801), pp. 393-414.

Ali, Y.B. (1995) "Fundamentals of Turbulent Combustion Related to Gasoline Engines," in *Mechanical Engineering*. University of Leeds.

Andrews, G. E., Bradley, D., and Lwakabamba, S. B. (1975) "Measurement of turbulent burning velocity for large turbulent Reynolds numbers," *Proceedings of the Combustion Institute*, 15(1), pp. 655-664.

ASTM International (2016) "Standard Specification for Forged or Rolled Alloy and Stainless Steel Pipe Flanges, Forged Fittings, and Valves and Parts for High-Temperature Service," ASTM International.

ASME (2015) "ASME boiler and pressure vessel code," Rules for Construction of Pressure Vessels, ASME.

Bell, W. (1986) "Spectral analysis of laser velocimeter data with the slotted correlation method," Proceedings of the AIAA/ASME Fourth Fluid Mechanics, Plasma Dynamics and Lasers Conference.

Bouvet, N., Halter, F., Chauveau, C., Yoon, Y. (2013) "On the effective Lewis number formulations for lean hydrogen/hydrocarbon/air mixtures," *International Journal of Hydrogen Energy* **38** pp. 5949-5960.

Bradley, D., P. H. Gaskell, and X. J. Gu (1994) "Application of a reynolds stress, stretched flamelet, mathematical model to computations of turbulent burning velocities and comparison with experiments," *Combustion and Flame*, Vol. 96(3): pp. 221-248.

Burke, M. P., Qin, X., Ju, Y., and Dryer, F. L. (2007) "Measurements of Hydrogen Syngas Flame Speeds at Elevated Pressures," 5th U.S. Combustion Meeting.

Cayana, F.M., Zhi, M., Pakalapati, S.R., Celik, I., Wu, N., and Gemmen, R. (2008) "Effects of coal syngas impurities on anodes of solid oxide fuel cells," *J. Power Sources* 185, 595-602.

Chaineaux, J. and E. Dannin (1992) “Sizing of explosion vents for the protection of vessels in which gases are processed at pressure and temperature higher than ambient,” *Proceedings of loss prevention and safety promotion in the process industries*, Taormina, pp. 1-30.

Chen, Z. (2010) “On the extraction of laminar flame speed and Markstein length from outwardly propagating spherical flames,” *Combustion and Flame* **158** (2) pp. 291-300.

Clean Air Technology Center (MD-12) (1999) "Nitrogen oxides (NOx): why and how they are controlled," No. EPA-456/F-99-006R, U.S. Environmental Protection Agency, Research Triangle Park, N.C.

Cuoci, A., Frassoldati, A., Buzzi Ferraris, G., Faravelli, T., and Ranzi, E. (2007) “The ignition, combustion and flame structure of carbon monoxide/hydrogen mixtures. Note 2: Fluid dynamics and kinetic aspects of syngas combustion,” *Int. J. Hydrogen Energy* 32, 3486-3500.

Dagaut, P., Glarborg, P., and Alzueta M. U. (2008) “The oxidation of hydrogen cyanide and related chemistry,” *Prog. Energy Combust. Sci*. 3, 1-46.

Das, A. K., Kumar, K., and Sung, C.-J. (2011) “Laminar Flame Speeds of Moist Syngas Mixtures,” *Combustion and Flame*, 158, pp. 345-353.

Davani, A. A. and P. D. Ronney (2015) “A Jet-Stirred Apparatus for Turbulent Combustion Experiments,” *9th U. S. National Combustion Meeting*, Cincinnati, Ohio.

De Vries, J. (2009) "A study on spherical expanding flame speeds of methane, ethane, and methane/ethane mixtures at elevated pressures.," Ph.D., Texas A&M University, College Station, Texas.

Fansler, T. D., and Groff, E. G., 1990, "Turbulence characteristics of a fan-stirred combustion vessel," *Combustion and Flame*, 80(3-4), pp. 350-354.

Galmiche, B., et al. (2014) “Turbulence characterization of a high-pressure high-temperature fan-stirred combustion vessel using LDV, PIV and TR-PIV measurements,” *Experiments in Fluids*, Vol. 55(1): pp. 1-20.

Glarborg, P. (2007) “Hidden interactions - Trace species governing combustion and emissions,” *Proc. Combust. Inst*. 31, 77–98.

Glarborg, P. and Marshall, P. (2013) “Oxidation of Reduced Sulfur Species: Carbonyl Sulfide,” *International Journal of Chemical Kinetics* 45, 429–439.

Groff, E. G. (1987) "An experimental evaluation of an entrainment flame-propagation model," *Combustion and Flame*, 67(2), pp. 153-162.

Groff, E. G. (1982) "The cellular nature of confined spherical propane-air flames," *Combustion and Flame*, 48(0), pp. 51-62.

Harris, D. C., (1999) *Materials for infrared windows and domes: properties and performance*, SPIE Optical Engineering Press, Bellingham, Wash.

Haq, M. Z. (1998) "Fundamental Studies of Premixed Combustion," Ph.D., The University of Leeds, Leeds, UK.

Herzler, J., Herbst, J., Kick, T., Naumann, C., Braun-Unkhoff, M., and Riedel, U. (2012) "Alternative Fuels Based on Biomass: an Investigation of Combustion Properties of Product Gases," Proceedings of ASME Turbo Expo 2012, GT2012, paper GT2012-69282.

Hu, E., Huang, Z., He, J., and Miao, H. (2009) "Experimental and numerical study on laminar burning velocities and flame instabilities of hydrogen-air mixtures at elevated pressures and temperatures," *International Journal of Hydrogen Energy* **34** pp. 8741-8755.

Kéromnès, A., Metcalfe, W. K., Donohoe, N., Das, A. K., Sung, C. J., Herzler, J., Naumann, C., Griebel, P., Mathieu, O., Krejci, M. C., Petersen, E., Pitz, W. J., and Curran, H. J. (2013) "An Experimental and Detailed Chemical Kinetic Modelling Study of Hydrogen and Syngas Mixtures at Elevated Pressures," *Combustion and Flame* 160, 995-1011.

Krejci, M. C. (2012) "Development of a New Flame Speed Vessel to Measure the Effect of Steam Dilution on Laminar Flame Speeds of Syngas Fuel Blends at Elevated Pressures and Temperatures," M.S. Thesis, Texas A&M University, College Station, TX.

Krejci, M.C., Mathieu, O., Vissotski, A.J., Ravi, S., Sikes, T.G., Petersen, E.L., Kéromnès, A., Metcalfe, W., and Curran, H.J. (2013) "Laminar Flame Speed and Ignition Delay Time Data for the Kinetic Modeling of Hydrogen and Syngas Fuel Blends," *J. Engineering for Gas Turbines and Power*, 135 / 021503-1.

Kundu, P. K., I. M. Cohen, and D. R. Dowling (2012) *Chapter 12 - Turbulence*, in *Fluid Mechanics (Fifth Edition)*, Academic Press: Boston. pp. 541-620.

Lautkaski, R. and T. Vanttola (2011) *Duct Venting of Gas Explosions,* VTT Technical Research Centre of Finland.

Lee, H.C., Jiang, L.Y., and Mohamad, A.A. (2014) “A review on the laminar flame speed and ignition delay time of Syngas mixtures,” *International Journal of Hydrogen Energy* **39** pp. 1105-1121.

Lefebvre, A. H. and Ballal, D. R. (2010) *Gas turbine combustion: alternative fuels and emissions*, 3rd ed, Boca Raton,Taylor & Francis.

Libby, P. A. (1996) *Introduction to turbulence. Combustion: an international series.* Washington, D.C., Taylor & Francis.

Liu, C. C., Shy, S. S., Chen, H. C., and Peng, M. W. (2011a) "On interaction of centrally-ignited outwardly-propagating premixed flames fully-developed isotropic turbulence at elevated pressure," *Proceedings of the Combustion Institute*, 33(1), pp. 1293-1299.

Liu, C. C., Shy, S. S., Chiu, C. W., Peng, M. W., and Chung, H. J. (2011b) "Hydrogen/carbon monoxide syngas burning rates measurements in high-pressure quiescent and turbulent environment," *International Journal of Hydrogen Energy*, 36(14), pp. 8595-8603.

Lowry, W., de Vries, J., Krejci, M., Petersen, E., Serinyel, Z., Metcalfe, W., Curran, H., Bourque, G. (2011) “Laminar Flame Speed Measurements and Modeling of Pure Alkanes and Alkane Blends at Elevated Pressures,” *Journal of Engineering for Gas Turbines and Power* **133** pp. 091501-1 – 091501-9.

Mathieu, O., Levacque, A., and Petersen, E. L. (2012) “Effects of N_2O addition on the ignition of H2–O2 mixtures: Experimental and detailed kinetic modeling study,” *International Journal of Hydrogen Energy* 37, 15393-15405.

Mathieu, O., Kopp, M. M., and Petersen, E. L. (2013a) “Shock Tube Study of the Ignition of Multi-Component Syngas Mixture With and Without Ammonia Impurities,” Proc. Combust. Inst. 34, pp. 3211-3218.

Mathieu, O., Petersen, E. L., Heufer, A., Donohoe, N., Metcalfe, W. K., Curran, H. J., Güthe, F., Bourque, G. (2013b) “Numerical Study on the Effect 1 of Real Syngas Compositions on Ignition Delay Times and Laminar Flame Speeds at Gas Turbine Conditions,” *J. Eng. Gas Turbines Power*, DOI: 10.1115/1.4025248.

Mathieu, O., Levacque, A., and Petersen, E. L. (2013c) “Effects of NO_2 addition on hydrogen ignition behind reflected shock waves,” *Proceedings of the Combustion Institute* 34, 633-640.

Mathieu, O., Deguillaume, F., and Petersen, E. L. (2013d) Effects of H_2S addition on hydrogen ignition behind reflected shock waves: Experiments and modeling. Combustion and Flame, http://dx.doi.org/10.1016/j.combustflame.2013.07.011.

Mathieu, O., Hargis, J.W., Petersen, E.L., Bugler, J., Curran, H.J., and Güthe, F. (2014a), "The Effect of Impurities on Ignition Delay Times and Laminar Flame Speeds of Syngas Mixtures at Gas Turbine Conditions" ASME Paper GT2014-25412, Proceedings of ASME Turbo Expo 2014, June 16-20 2014, Düsseldorf, Germany.

Mathieu, O., Petersen, E.L., Heufer, A., Donohoe, N., Metcalfe, W., Curran, H.J., Güthe, F., and Bourque, G. (2014b) "Numerical Study on the Effect of Real Syngas Compositions on Ignition Delay Times and Laminar Flame Speeds at Gas Turbine Conditions," *Journal of Engineering for Gas Turbines and Power* **136** pp. 011502-1-011502-9.

Metcalfe, W. K., Burke, S. M, Ahmed, S. S, and Curran, H. J. (2013) "A Hierarchical and Comparative Kinetic Modeling Study of C1–C2 Hydrocarbon and Oxygenated Fuels," *Int. J. of Chem. Kinetics* 45, pp. 638-675.

Mével, R., et al. (2009) "Spherical expanding flames in H_2–N_2O–Ar mixtures: flame speed measurements and kinetic modeling," *International Journal of Hydrogen Energy*, Vol. 34(21): pp. 9007-9018.

Molkov, V.V. (2001) "Unified correlations for vent sizing of enclosures at atmospheric and elevated pressures," *Journal of Loss Prevention in the Process Industries*, 14(6): pp. 567–574.

Morones, A. (2015) "Turbulence Measurements in a Fan-Stirred Flame Bomb Using Laser Doppler Velocimetry," M.S. Thesis, Mechanical Engineering, Texas A&M University.

Morones, A., Leon, V. J., and Petersen, E. L. (2017) "Reconfigurable Fan-Stirred Flame Bomb with Optical Access," 55th AIAA Aerospace Sciences Meeting, American Institute of Aeronautics and Astronautics.

Munasinghe, P. C. and Khanal, S. K. (2010) "Biomass-Derived Syngas Fermentation into Biofuels: Opportunities and Challenges," Bioresour. Technol., 101, 5013–5022.

Natarajan, J., Nandula, S., Lieuwen, T., and Seitzman, J. (2005) "Laminar Flame Speeds of Synthetic Gas Fuel Mixtures," ASME Paper GT2005-68917.

Newby, A., Smeltzer, E. E., Lippert, T. E., Slimane, R. B., Akpolat, O. M., Pandya, K., Lau, F. S., Abbasian, J., Williams, B. E., and Leppin, D. (2001) "Novel Gas Cleaning/Conditioning for Integrated Gasification Combined Cycle Base Program," Report No. DE-AC26-99FT40674.

Oberg, E., Jones, F. D., Horton, H. L., and Ryffel, H. H. (2012) *Machinery's Handbook (29th Edition) & Guide to Machinery's Handbook*, Industrial Press.

Pegg, M., P. Amyotte, and S. Chippett (1992) "Confined and vented deflagrations of propane/air mixtures at initially elevated pressures," in *Proc. 7-th Intern. Symp. Loss Prevention in the Process Industries*, Taormina, Italy.

Peng, M. W. (2010) "Measurements of Laminar and Turbulent Burning Velocities for Centrally-Ignited, Outwardly Propagation Premixed Flames at Elevated Pressure," M.S., National Central University, Taiwan, Taiwan.

Prathap, C., Ray A., and Ravi, M. R. (2008) "Investigation of Nitrogen Dilution Effects on the Laminar Burning Velocities and Flame Stability of Syngas Fuel at Atmospheric Condition," *Combustion and Flame*, 155, pp. 145-160.

Ravi, S., Peltier, S. J., and Petersen, E. L. (2013) "Analysis of the Impact of Impeller Geometry on the Turbulent Statistics inside a Fan-Stirred, Cylindrical Flame Speed Vessel using PIV," *Experiments in Fluids*, Vol. 54, pp. 1424.

Razus, D.M. and U. Krause (2001) "Comparison of empirical and semi-empirical calculation methods for venting of gas explosions," *Fire Safety Journal*, **36**(1): pp. 1-23.

Russo, P. and A. Di Benedetto (2007) "Effects of a Duct on the Venting of Explosions - Critical Review," *Process Safety and Environmental Protection*, **85**(1): p. 9-22.

Santner, J., Haas, F. M., Ju, Y., Dryer, F. L. (2014) "Uncertainties in interpretation of high pressure spherical flame propagation rates due to thermal radiation" Combustion and Flame **161** pp. 147-153.

Sharma, S. D., McLennan, K., Dolan, M., Nguyen, T., and Chase, D. (2013) "Design and Performance Evaluation of Dry Cleaning Process for Syngas," Fuel, 108, 42–53.

Shy, S. S., I, W. K., and Lin, M. L. (2000) "A new cruciform burner and its turbulence measurements for premixed turbulent combustion study," *Experimental Thermal and Fluid Science*, 20(3-4), pp. 105-114.

Sick, V., Hartman, M. R., Arpaci, V. S., and Anderson, R. W. (2001) "Turbulent scales in a fan-stirred combustion bomb," *Combustion and Flame*, 127(3), pp. 2119-2123.

Sivaramakrishnan, R., Brezinsky, K., Dayma, G., and Dagaut, P. (2007) “High pressure effects on the mutual sensitization of the oxidation of NO and CH_4–C_2H_6 blends” *Phys. Chem. Chem. Phys.* 9 4230–4244.

Smallbone, A., Tsuneyoshi, K., and Kitagawa, T. (2006) "Turbulent and stable/unstable laminar burning velocity measurements from outwardly propagating spherical hydrogen-air flames at elevated pressures," *Journal of Thermal Science and Technology*, 1(1), pp. 31-41.

Trembly, J. P., Gemmen, R. S., and Bayless, D. J. (2007) “The effect of IGFC warm gas cleanup system conditions on the gas–solid partitioning and form of trace species in coal syngas and their interactions with SOFC anodes,” *Journal of Power Sources* 163, 986–996.

Varga, T., Olm, C., Nagy, T., Zsély, I. G., Valkó, É., Pálvölgyi, R., Curran, H. J., and Turányi, T. (2016) "Development of a Joint Hydrogen and Syngas Combustion Mechanism Based on an Optimization Approach," *International Journal of Chemical Kinetics*, 48(8), pp. 407-422.

Wang, J., Zhang, M., Huang Z., Kudo, T., and Kobayashi, H. (2013) “Measurement of the instantaneous flame front structure of syngas turbulent premixed flames at high pressure”. *Combustion and Flame* 160, 2434-2441.

Weiß, M. (2008) "Untersuchung von Flammenfrontstreckungseffekten auf die sphärische Flammenausbreitung laminarer und turbulenter Brennstoff/Luft-Gemische," Ph.D., Karslruhe University, Germany.

Weiß, M., Zarzalis, N., and Suntz, R. (2008) "Experimental study of Markstein number effects on laminar flamelet velocity in turbulent premixed flames," *Combustion and Flame*, 154(4), pp. 671–691.

Xu, Z.-R., Luo, J.-L., and Chuang, K. T. (2009) “The Study of Au/MoS2 Anode Catalyst for Solid Oxide Fuel Cell (SOFC) Using H2S-Containing Syngas Fuel,” *J. Power Sources*, 188, 458–462.

Xu, D., Tree, D.R., Randy S., and Lewis, R.S. (2011) “The effects of syngas impurities on syngas fermentation to liquid fuels,” *Biomass and Bioenergy* 35, 2690-2696.

APPENDIX

Flame speed facility drawings.

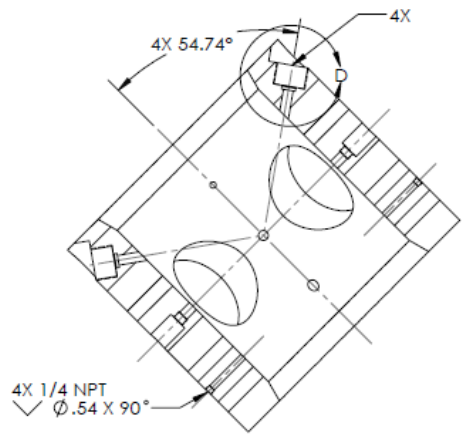

SECTION C-C

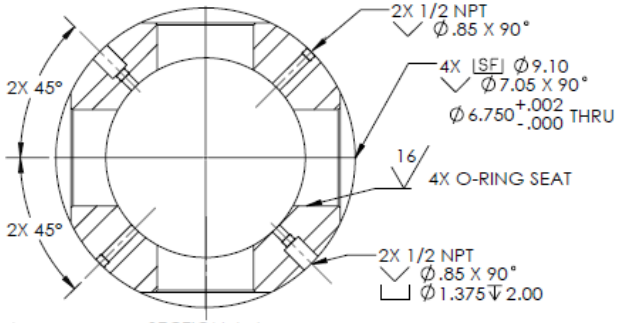

SECTION A-A

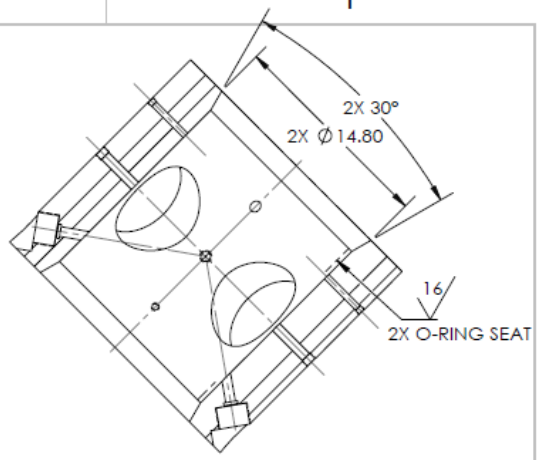

SECTION B-B

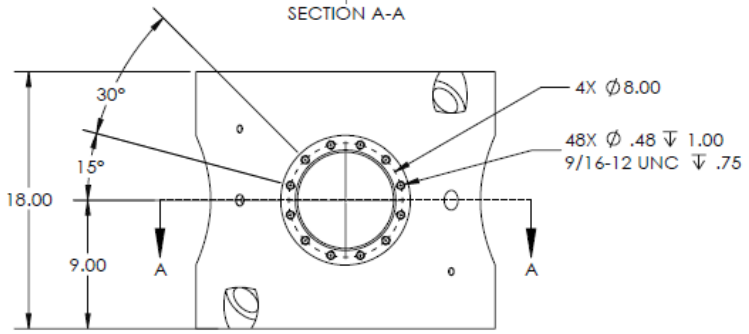

FRONT VIEW

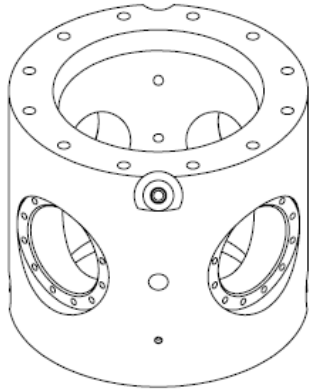

ISOMETRIC VIEW

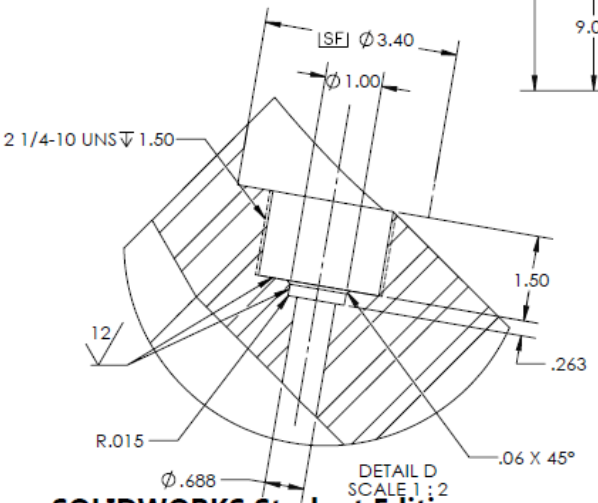

DETAIL D
SCALE 1 : 2

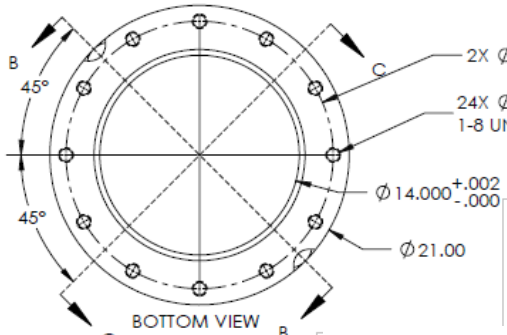

BOTTOM VIEW

THIRD ANGLE PROJECTION

SOLIDWORKS Student Edition.
For Academic Use Only.

UNLESS OTHERWISE SPECIFIED: DIMENSIONS ARE IN INCHES TOLERANCES: .X ±.1 .XX ±.01 .XXX ±.005 ANGULAR: ±1° BREAK ALL CORNERS R .05	COMMENTS	TEXAS A&M UNIVERSITY TITLE: Vessel
INTERPRET GEOMETRIC TOLERANCING PER: MATERIAL DO NOT SCALE DRAWING	CONTACT:	SIZE B | DWG. NO. TFSB-01 | REV SCALE: 1:8 | WEIGHT: | SHEET 1 OF 1

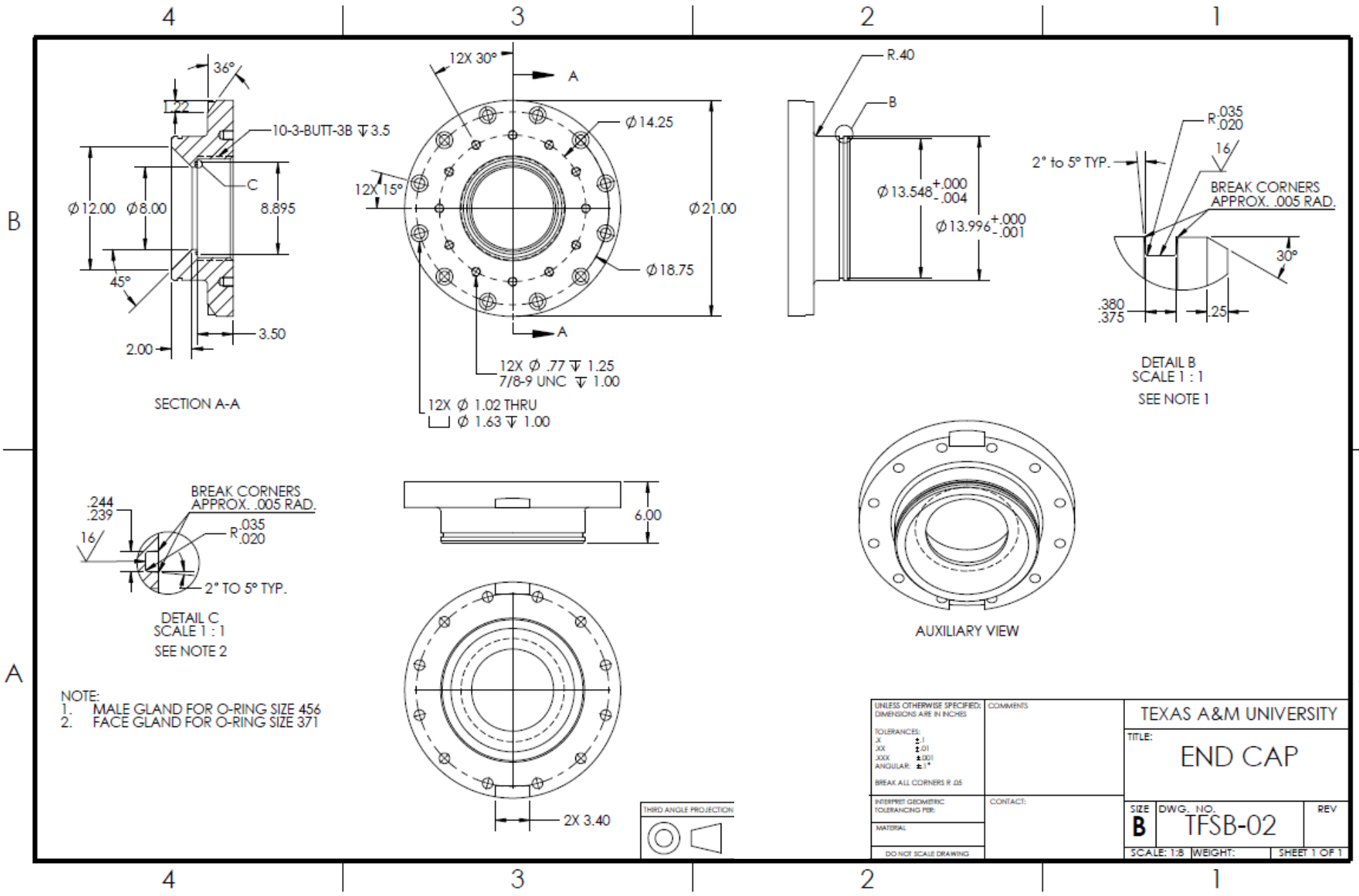
36°
.22
10-3-BUTT-3B ↧3.5
C
Ø12.00
Ø8.00
8.895
45°
2.00
3.50
SECTION A-A
12X 30°
A
Ø14.25
12X 15°
Ø21.00
Ø18.75
12X Ø .77 ↧ 1.25
7/8-9 UNC ↧ 1.00
12X Ø 1.02 THRU
Ø 1.63 ↧ 1.00
R.40
B
Ø13.548 +.000 -.004
Ø13.996 +.000 -.001
2° to 5° TYP.
R .035 .020
16
BREAK CORNERS
APPROX. .005 RAD.
30°
.380
.375
.25
DETAIL B
SCALE 1 : 1
SEE NOTE 1
.244
.239
16
BREAK CORNERS
APPROX. .005 RAD.
R .035 .020
2° TO 5° TYP.
DETAIL C
SCALE 1 : 1
SEE NOTE 2
6.00
AUXILIARY VIEW
2X 3.40
NOTE:
1. MALE GLAND FOR O-RING SIZE 456
2. FACE GLAND FOR O-RING SIZE 371
THIRD ANGLE PROJECTION
UNLESS OTHERWISE SPECIFIED:
DIMENSIONS ARE IN INCHES
TOLERANCES:
X ±.1
.XX ±.01
.XXX ±.001
ANGULAR: ±.1°
BREAK ALL CORNERS R .05
INTERPRET GEOMETRIC TOLERANCING PER:
MATERIAL
DO NOT SCALE DRAWING
COMMENTS
CONTACT:
TEXAS A&M UNIVERSITY
TITLE:
END CAP
SIZE B
DWG. NO. TFSB-02
REV
SCALE: 1:8
WEIGHT:
SHEET 1 OF 1

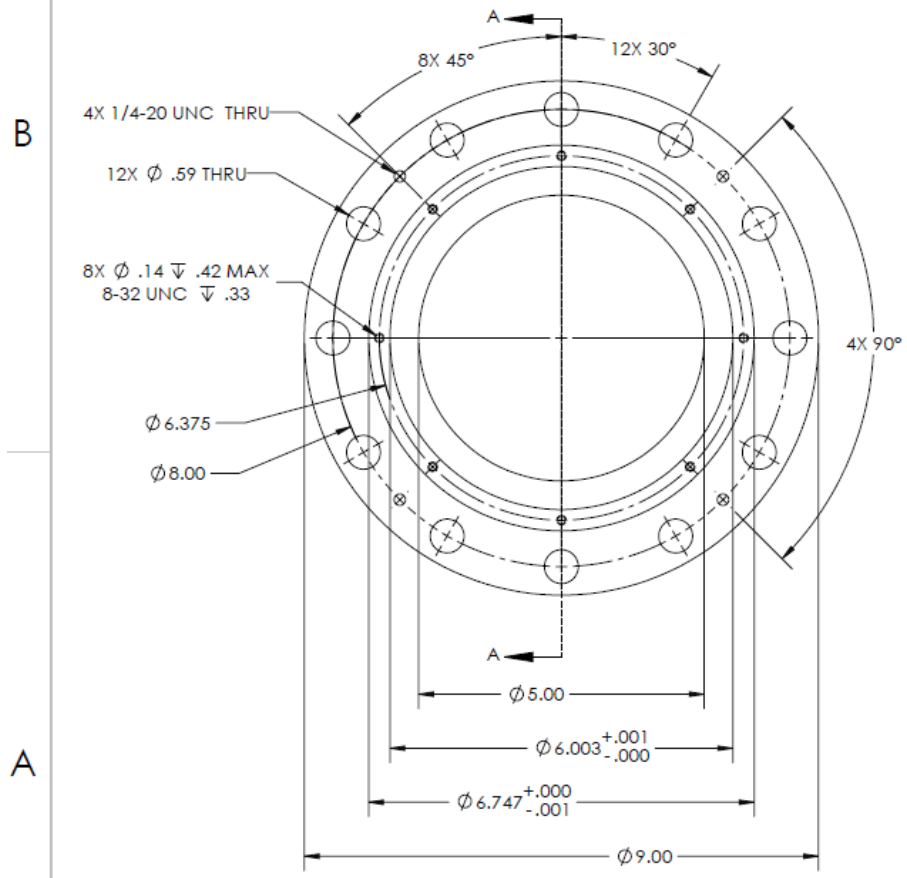

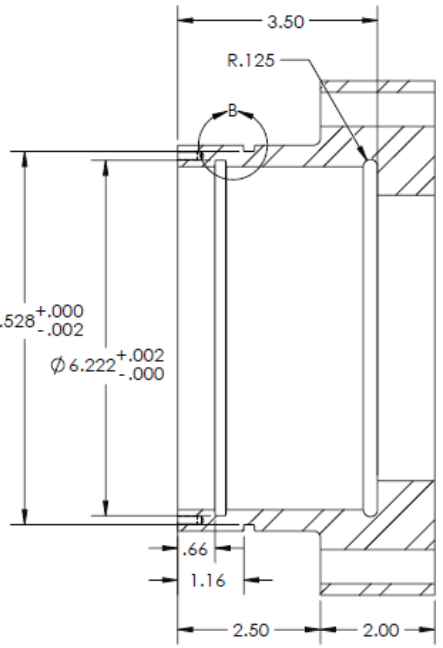

SECTION A-A
SCALE 1 : 2

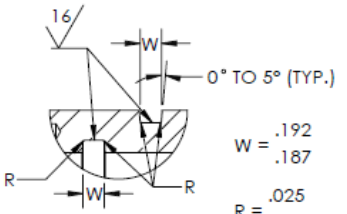

DETAIL B
SCALE 1 : 1

THIRD ANGLE PROJECTION

UNLESS OTHERWISE SPECIFIED: DIMENSIONS ARE IN INCHES

TOLERANCES:
.X ±.1
.XX ±.01
.XXX ±.005
ANGULAR: ±1°

BREAK ALL CORNERS R .05

INTERPRET GEOMETRIC TOLERANCING PER: ASME Y14.5

MATERIAL

DO NOT SCALE DRAWING

COMMENTS

CONTACT:

TEXAS A&M UNIVERSITY

TITLE:
WINDOW CASING

SIZE B | DWG. NO. TFSB-04 | REV

SCALE: 1:2 | WEIGHT: | SHEET 1 OF 1

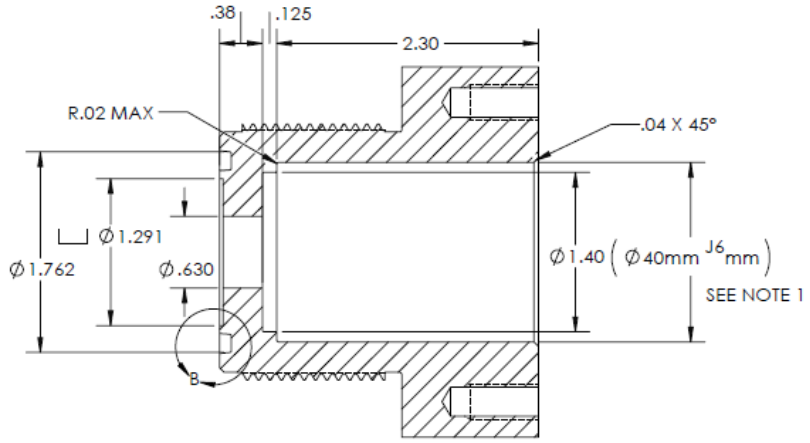

SECTION A-A

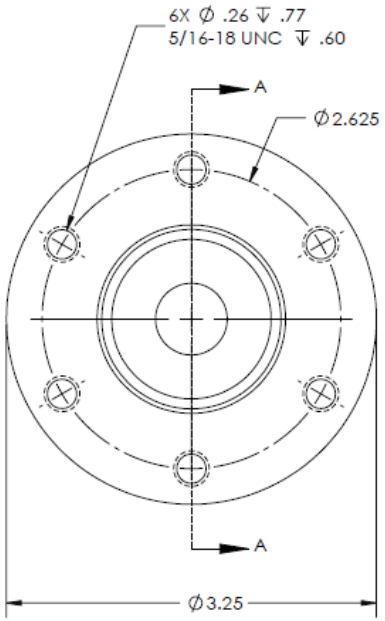

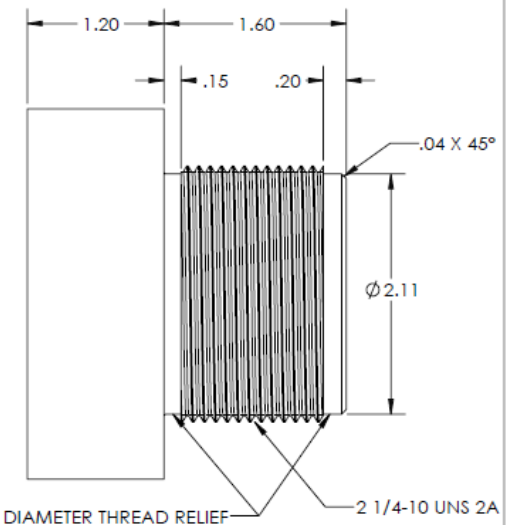

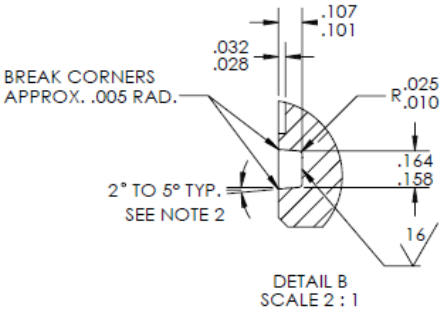

DETAIL B
SCALE 2 : 1

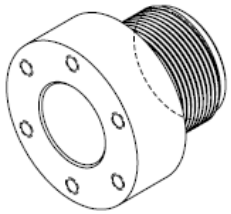

ISOMETRIC VIEW
SCALE 1 : 2

NOTES:
1. FOR METRIC BEARING OUTER RACE. BASIC DIAMETER 40MM. FIT J6
2. FOR O-RING SIZE 222

SOLIDWORKS Student Edition.
For Academic Use Only.

THIRD ANGLE PROJECTION

UNLESS OTHERWISE SPECIFIED: DIMENSIONS ARE IN INCHES TOLERANCES: .X ±.1 .XX ±.01 .XXX ±.001 ANGULAR: ±1° BREAK ALL CORNERS R .05	COMMENTS	TEXAS A&M UNIVERSITY TITLE: BEARING HOUSING
INTERPRET GEOMETRIC TOLERANCING PER: MATERIAL DO NOT SCALE DRAWING	CONTACT:	SIZE B | DWG. NO. TFSB-06 | REV SCALE: 1:1 | WEIGHT: | SHEET 1 OF 1

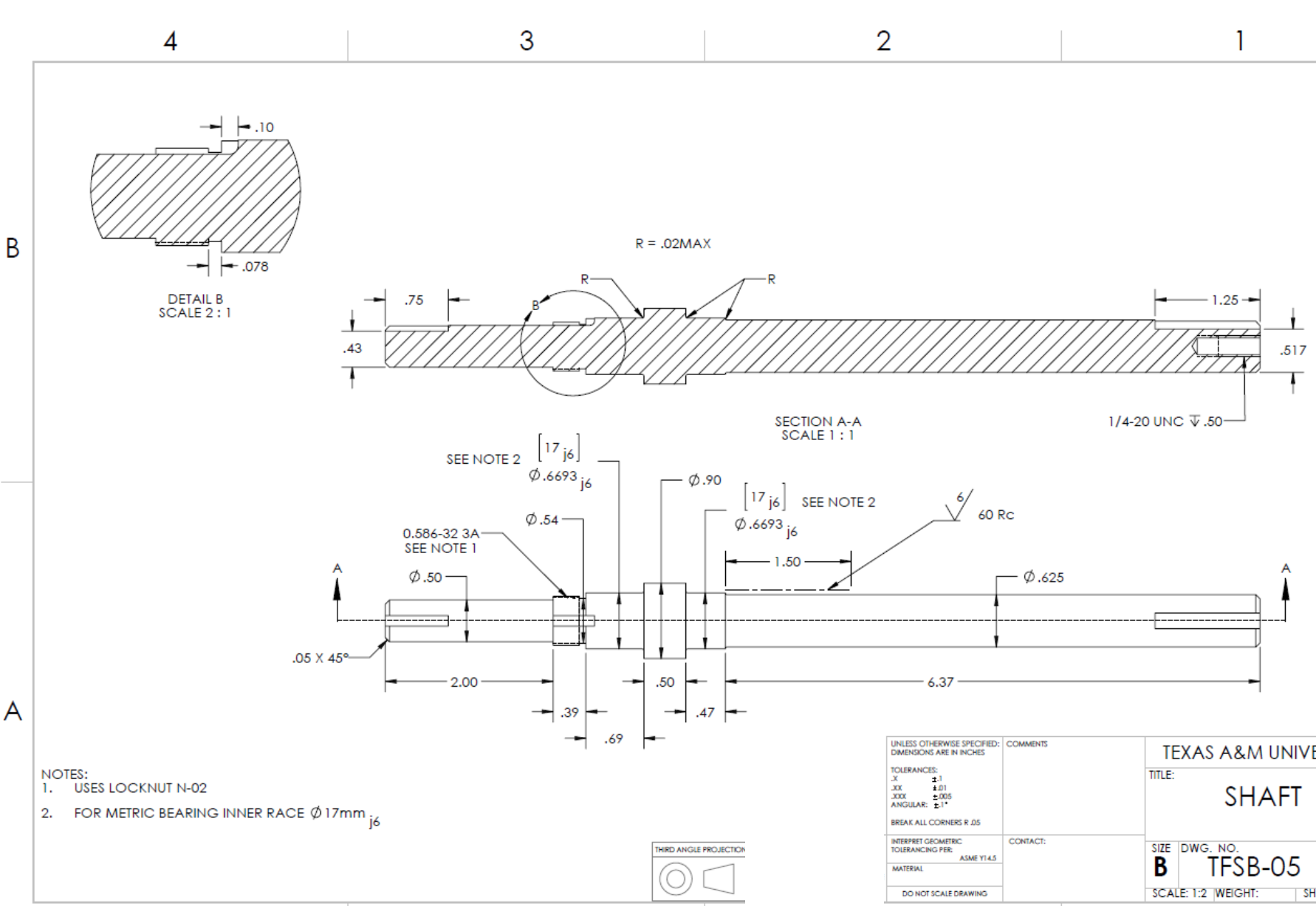
4
3
2
1
B
A
.10
.078
DETAIL B
SCALE 2 : 1
R = .02MAX
R
R
B
.75
1.25
.43
.517
SECTION A-A
SCALE 1 : 1
1/4-20 UNC ↧ .50
SEE NOTE 2
[17 j6]
Ø.6693 j6
Ø.90
[17 j6]
SEE NOTE 2
Ø.6693 j6
6
60 Rc
Ø.54
0.586-32 3A
SEE NOTE 1
A
Ø.50
1.50
Ø.625
A
.05 X 45°
2.00
.50
6.37
.39
.47
.69
NOTES:
1. USES LOCKNUT N-02
2. FOR METRIC BEARING INNER RACE Ø17mm j6
THIRD ANGLE PROJECTION
UNLESS OTHERWISE SPECIFIED:
DIMENSIONS ARE IN INCHES
TOLERANCES:
.X ±.1
.XX ±.01
.XXX ±.005
ANGULAR: ±1°
BREAK ALL CORNERS R .05
COMMENTS
INTERPRET GEOMETRIC TOLERANCING PER: ASME Y14.5
MATERIAL
DO NOT SCALE DRAWING
CONTACT:
TEXAS A&M UNIVERSITY
TITLE:
SHAFT
SIZE B
DWG. NO. TFSB-05
REV
SCALE: 1:2
WEIGHT:
SHEET 1 OF 1

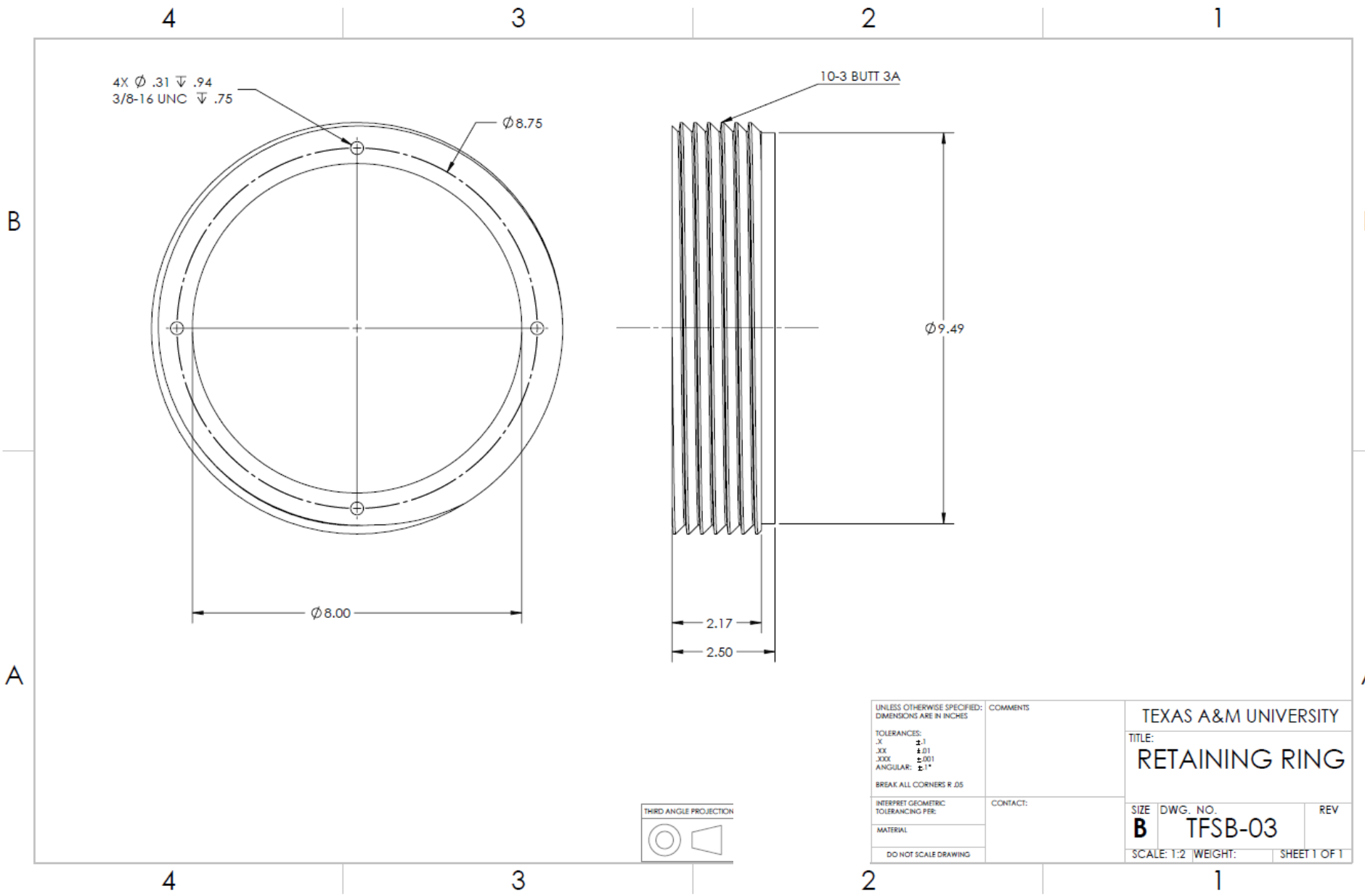
4X Ø .31 ↧ .94
3/8-16 UNC ↧ .75
Ø8.75
Ø8.00
10-3 BUTT 3A
Ø9.49
2.17
2.50
THIRD ANGLE PROJECTION
UNLESS OTHERWISE SPECIFIED:
DIMENSIONS ARE IN INCHES
TOLERANCES:
.X ±.1
.XX ±.01
.XXX ±.001
ANGULAR: ±1°
BREAK ALL CORNERS R .05
INTERPRET GEOMETRIC TOLERANCING PER:
MATERIAL
DO NOT SCALE DRAWING
COMMENTS
CONTACT:
TEXAS A&M UNIVERSITY
TITLE:
RETAINING RING
SIZE B
DWG. NO. TFSB-03
REV
SCALE: 1:2
WEIGHT:
SHEET 1 OF 1